NEUTRON CAPTURE CROSS SECTIONS FOR THE *i*-PROCESS

By

Caley Manuela Sorice Harris

A DISSERTATION

Submitted to
Michigan State University
in partial fulfillment of the requirements
for the degree of

Physics—Doctor of Philosophy

2025

ABSTRACT

Heavy element nucleosynthesis is one of the main focuses of the nuclear astrophysics community, specifically nucleosynthesis of elements heavier than Fe formed by neutron-capture processes. The slow (s) and rapid (r) processes are responsible for the synthesis of a majority of the heavier elements observed today. However, the reaction networks and astrophysical sites are not necessarily well-understood in all regions of the nuclear landscape. Discrepancies between stellar observations and models seem to imply that there is a missing piece to the neutron-capture puzzle. An intermediate (i) process was proposed in the 1970s to more accurately describe the abundance pattern of certain carbon stars [1]. The i process has gained traction in the recent decades as a viable model that can successfully reproduce observational data.

Astrophysical models for nucleosynthesis require nuclear physics inputs, such as nuclear masses, β-decay rates, and neutron-capture rates [2]. Masses and β-decay rates are known or isotopes near and far from the valley of stability, but neutron-capture rates are almost completely unknown for radioactive nuclei, even close to the stable isotopes. This is a major source of model uncertainty that has yet to be fully constrained due to the lack of experimental data. Two sensitivity studies by Denissenkov *et al.* [3] and Martinet *et al.* [4] identified reactions that most impact the final abundance of Sr calculated by i-process models. Both studies found the ^{88}Kr(n,γ)^{89}Kr reaction to have the strongest impact on the Sr abundance. An experimental measurement of this reaction could be used to constrain i-process models.

Neutron-capture experiments are particularly difficult due to the instability of both neutrons and the target isotopes of interest [5]. Away from the valley of stability, half-lives decrease and the decay products from β-decay are increasingly radioactive. This means that the decay products of the isotope of interest are a source of unwanted background. Another problem introduced far from stability is low beam intensity, which means that, in a β-decay experiment, a high efficiency detection method is necessary. To address these issues, the present work combines an established high efficiency γ-ray detector SuN, the Summing NaI(Tl) detector , with a new tape transport system [6, 7].

Tape systems can be used to transport radioactive isotopes from the implantation point to the detector. They can also be used to move radioactive decay products out of the detector volume to be stored in a shielded area. This reduces the background radiation from subsequent decays. The latter function is the intended function of the tape system constructed for SuN. However, the former option is still a possibility for future upgrades.

The SuN Tape system for Active Nuclei (SuNTAN) was developed between Michigan State University, Louisiana State University, and Argonne National Laboratory. To further reduce background, a β detector is needed to measure β particles in coincidence with γ rays detected in SuN. Due to SuN's small inner volume, the traditional tape system with β detector was not optimal to fit in the limited space. Therefore, the SuNTAN design was adapted to the geometrical constraints of SuN. To enhance the β-detection geometric acceptance, a new barrel-shaped, segmented plastic scintillator detector (SuNSPOT) was designed and fabricated at Hope College.

An experiment was performed at Argonne National Laboratory, in which a ^{89}Br beam was implanted in the tape at the center of SuN. The compound nucleus of interest is populated by the β^- decay of ^{89}Br into ^{89}Kr. SuNTAN was implemented to characterize the parent nucleus, as well as the decay of the daughter and granddaughter nuclei. After background contamination was removed, the NLD and γSF were extracted and normalized with the β-Oslo method [8, 9]. The extracted functions became inputs for the Hauser-Feshbach statistical code TALYS [10] to calculate the first experimentally-constrained reaction rate for ^{88}Kr(n,γ)^{89}Kr. Astrophysical i-process abundance simulations were performed taking into account the new reaction rate. The new rate was shown to strongly impact one-zone stellar models, but had only a moderate effect on multi-zone models.

TABLE OF CONTENTS

LIST OF ABBREVIATIONS

ANL Argonne National Laboratory

CARIBU CAlifornium Rare Isotope Breeder Upgrade

FRIB Facility for Rare Isotope Beams

JINA Joint Institute for Nuclear Astrophysics

MSU Michigan State University

NSCL National Superconducting Cyclotron Laboratory

DDAS Digital Data Acquisition System

DSSD Double-Sided Silicon Detector

PMT PhotoMultiplier Tube

SuN Summing NaI detector

SuNTAN SuN Tape-system for Active Nuclei

CHAPTER 1

INTRODUCTION

The human body consists of oxygen, carbon, nitrogen, hydrogen, calcium, along with trace amounts of magnesium, zinc, fluorine, and many more elements. Each element was created in a stellar environment, billions of years ago. The death of stars left behind dust that eventually made its way into each and every one of us. To quote astronomer Carl Sagan, "The cosmos is within us. We are made of star-stuff" [11]. Humanity is driven by curiosity, and throughout history, our heads have continued to turn to the night sky. For thousands of years, people gazed up at the cosmos, tracking the movements of "stars" that were eventually discovered to be planets, using the constellations to navigate the vast oceans, and pushing science further to achieve a deeper understanding of our universe. The inventions of the telescope, space satellites, and interferometers have greatly expanded the bounds of our world and continue to this day.

Advancements in nuclear physics have also developed our understanding of the cosmos. We have the ability to measure the same reactions in the laboratory that occur in stellar environments light-years away. The field of nuclear astrophysics takes advantage of our earth-bound laboratories to study nucleosynthesis. The current scientific landscape, intersections of diverse fields can be found performing cutting-edge research. Hopefully, this work will provide a small look into the world of nuclear astrophysics and provide insight into the work that is being done to answer some of the universe's biggest questions.

The rest of this thesis will take the reader through a crash course of nuclear physics in Chapter 2 and astrophysics in Chapter 3. These chapters will also motivate the remainder of this work. Chapter 4 illustrates the experimental setup, while Chapter 5 lays out the techniques implemented for experiment and analysis. An extensive description of the analysis performed can be found in Chapter 6. Finally, results are presented in Chapter 7, followed by a summary in Chapter 8.

CHAPTER 2

NUCLEAR PHYSICS

An atomic nucleus is formed by a collection of nuclear particles called nucleons. There are two species of nucleons, the positively-charged proton and the electrically neutral neutron. The nucleus is bound together by the strong force, which overpowers the Coulomb repulsion between protons at short ranges. Just as elements are defined by their number of protons Z, nuclides are characterized by the number of protons, number of neutrons N, and mass number $A = Z + N$ of the nucleus. Mendeleev classified elements into the periodic table, which is organized by proton number. Similarly, the nuclear version is called the chart of nuclides, shown in Fig. 2.1, where the y-direction represents increasing Z and the x-direction increasing N. In the periodic table, each Z corresponds to a different element, whereas in the chart of nuclides, nuclei of a one element can have a multiple mass numbers A, that is, a different number of neutrons for the same number of protons. Species of equal Z and different N are called *isotopes*, and can be written ${}^{A}_{Z}\mathrm{X}_{N}$, where X is the elemental symbol.

Isotopes can be stable, represented by the black squares in the chart of nuclides, or unstable meaning the nucleus will decay at some point into another species. The stable nuclei form the "valley of stability," named because unstable isotopes on either side will decay from the edges (driplines) toward the stable isotopes. For small Z, the mass A increases linearly with $N = Z$ until around $Z = 20$, at which point there are generally more and more neutrons per proton. As the number of protons increase, the Coulomb repulsion grows and more neutrons are needed to balance the electromagnetic repulsion via the strong force. The properties of nuclei include mass, decay modes and half-lives, reaction modes and cross sections, nuclear radius, spin, and more. Many types of experiments are needed to study and measure all of the properties of even a single nuclear species.

2.1 Nuclear Structure

Understanding the structure of the nucleus has come a long way, from the "plum pudding" model of the atom, where there was no nucleus, to the liquid drop model that incorporates the Pauli

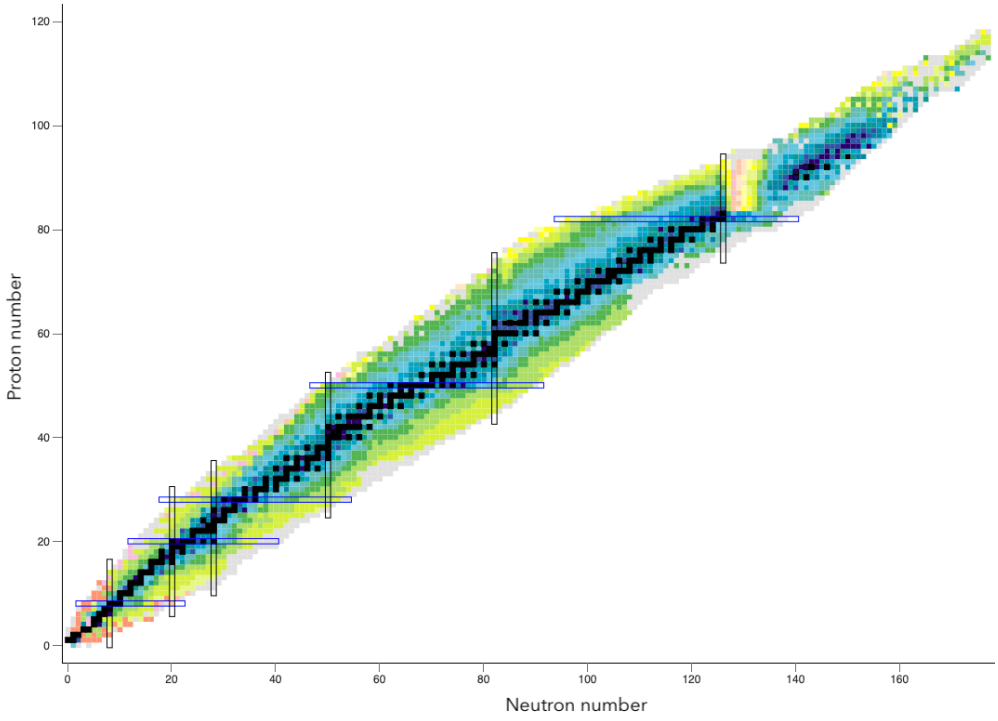

Figure 2.1 The chart of nuclides. The stable isotopes are shown as black squares and the colorful squares represent radioactive isotopes, the shade indicating different half-life time ranges. (Source: https://www.nndc.bnl.gov/)

exclusion principle. The shell model can be used to describe the structure of a nucleus in a similar manner in which electrons fill shells of discrete energy. In atomic physics, the electrons exist in a potential created by the positively-charged nucleus. In nuclear physics, the nucleons exist in and create their own potential. A shell model prescription treats single nucleons with a potential that is created by all of the other nucleons in the nucleus. As fermions, the Pauli exclusion principle, which states that two identical nucleons cannot share the same set of quantum numbers, must be obeyed. As protons and neutrons are not identical, they fill their own shells.

The most basic shell model potential is the Woods-Saxon potential, given by

$$V(r) = \frac{V_0}{1 + \exp\left(\frac{r-R}{a}\right)} \tag{2.1}$$

V_0 represents the depth of the potential well depth, a describes the "thickness" of potential boundary, and the nuclear radius is given by $R = r_0 A^{1/3}$ where $r_0 = 1.25$ fm. The Woods-Saxon potential can accurately predict levels and shell closures up to $Z, N = 20$, but the degenerate levels require

an additional term to account for further splitting by total angular momentum J. If this potential is applied, the states can be labeled by $J = \ell \pm 1/2$, and the shell model is able to accurately predict all shell closures up to $Z, N = 126$ and beyond.

2.2 Nuclear Decay

Radioactive nuclei can spontaneously decay in order to reach a more energetically stable configuration. Measurements of radioactive decay can provide useful information about the structure and shape of nuclei, as well as reaction properties, among other things. There several decay modes, include α decay, β decay, γ decay, spontaneous fission, and nucleon emission.

2.2.1 Nuclear Decay Modes

Through α decay, an unstable nucleus can de-excite by ejecting an α particle.

$$ {}^{A}_{Z}\mathrm{X}_{N} \rightarrow {}^{A-4}_{Z-2}\mathrm{X}_{N-2} + {}^{4}_{2}\mathrm{He}_{2} \tag{2.2} $$

A nucleus undergoing β decay emits a β particle in order to correct for an excess number of neutrons or protons. This decay materializes in three ways, with charge always conserved: β^- decay (Eq. 2.3), β^+ decay (Eq. 2.4), and electron capture (EC) (Eq. 2.5). In $\beta^{-(+)}$ decay, an electron (positron) and a neutrino (antineutrino) are created from the decay energy, and in EC, a proton in the nucleus captures an electron from a low-lying atomic orbit. The last two β decay modes can occur in bound protons, as well as bound and free neutrons because the neutron is unstable on its own.

$$ \beta^- : \ \mathrm{n} \rightarrow \mathrm{p} + \mathrm{e}^- + \bar{\nu}_e \tag{2.3} $$

$$ \beta^+ : \ \mathrm{p} \rightarrow \mathrm{n} + \mathrm{e}^+ + \nu_e \tag{2.4} $$

$$ \mathrm{EC} : \ \mathrm{p} + \mathrm{e}^- \rightarrow \mathrm{n} + \bar{\nu}_e \tag{2.5} $$

γ decay is similar to the relaxation of an electron in an excited atom, but instead the protons and neutrons relax from a high energy state to a lower energy level. This decay often occurs after an α or β decay. Spontaneous fission can occur in heavy, neutron-rich nuclei in which the nucleus splits into two lighter particles. The fission fragments are of roughly equal mass and neutron-rich due to the large number of neutrons in the nucleus that undergoes fission.

$$ \mathrm{X}^* \rightarrow \mathrm{X} + \gamma \tag{2.6} $$

Lastly, nucleon emission in the form of an emitted neutron or proton can occur if the particle energy is greater that the particle separation energy, which is given by

$$S_n = [m(^{A-1}_{Z}\mathrm{X}_{N-1}) - m(^{A}_{Z}\mathrm{X}_{N}) + m_n]c^2 \tag{2.7}$$

for neutrons and

$$S_p = [m(^{A-1}_{Z-1}\mathrm{X}_{N}) - m(^{A}_{Z}\mathrm{X}_{N}) + m(^{1}\mathrm{H})]c^2 \tag{2.8}$$

for protons.

2.2.2 Exponential Decay Law

Radioactive decay is statistical in nature. We can never know if or when a single nucleus will decay, but we can determine the decay rate for a large number of identical isotopes. A radioactive decay is defined by the decay constant λ, which is the probability that a nucleus will decay per unit time, and can be expressed as

$$\lambda = -\frac{dN/dt}{N}, \tag{2.9}$$

where N is the number of nuclei. In addition to the decay rate, decays can be characterized by half-life,

$$t_{1/2} = \frac{ln(2)}{\lambda}, \tag{2.10}$$

which is the amount of time for the initial population to halve in number, and mean lifetime

$$\tau = \frac{1}{\lambda}. \tag{2.11}$$

The exponential law of decay can be derived by integrating Eq. 2.9.

$$\int_0^t \lambda dt = \int_{N_0}^{N} \frac{dN}{N} \tag{2.12}$$

$$\lambda t = ln(N) - ln(N_0) \tag{2.13}$$

$$e^{-\lambda t} = \frac{N}{N_0} \tag{2.14}$$

Finally, the exponential decay law is given by

$$N(t) = N_0 e^{-\lambda t}, \tag{2.15}$$

where N_0 is the number of nuclei at time $t = 0$. This law only describes the decay of an initial number of radioactive nuclei allowed to decay. If nuclei are added at any point in time, there is a build-up of radiation, and thus an additional rate term is needed to describe the decay. For a constant rate of incoming particles, such as when a radioactive beam implants on a target, it takes 2-3 half-lives to reach 75-87.5% of maximum, or saturation, meaning the rate of added nuclei is the same as the decay rate [12].

Another way to describe a decay is by the activity, which is the number of decays per unit time, usually seconds. Activity is defined as $A(t) = \lambda N(t)$, which can also be written as

$$A(t) = A_0 e^{-\lambda t} \tag{2.16}$$

2.2.3 Decay Chains

In the previous section, the description for a decay of one species into a stable isotope was provided. For isotopes further from the valley of stability, it is likely that a series or chain of decays will occur with the original nucleus as the parent and subsequent generations called daughter, granddaughter, and so forth. Assuming at time $t = 0$ there is only the parent species present, then the number of the parent and daughter nuclei at time t can be written

$$N_p(t) = N_p(0) e^{-\lambda_p t} \tag{2.17}$$

$$N_d(t) = \frac{\lambda_d}{(\lambda_d - \lambda_p)} N_p(0) \left(e^{-\lambda_p t} - e^{-\lambda_d t} \right). \tag{2.18}$$

Similar to build-up of radioactive nuclei, another example of saturation is when rate of production of the daughter is equal to the decay rate of daughter. For the isotopes studied in this thesis, there were 4 or more generations of decays from the parent nuclei. In this case, the decay equations can get quite complicated. Fortunately, a general solution was found by Bateman, whose eponymous equations were named the Bateman equations [13]. Beginning with Eq 2.15,

$$N(t) = N_0 \exp^{-\lambda t}, \tag{2.19}$$

the general solution for a decay chain $X_1 \rightarrow X_2 \rightarrow \cdots \rightarrow X_i \cdots \rightarrow X_n$ of total length n is given by

$$N_n(t) = N_0(0) \times \left(\prod_{i=1}^{n-1} \lambda_i \right) \times \sum_{i=1}^{n} \frac{\exp^{-\lambda_i t}}{\prod_{j=1, j \neq i}^{n} (\lambda_j - \lambda_i)} \tag{2.20}$$

For the example of a parent decaying into a radioactive daughter, we can write the decay chain as

$$A \xrightarrow{\lambda_A} B \xrightarrow{\lambda_B} C \tag{2.21}$$

The parent population is given by

$$N_A(t) = N_A(0)e^{-\lambda_A t}, \tag{2.22}$$

The number of species of daughter nuclei B is expressed as

$$N_B(t) = \frac{\lambda_A}{(\lambda_B - \lambda_A)} N_A(0)\left(e^{-\lambda_A t} - e^{-\lambda_B t}\right), \tag{2.23}$$

while the number of nuclei of the granddaughter species C is

$$N_C(t) = \lambda_A \lambda_B N_A(0)\left[\frac{e^{-\lambda_A t}}{(\lambda_B - \lambda_A)(\lambda_C - \lambda_A)} + \frac{e^{-\lambda_B t}}{(\lambda_A - \lambda_B)(\lambda_C - \lambda_B)} + \frac{e^{-\lambda_C t}}{(\lambda_A - \lambda_C)(\lambda_B - \lambda_C)}\right] \tag{2.24}$$

The Bateman equations provide a general solution that can be used for any nucleus at any point in a decay chain.

2.3 Nuclear Reactions

Nuclear reactions describe the process of collision between nuclear entities. A basic reaction can be written $A + B \rightarrow C + D$ or $B(A, C)D$, in which A is the projectile, B is the target and together they compose the entrance channel. The exit channel is comprised of the residual nuclei C and D. Reactions are defined by their Q-value, which is the amount of energy required or released during a reaction:

$$Q = (m_A + m_B - m_C - m_D)c^2. \tag{2.25}$$

Negative Q-values describe reactions that release energy (endothermic), while positive Q-values equal the amount of energy a system requires to undergo the exothermic reaction. Reactions can be divided into two broad categories: direct and compound-nucleus reactions.

Direct reactions occur in short time frames (10^{-22} s) and involve incident particles with high energy. The cross section, which describes the probability for a reaction to occur for a given incident energy or angle, varies smoothly with a large peak at small angles in reference to the center-of-mass

frame. High energy projectiles do not spend a long enough time near the nucleus to interact with more than a few surface nucleons or with the collective nucleus. Direct reactions include transfer reactions, such as stripping $A(p,d)B$ or pick-up reactions $A(d,p)B$, as well as break-up reactions $A(B = C + D, C + D)A$. The first reactions after the Big Bang were direct reactions and will be discussed in the next chapter.

The second type of reaction is called a compound nucleus (CN) reaction. These reactions transpire over a relatively long timescale (10^{-19} to 10^{-15} s). Capture reactions, in which a nucleus absorbs an incident proton or neutron, are a form of CN reaction. For a projectile with a small impact parameter, which describes a distance measured from the target, the nucleon has a high probability of interacting with nucleons in the target. For low incident energies, a projectile that scatters from a nucleon will transfer some of its energy, but neither will have enough energy to escape the nucleus after the interaction. The scattered nuclei subsequently collide randomly with more nucleons, until the point that all of the incident energy has been dispersed throughout the nucleus. Random collisions result in an isotropic emission with the statistical Maxwell-Boltzmann energy distribution. CN reactions can be divided into three distinct stages: absorption of the projectile, formation of compound nucleus, and emission from the de-excitation of the CN. This reaction can be written as: $a + A \rightarrow C^* \rightarrow b + B$, where a is the projectile, A is the target nucleus, C^* is the compound nucleus in an excited state, and B and b are the final nuclei emitted. The CN can be populated at a discrete low-lying energy level, giving rise to a single peak or resonance in the cross section. Resonances are measured by their full width at half maximum (FWHM) Γ and the wider the resonance, the longer the nucleus exists in that state. The CN may also be populated at higher excitation energies where the density of levels is high. In this regime, the cross section becomes smooth because individual resonances are no longer resolved.

Niels Bohr formed the independence hypothesis about CN reactions that postulates that the decays of the final states are independent of the way in which the CN was formed. Effectively, the compound nucleus "forgets" all information prior to its existence and the decays behave statistically. This thesis will focus on the statistical decay of CN reactions, as described by the Hauser-Feshbach

formalism (See Section **??**).

2.3.1 Neutron-capture Reactions

Nucleon capture reactions are a form of CN reaction for low energy incident nucleons. Both (n, γ) and (p, γ) reactions play a role in stellar reactions that drive nucleosynthesis. Proton-capture reactions are challenging to measure at stellar energies, because the incident proton must overcome the Coulomb barrier for the reaction to occur, resulting in extremely low cross sections. While neutron capture is unaffected by the Coulomb potential, there remain challenges for experimentalists. In many cases, the CN is characterized by narrow resonance widths and a high level density, for which Hauser-Feshbach statistical methods can be utilized to extract information.

[fig 12.13 in Krane p. 462]

2.4 Hauser-Feshbach Model

In the 1950's, Hauser and Feshbach [14] developed a method to calculate the cross section of a reaction using statistical properties, rather than microscopic models that considered the interactions between all particles participating in the reaction, a computationally costly process. The Hauser-Feshbach (HF) model relies on two assumptions. (1) Upon absorption of an incident projectile, a compound nucleus is formed in a highly excited state, and its decay pathway is independent of the formation mechanism (Bohr's independence hypothesis). (2) Decay channel probabilities can be treated statistically, such that the sum of probabilities from all channels is unity. This model depends on three key ingredients, the optical model potential, the transmission coefficients and related γ-ray strength function, and the nuclear level density.

The transmission coefficient quantifies the probability that the compound nucleus will form via a particular entrance channel a and decay through a specific exit channel. It can be thought to describe how "open" a channel is to formation or decay. Each transmission coefficient calculated for the excitation energy E^*, spin J, and parity π of the CN states. For a compound nucleus reaction given by

$$a + A \rightarrow C^* \rightarrow b + B, \tag{2.26}$$

in which projectile a is incident on target A, followed by the formation of a compound nucleus in

an excited state C^*, and subsequent emission of particle or photon b and residual nucleus B. If we let α and β represent the entrance and exit channel, respectively, then the energy-averaged cross section from integration of a Breit-Wigner resonance [15] is

$$\langle \sigma_{\alpha\beta}(E) \rangle = \frac{\pi}{k^2} \left[\frac{2J+1}{(2J_a+1)(2J_A+1)} \right] \left\langle \frac{\Gamma_\alpha \Gamma_\beta}{\sum_c \Gamma_c} \right\rangle \frac{2\pi}{D}. \tag{2.27}$$

Here, the projectile wave number is given by $k = 2\pi/\lambda$, D is the level spacing between resonances, Γ is the resonance width corresponding to the channel, and J values are the total angular momentum of the CN, projectile (J_a), and target (J_A). Due to possible correlations in the average width term, we include a width fluctuation correction factor $W_{\alpha\beta}$:

$$\langle \sigma_{\alpha\beta}(E) \rangle = \frac{\pi}{k^2} \left[\frac{2J+1}{(2J_a+1)(2J_A+1)} \right] \frac{2\pi}{D} W_{\alpha\beta} \frac{\langle \Gamma_\alpha \rangle \langle \Gamma_\beta \rangle}{\sum_c \langle \Gamma_c \rangle}. \tag{2.28}$$

In the limit that $\Gamma \ll D$, we can set $W_{\alpha\beta} \approx 1$. The HF cross section can also be written in terms of transmission coefficients T, which are related to the average width $\langle \Gamma \rangle$, by $T = 2\pi \langle \Gamma \rangle / D$. Thus, the total cross section, obtained by taking the average cross section for all possible spin $J$and parity π levels populated in the compound nucleus, is given by

$$\sigma_{\alpha\beta}^{HF}(E) = \langle \sigma_{\alpha\beta}(E) \rangle = \frac{\pi}{k_\alpha^2} \sum_{J\pi} \frac{2J+1}{(2J_a+1)(2J_A+1)} \frac{T_\alpha^{J^\pi}(E)\, T_\beta^{J^\pi}(E)}{\sum_c T_c^{J^\pi}(E)}. \tag{2.29}$$

The first term is a statistical weighting factor that accounts for the number of possible couplings of the total angular momentum of the target J_A and the projectile spin J_a that give total angular momentum J of the compound nucleus . The numerator of the second term gives the probability that the CN forms through channel α and decays via channel β. The denominator is the total probability of decay through *any* channel c. The last term includes the HF branching ratio between different channels:

$$B_\alpha = \frac{T_\alpha}{\sum_c T_c}. \tag{2.30}$$

2.4.1 Optical Model Potential

The first HF ingredient we will discuss is the optical model potential (OMP). This quantity describes the interaction between the projectile and the nucleus, as well as the emitted particles and the nucleus. The OMP must take into consideration the possible outcomes that include absorption of the projectile into the target and scattering of the projectile from the target, as well as a mixture of both. The OMP is described as "optical" because it mimics the process of light being partially absorbed and partially scattered from an opaque refractive medium, a "cloudy crystal ball" in a sense. In the most simplistic model, the OMP can be described by the square-well potential with boundary conditions:

$$U(r) = -V_0 - iW_0 \quad r < \mathrm{R} \tag{2.31}$$

$$= 0 \qquad\qquad r > \mathrm{R}, \tag{2.32}$$

for which V_0 if the depth of the real potential and W_0 is the depth of the complex potential. A more realistic phenomenological model gives the OMP to be

$$U(R) = V(R) + iW(R), \tag{2.33}$$

in which the real part represents the average nuclear potential:

$$V(R) = -\frac{V_0}{1 + \exp\left(\frac{R-R_r}{a_r}\right)}, \tag{2.34}$$

and the imaginary part accounts for absorption:

$$W(R) = -\frac{W_0}{1 + \exp\left(\frac{R-R_i}{a_i}\right)}. \tag{2.35}$$

Both potentials take the form of the Woods-Saxon potential [16], for which a_r is the diffuseness of the potential and R_r is radius of the potential. Typically, the depths of each potential are between 40 and 50 MeV for the real part V_0 and 10 to 20 MeV for W_0 of the imaginary part. The radius of both is given by $R_{r,i} = r_0 A^{1/3}$ for a nucleus of A nucleon with $r_0 \approx 1.2$ fm, while the diffuseness parameter $a_{r,i}$ is about 0.6 fm. Fig. 2.2 shows the shape of the imaginary and real potentials.

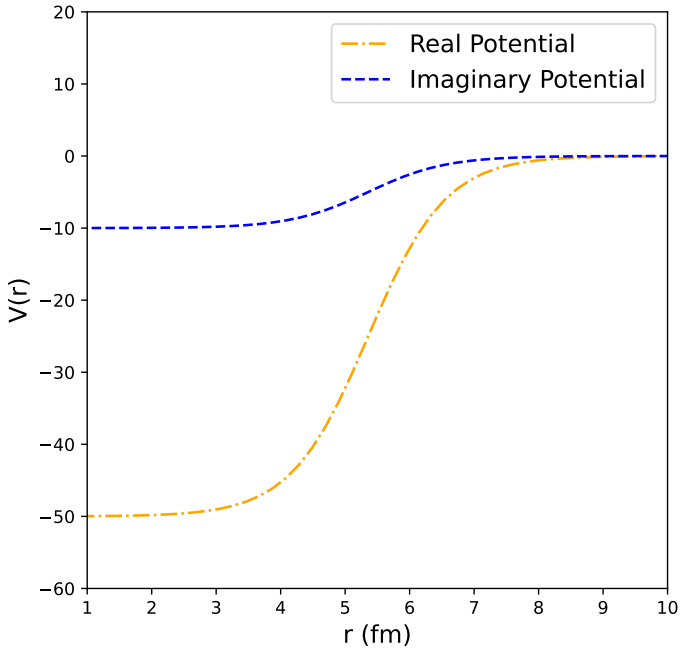

Figure 2.2 Simplified optical model potential of a Woods-Saxon shape. The imaginary potential is shown in blue and the real potential in orange.

Rather than the phenomenological model of the Woods-Saxon shape, OMPs can be described by microscopic models, such as the double-folding models from nucleon-nucleon (N-N) interactions, in which the (N-N) interaction potential is integrated with the density of the target in one of the foldings and with the projectile density in the other folding. The OMP can be used to calculate the transmission coefficients that govern the probability of each channel.

2.4.2 Nuclear Level Density

The nuclear level density $\rho(E_x, J, \pi)$ is defined as the number of levels with spin J and parity π that exist at excitation energy E_x per unit energy. The general form of the total level density is given by the sum of level densities over all J and π,

$$\rho^{tot}(E_x) = \sum_J \sum_\pi \rho(E_x, J, \pi). \tag{2.36}$$

The level density for a state with (E_x, J, Π) can be factorized into

$$\rho(E_x, J, \pi) = P(E_x, J, \pi) R(E_x, J) \rho^{tot}(E_x), \tag{2.37}$$

where $P(E_x, J, \Pi)$ is parity distribution, which can be assumed to be 1/2 in many cases, and $R(E_x, J, \Pi)$ is the spin distribution. The total level density can then be described by analytical expressions, as well as microscopic and phenomenological models. The analytical Fermi gas (FG) model by Bethe [17] describes the nucleus as a collection of non-interacting fermions, assuming that single particle states of the excited levels are equally space and that there is no collective motion of the nucleus [17]. The FG level density is given by

$$\rho_{FG}^{tot}(E_x) = \frac{\sqrt{\pi}}{12} \frac{e^{2\sqrt{aE_x}}}{a^{1/4} E_x^{5/4}}, \tag{2.38}$$

where a is the level density parameter that can be experimentally determined with the average s-wave resonance level spacing at the separation energy S_n. Realistically, the nucleons within the nucleus are indeed interacting. To account for nucleon pairing effects, the back-shifted Fermi gas (BSFG) phenomenological model was developed. The BSFG models includes an energy shift that represents the energy required to break apart a nucleon pair before excitation of a single nucleon can occur [18]. The BSFG model is expressed as

$$\rho_{BSFG}^{tot}(E_x) = \frac{1}{\sqrt{2\pi}\sigma} \frac{\sqrt{\pi}}{12} \frac{e^{2\sqrt{aU}}}{a^{1/4} U^{5/4}}, \tag{2.39}$$

where $U = E_x - \Delta$ is the energy shift that accounts for pairing effects. In practice, Δ and a are free parameters that can be adjusted to reproduce experimental data. Another NLD model is the constant temperature (CT) model [19], given by

$$\rho(E) = \frac{1}{T} e^{(E - E_0)/T}, \tag{2.40}$$

in which T and E_0 are introduced as free parameters. It has been shown by [19] that the CT model does well to describe the level density at low excitation energy up to an energy E_x, above which the FG model can be used to describe the higher energy level density. The analytical level density models are depicted in Fig. 2.3. Alternatively, The BSFG can describe NLD over the entire energy energy range if the pairing energy shift Δ is used as a free parameter for fitting experimental NLD.

Microscopic models are more complicated, but may better predict experimental data. Several semi-microscopic models can be used to calculate ρ^{tot} for large energy and spin ranges, including

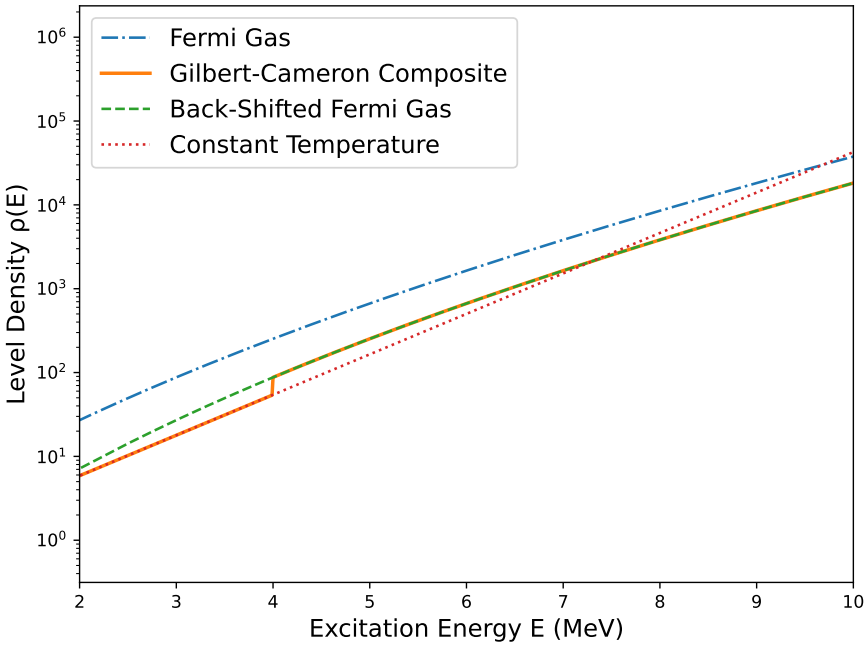

Figure 2.3 Analytical level density models: Fermi gas model (blue dash-dotted), back-shifted Fermi gas (green dashed), constant temperature (red dotted), and the Gilbert-Cameron composite (orange solid)

the Hartree-Fock model [20], the deformed Skyrme-HFB plus combinatorial model that includes an intrinsic state density and collective enhancement [21], and a temperature-dependent HFB model with the Gogny force [22]. The semi-microscopic level densities are provided as tabulated files available from the `RIPL-3` database [23] and can be scaled to match experimental data by

$$\rho(E, J^\pi) = \exp\left(c\sqrt{E-\delta}\right)\rho_{HFM}(E-\delta, J^\pi). \tag{2.41}$$

The adjustable parameters c and δ are the y-scaling factor and pairing shift energy, respectively. Another important term related to the NLD is the spacing between levels of the same spin and parity J^π. The level spacing D given by the sum of level densities for the spin range $J = I \pm 1/2$:

$$\frac{1}{D} = \sum_{J=|I-\frac{1}{2}|}^{J=I+\frac{1}{2}} \rho_{FG}(E_x, J^\pi). \tag{2.42}$$

I is the spin of the target nucleus and an s-wave neutron has spin $1/2$. Generally, the target nucleus

in its ground state with $I = 0$, so the level spacing at the neutron separation energy is

$$\frac{1}{D_0} = \rho(S_n, 1/2+). \tag{2.43}$$

2.4.3 γ-ray Strength Function

The γ-ray strength function (γSF), is related to the γ-ray transmission coefficient T_γ that gives the probability for a state to decay via the γ emission channel. The γSF describes the probability distribution for a γ ray of energy E_γ to be emitted during the transition from an excited state to a lower energy level. Both γSF and T_γ are important for the calculation of radiative reaction cross sections, specifically radiative capture (n,γ) and photodisintegration (γ,n).

In order to better understand the γSF, let us separate the function into upward and downward functions. The upward γSF $\overrightarrow{f_{X\ell}}(E_\gamma)$ relates to the γ-ray absorption cross section of (γ, n) reactions in the energy range $E_\gamma > S_n$. The photoabsorption cross section, given by

$$\sigma_{(\gamma,abs)}E_\gamma = \sum_{X\ell} \sigma_{X\ell}(E_\gamma), \tag{2.44}$$

is the sum of all cross sections for γ rays of type X (electric E or magnetic M) and multipolarity ℓ. It is related to the upward γSF by,

$$\overrightarrow{f_{X\ell}}(E_\gamma) = K_{X\ell}\frac{\sigma_{X\ell}(E_\gamma)}{E_\gamma^{2\ell-1}} \tag{2.45}$$

where,

$$K_{X\ell} = \frac{1}{(2\ell+1)\pi^2\hbar^2c^2}. \tag{2.46}$$

Meanwhile, the downward γSF is related to the γ-ray transmission coefficient T_γ by

$$T_\gamma^{X\ell}(E_\gamma) = 2\pi\overleftarrow{f_{X\ell}}E_\gamma^{2\ell+1}, \tag{2.47}$$

which determines the competition between photon emission and emission of other particles. The average resonance width of the γ channel $\langle\Gamma_\gamma\rangle$ is given by the integration of T_γ over the level density of final states that can be accessed by γ rays first emitted from the decay of the CN:

$$\frac{2\pi\langle\Gamma_\gamma\rangle}{D_0} = \sum_J \sum_\Pi \sum_{X\ell} \sum_{I'=|J-\ell|}^{J+\ell} \sum_{\Pi'} \int_0^{S_n} dE_\gamma T_{X\ell}(E_\gamma)\rho(S_n - E_\gamma, I', \Pi')F(X, \Pi', \ell). \tag{2.48}$$

D_0 is the level spacing at S_n and F is determined by the multipolarity selection rules, given by

$$F(E, \pi', \ell) = 1 \text{ if } \Pi = \Pi'(-1)^{\ell} \tag{2.49}$$

$$F(M, \pi', \ell) = 1 \text{ if } \Pi = \Pi'(-1)^{\ell+1}. \tag{2.50}$$

The integral is summed over J, Π of the CN initial states, $X\ell$ character of the emitted radiation, and I', Π' of the CN final states. Recalling Eq. 2.29, the cross section can be written as a ratio of the transmission coefficients for particular channels over the sum of all coefficients. Considering only the n and γ channels, and in the limit that $\Gamma_n \gg \Gamma_\gamma$, the cross section can be given by

$$\sigma(n, \gamma) = \frac{T_n T_\gamma}{T_n + T_\gamma} \approx T_\gamma \tag{2.51}$$

$$= \sum_J \sum_\Pi \sum_{X\ell} \sum_{I'=|J-\ell|}^{J+\ell} \sum_{\Pi'} \int dE_\gamma T_{X\ell}(E_\gamma) \rho(S_n - E_\gamma, I', \Pi') F(X, \Pi, \ell). \tag{2.52}$$

The Brink hypothesis [24] tells us that the upward and downward γSFs are approximately equal, such that

$$f_{X\ell} = \overleftarrow{f_{X\ell}} = \overrightarrow{f_{X\ell}}. \tag{2.53}$$

Thus, above S_n we have a good description of the γSF from the (γ,n) cross section and below, (n,γ) cross sections provide a good description. Additionally, measurements made in these regions can constrain the γSF. For example, the Oslo or β-Oslo methods can be used to extract the γSF below the separation energy through population of the statistical states. The total γSF is determined by summing over the individual $f_{X\ell}$ for all X and ℓ values.

The first analytical model of the γSF is the standard Lorentzian model (SLO) [24, 25], which describes the shape of the giant dipole resonance (GDR):

$$f_{X\ell}(E_\gamma) = K_{X\ell} \frac{\sigma'_{X\ell} E_\gamma \Gamma'^2_{X\ell}}{(E_\gamma^2 - E_{X\ell}^2)^2 + E_\gamma^2 \Gamma'^2_{X\ell}}. \tag{2.54}$$

The SLO parameters are the GDR width $\Gamma'_{X\ell}$, GDR energy $E_{X\ell}$, and GDR strength $\sigma'_{X\ell}$. Prime accents are used to distinguish between the SLO parameters and previously defined HF quantities. A phenomenological model commonly used is the Kopecky-Uhl generalized Lorentzian (GLO)

model [26], in which we assume electric dipole radiation dominates the shape of the γSF. The GLO model is expressed by

$$f_{E1}(E_\gamma) = K_{E1}\left[\frac{E_\gamma \tilde{\Gamma}_{E1}}{(E_\gamma^2 - E_{E1}^2)^2 + E_\gamma^2 \tilde{\Gamma}_{E1}} + \frac{0.7\ \Gamma_{E1} 4\pi^2 T^2}{E_{E1}^5}\right]\sigma_{E1}\Gamma_{E1}, \tag{2.55}$$

where $\tilde{\Gamma}_{E1}$ is the energy-dependent damping width,

$$\tilde{\Gamma}_{E1} = \Gamma_{E1}\frac{E_\gamma^2 + 4\pi^2 T^2}{E_{E1}^2}, \tag{2.56}$$

and T is the nuclear temperature. Fig. 2.4 compares the slight difference in shape between the SLO and GLO. For some nuclei, there is an additional region of strength at lower energy than that of the GDR called the Pygmy resonance. To include this feature in the total γSF, simply add another term in the form of Eq. 2.54.

In addition to the GDR and Pygmy $E1$ resonances, it has been observed in many isotopes that the γSF increases in strength at $E_\gamma < 2$ MeV, and was first measured in iron isotopes ^{56,57}Fe [27]. This phenomenon has been named the low-energy enhancement (LEE) or the "upbend." Since its discovery, significant research has been focused on the upbend as it strongly diverges from theoretical predictions of the γSF at low energy. Multiple studies experimentally confirmed the existence of the upbend [28, 29, 30, 31]. Since its discovery, many experiments have also detected an upbend in many isotopes across the nuclear chart, however, it does not always appear []. This is significant, because such a diversion from theory can strongly affect nucleosynthesis abundances, especially for reactions that have not been directly measured and must be calculated from theory alone. It is not clear whether the LEE arises from $E1$ or $M1$ radiation, but it was shown to be dipole in nature [31]. A recent publication by Chen *et al.* [32] applied a novel theoretical shell-model method to weakly deformed nuclei. They propose that the upbend is the result of a new collective motion called the scissors rotation, and state the the LEE is a feature of all weakly-deformed nuclei, regardless of mass.

Beyond the analytical and phenomenological models described so far, several microscopic models can be used to describe the γSF. They include the Skyrme-Hartree-Fock-Bogoliubov (HFB) model, calculated with the quasiparticle random-phase approximation (QRPA) [33], the

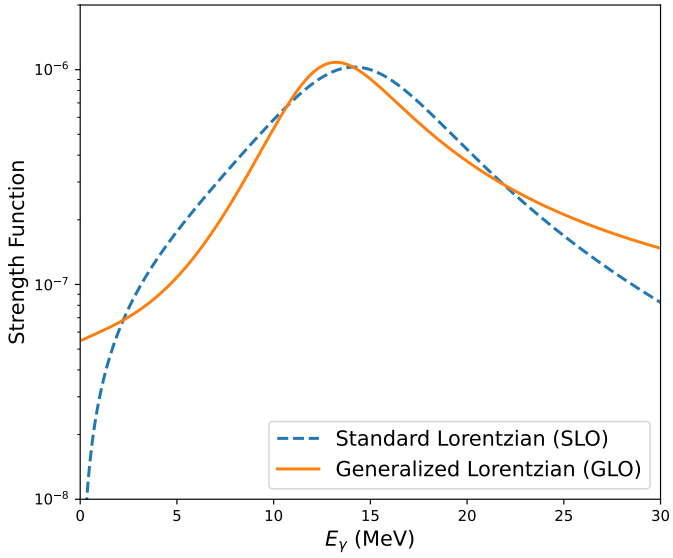

Figure 2.4 The SLO (blue dashed) and GLO (orange solid) γ-ray strength functions for generic parameters.

temperature-dependent Skyrme-HFB model [33], and the Gogny-HFB model [34] that includes the Gogny force with QRPA.

2.4.4 Direct vs. Indirect Techniques

As discussed previously, direct measurements of neutron- and proton- capture reactions provide crucial information to better understand stellar reactions and their effect on nucleosynthesis. Typical capture experiments involve a beam of accelerated particles impinged on a stationary target. The beam can be stable or radioactive, and the target is stable or consists of long-lived isotopes with a half-life on the scale of at least days. As experimental measurements move toward the driplines, targets become unrealistic. For n-capture, either the beam or target must consist of only neutrons.

Given these points, direct capture of neutrons is very nearly impossible today. Some efforts are underway but still far from ready. Indirect methods are needed to measure quantities from which we can infer information about the CN. Several methods include, photodisintegration reactions (γ, n), the Oslo method which utilizes transfer reactions, such as (d, p), the β Oslo method, which populates states in the CN through β decay, the surrogate method, and the γSF method [5]. These methods take advantage of the statistical nature of the CN, for which the Hauser-Feshbach

formalism, discussed in Sec. 2.4, can provide a framework to extract CN cross sections.

2.5 Detector Physics

The last section of this chapter is on the subject of the γ-ray detection mechanism, which will be relevant to the discussion in Sec. 4.1.

2.5.1 Interactions of Photons with Matter

Detection of γ rays involves understanding the various ways in which photons interact with matter. A γ ray can interact with matter via the photoelectric effect, Compton scattering, and pair production, illustrated in Fig. 2.5. Each interaction produces a unique signature in the γ-ray spectrum, a representation of which is shown in Fig. 2.6.

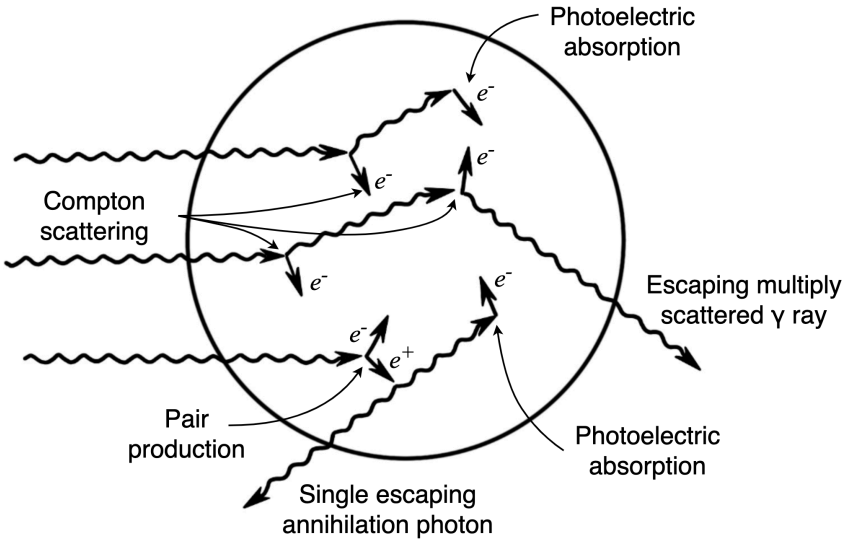

Figure 2.5 Illustration of γ-ray interactions in a medium-sized NaI(Tl) detector. Image adapted with permission from Fig. 10.4 of [12]

An incident γ ray that undergoes the photoelectric electric effect within the volume of a detector transfers all of its energy to an electron which subsequently deposits its energy in the detector material. This appears as a single peak in the γ-ray spectrum at the energy of the γ ray, called the photopeak, or full energy peak.

During Compton scattering, the incident photon scatters from a loosely-bound electron, im-

parting some fraction of its energy in the electron. In a sufficiently large detector, such as the SuN detector [6], a single γ ray may scatter multiple times before being fully absorbed through the photoelectric effect. The energy spectrum from Compton scattering is a continuum from $E = 0$ to the "Compton edge" where the distance between the full energy peak and Compton edge is given by $E = E_\gamma - E_{e^-}$. Multiple Compton scatters by the same incident photon create a continuous background on which the photopeak sits. Another possibility is that the incident photon may instead Compton scatter from the material that surrounds the detector, in which case the photon is back-scattered and may get absorbed at $E_\gamma \approx 200$ keV, in what is called the back scatter peak.

High energy photons are likely to undergo pair production. A photon near the strong electric field surrounding the nucleus can disappear while an electron-positron pair is created. The incident photon must have a minimum energy of 1.022 MeV for pair production to even be possible. The two particles are able to travel a few millimeters before losing all kinetic energy to the detection medium. The newly-created positron, an antimatter particle, will annihilate when it comes in contact with a free electron in the detector, in which both particles disappear and two 511 keV photons are emitted in opposite directions. If both photons are absorbed, the full energy will be preserved. However, if one or both annihilation photons escape the detector without further interaction, then the energy spectrum will contain 1-2 additional peaks, the single and double escape peaks. The single escape peak is located at $E = E_\gamma - 511$ keV and the double escape peak at $E = E_\gamma - 1022$ keV.

2.5.2 NaI(Tl) Detectors

NaI(Tl) detectors are a type of alkali halide scintillator that consist of a solid sodium iodide crystal that has been doped with trace amounts of thallium iodide. They were first used in 1948 and continue to see use today. Although they have worse energy and time resolution compared to other types of detectors, such as HPGe, NaI(Tl) detectors have a higher detection efficiency, their crystals can be grown into large volumes of unique shape, and are relatively affordable. Photomultiplier tubes (PMTs), which are devices that use the photoelectric effect to amplify electron signals, may be attached directly to the crystal and are used to detect the scintillator light produced in the detector.

NaI(Tl) is an inorganic crystal that has a lattice structure. It's band structure, depicted in Fig.

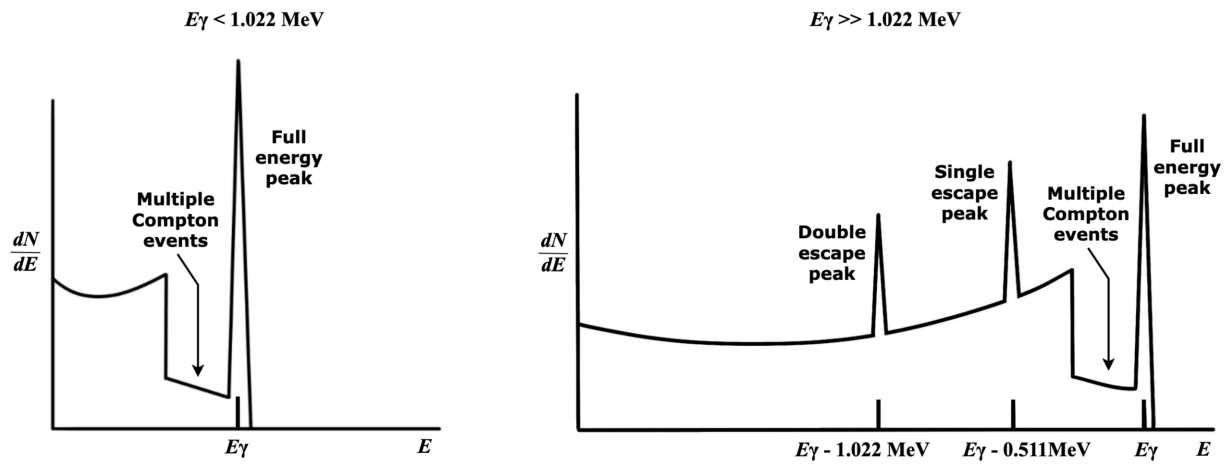

Figure 2.6 Illustrations of the γ-ray spectrum of a NaI(Tl) detector for lower energy γ rays (left) and γ rays of higher energies (right). Image adapted with permission from Fig. 10.4 of [12]

2.5, is composed of a valence band of electrons bound to the lattice and a conduction band of free electrons that can move throughout the crystal. The bands are separated by a large band gap, and when a γ ray with enough energy to overcome the band gap interacts with the crystal, an electron from the valence band may be excited to the conduction band. After some time the excited electron will relax back to the valence band, producing a photon as it de-excites. In a pure crystal, electrons are forbidden from occupying energy levels that fall within the band gap, therefore the photons emitted have too high of an energy to be detected by PMTs. This challenge is quelled through the addition of small amounts of impurities, called activators, that create bands within the forbidden energy region. In the case of NaI, thallium provides the additional levels, also shown in Fig. 2.7. Photons that undergo the photoelectric effect in the detector produce a photoelectron with a large amount of energy. As the photoelectron passes through the crystal, many electrons from the valence band are excited to the conduction band. These electrons will eventually de-excite through the activator states, thus transferring the initial γ-ray energy into low energy scintillator photons. The maximum wavelength of scintillator photons is 415 nm, which is within the PMT wavelength detection range.

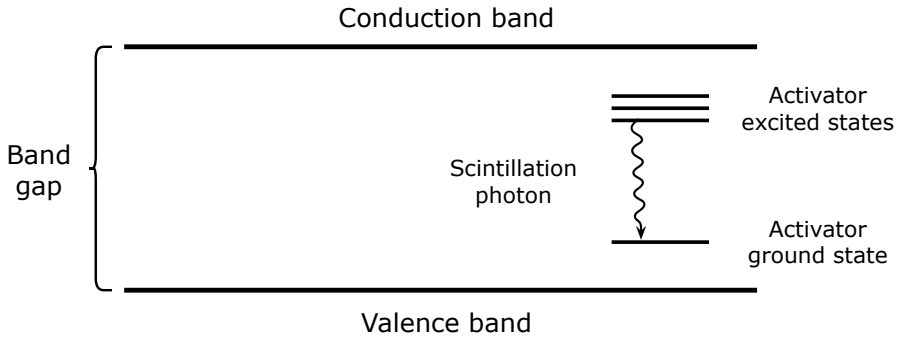

Figure 2.7 Illustration of activator states in NaI(Tl) crystal. Reproduced with permission from [12]

CHAPTER 3

NUCLEAR ASTROPHYSICS

The study of nuclear astrophysics requires involvement from four primary fields: astronomy, astrophysics, experimental nuclear physics, and theoretical nuclear physics. Each field contributes important pieces of the puzzle that is the origin of the elements. Astronomers observe astrophysical events and analyze data across many wavelengths of the entire electromagnetic spectrum. They also study the composition of meteorites that may contain early signatures of nucleosynthesis. Astrophysicists develop predictive computational models that simulate astrophysical environments from the stellar to galactic scale, in order to further understand our observations and make predictions. Stars are essentially massive nuclear reaction that can only be contained by the their own gravity, hence, nuclear physicists are needed to understand the nuclear reactions and properties that drive such extreme environments. Where the limits of experiments end, nuclear theorists fill in the knowledge gaps with theoretical models that can predict nuclear properties of isotopic regions that are currently inaccessible to experiment but regardless, still important for our understanding of stars. These four fields intermingle, each one motivating another to push the boundaries of knowledge in this epic age of multi-messenger astronomy.

3.1 Big Bang Nucleosynthesis

Thirteen point eight billion years ago, the universe erupted in a great expansion. Within the first second, the thermal energy ($E > 1$ MeV) was high enough to create the first particles: protons, neutrons, and electrons. They existed in statistical equilibrium in which neutron and protons were constantly converted into one another and electron-positron annihilation produced γ rays that in turn had enough energy to create e^-e^+ pairs. After 2 seconds, the thermal energy dropped below 1 MeV, which allowed protons and neutrons to exist without constant conversion. Over the next 250 seconds, primordial nucleosynthesis occurred in which protons and neutrons combined to form the first elements H, He, and trace amounts of Li. The first capture reaction to happen was the reaction that forms deuterium (^{2}H or d),

$$\mathrm{n} + \mathrm{p} \rightarrow \mathrm{d} + \gamma, \tag{3.1}$$

which then made the reactions that form tritons (^{3}H or t), ^{3}He, and ^{4}He possible. The ratio of neutrons to protons is given by the Saha equation,

$$\frac{n_n}{n_p} \approx exp\left(\frac{(m_n - m_p)c^2}{k_B T}\right), \tag{3.2}$$

where k_B is the Boltzmann constant, $m_{n,p}$ are the masses of the neutron and proton, and T is the temperature. At the beginning of this period of nucleosynthesis, $k_B T \gg (m_n - m_p)c^2$ which meant that there were approximately the same numbers of neutrons and protons. However, as the environment cooled, "freeze out" ensued when the ratio shrank to $m_n/m_p \approx 1/8$, and at $t \approx 250$ s, all reactions stopped with the exception of the β decays of neutrons, tritons, ^{7}Be. Once all radioactive species had decayed, the universe was composed of p, d, ^{3}He, ^{4}He, e^-, γ, and ν_e, with protons making up 75%.

The early universe had to cool for 380,000 years until the thermal energy was low enough for the first atoms to form. At $E \sim 0.4$ eV, electrons could remain bound to nuclei without immediately ionizing. The Cosmic Microwave Background is the observational evidence of this young universe, detectable from every direction in the sky. 200 million years after the big bang, gas and dust were compressed enough to ignite the first stars, and galaxies formed after 400 million years. Fig. 3.1 depicts the timeline of the universe, from the big bang 13.8 million years ago to today.

3.2 Stellar Burning

3.2.1 Hydrogen Burning

When gas and dust are compressed enough, hydrogen burning, the first stellar burning process, is ignited and a star is formed. The hydrogen-burning phase is fueled by the *p-p* chain reactions, which are the slowest and least probable reaction in stellar burning. The reaction is governed by the weak force and has cross sections of the order $\sim 10^{-33}$ barns for protons with energy on the scale of keV and $\sim 10^{-23}$ barns in the MeV energy scale. The low reaction rate allows stars to spend a long time in this phase of their life cycle.

Initially, the two protons fuse to produce a deuteron (^{2}H or d), positron (e^+), and neutrino (ν_e):

$$p + p \rightarrow {}^2H + e^+ + \nu_e \tag{3.3}$$

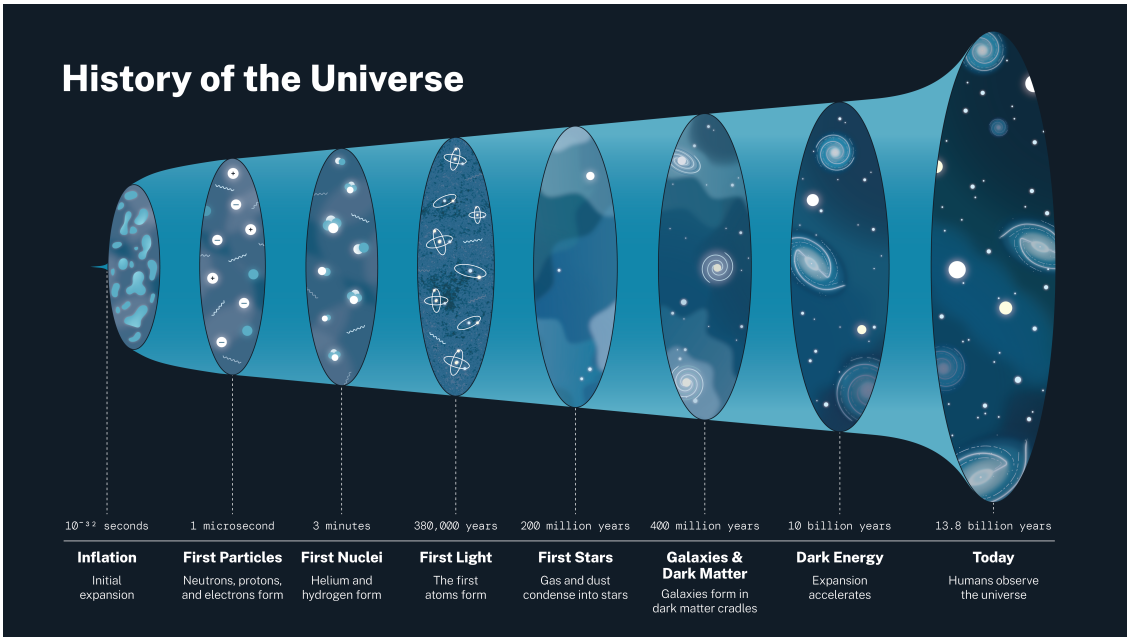

Figure 3.1 Illustration of the timeline of our universe. From nasa.com

In a star similar to the sun, 1 deuteron nucleus (1 proton, 1 neutron) is formed for every $\sim 10^{18}$ protons. The deuteron can subsequently consume another proton to form ^{3}He (2 protons, 1 neutron). Once enough ^{3}He has built up, two ^{3}He nuclei can fuse forming one helium nucleus (^{4}He) with the release of two protons. The net reaction of the *p-p* chain to form a single ^{4}He nucleus can be summarized by

$$4\mathrm{p} \rightarrow {}^4\mathrm{He} + 2\mathrm{e}^+ + 2\nu_e + 26\ \mathrm{MeV}, \tag{3.4}$$

The large amount of energy released increases the outward radiation pressure, hence supporting the stellar core against gravitational collapse. Stars burn hydrogen for their entire lives in the stellar life stage called the Main Sequence (MS), which can last for billions of years. When plotted on a Hertzsprung-Russell (HR) diagram, which has surface temperature (color) on the x-axis and luminosity (brightness) on the y-axis, a star burning hydrogen sits on the MS line. Fig. 3.2 shows an HR diagram for a collection of stellar data. Interestingly, stars do not sit uniformly across the plot, but rather, clump together in specific locations. The position of the star can provide insight on other stellar quantities, such as the mass, age, chemical composition, and evolutionary phase; neighboring stars share many of these quantities. The MS lies diagonally across the plot, where massive stars fall on the hotter, brighter end of the MS, while lower mass stars are cooler and

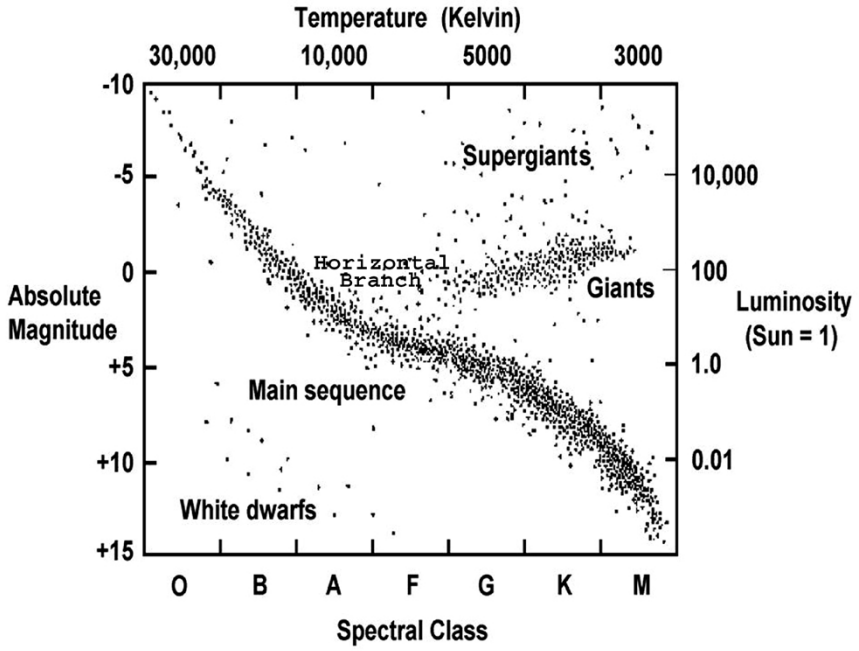

Figure 3.2 HR diagram for a collection of stars. The x-axes are surface temperature (top) and spectral class (bottom); y-axes are absolute magnitude (left) and luminosity (right). Labels are provided for notable groupings of stars, including the Main Sequence, Horizontal Branch, Giants, Super Giants and White Dwarfs. (Image from https://chandra.harvard.edu/)

dimmer. 90% of stars are located along the MS. Once the star has burned the hydrogen in the core, it leaves the MS path, beginning its journey toward the end of its life.

More recent generations of stars, stars that form in the remnants of older stars that have died, can contain elements other than hydrogen at their conception. They typically have impurities of carbon, oxygen, and neon, the ashes of helium burning. In these stars, another form of hydrogen burning can occur. Instead of fusing protons, ^{12}C acts as a catalyst to convert protons to alpha particles. The net reaction of the CNO cycle is in fact the same as that of the *p-p* chain process, given by $4p \rightarrow {}^4He + 2e^+ + 2\nu_e$, however, the CNO cycle proceeds more quickly than the latter process.

3.2.2 Helium Burning

Once the hydrogen has been exhausted in the core, the outward pressure from nucleosynthesis ceases, allowing unopposed gravitational force to compress the core. As the core contracts, temperature increases to the point that hydrogen burning ignites in the hydrogen shell around the

helium core. The increase in thermal pressure causes the outer layers to expand; expansion cools the outer layers and the star sets out on the Red Giant Branch (RGB) track of stellar evolution. As the star compresses, the pressure and temperature continue to increase, and the hydrogen-burning shell adds more and more mass to the central region of the star. Eventually, core helium burning will ignite, once again producing thermal energy that can balance gravitational contraction.

Two ^{4}He, or α particles, cannot form a bound state, but there exists a small low-lying energy resonance in the unbound ^{8}Be nucleus with a lifetime just long enough for a third α particle to be captured. The so-called triple-α process forms an excited ^{12}C nucleus that de-excites by γ decay. Subsequently, the ^{12}C nucleus can now capture an addition α particle to form ^{16}O, and then alpha capture again to form ^{20}Ne.

In stars with mass $0.5\ M_\odot < M < 2\ M_\odot$ (solar mass), helium burning begins with an event called a helium-core flash. In this mass region, the helium core becomes degenerate, with only electron degeneracy pressure supporting the core against gravitational collapse. Continued contraction increases the heat, but there is no thermal energy that can regulate the temperature by expanding the core. When the central temperature reaches that required to ignite helium, the fusion energy released increases the temperature, which increases the fusion rate, leading to thermonuclear runaway. At this point in the star's life, the star is located in the Horizontal Branch (HB) of the HR diagram, and will quiescently burn helium until the nuclear fuel is depleted in the core.

Once core helium has been exhausted, the star once again contracts, heating and subsequently expanding and cooling the outer layers. The core now consists of mostly carbon and oxygen, surrounded by a helium-burning shell, a hydrogen-burning shell, and a hydrogen envelope. The star again grows in luminosity and reddens, becoming a red giant on the Asymptotic Giant Branch (AGB), named "asymptotic" because it nearly aligns with the previous red giant path. Stars of mass $9\ M_\odot < M < 11\ M_\odot$ can reach a central temperature high enough to ignite carbon burning in their cores, producing oxygen, neon, sodium, and magnesium. In addition, neutrons are produced during carbon burning, as follows,

$$^{12}\mathrm{C} + {}^{12}\mathrm{C} \rightarrow {}^{24}\mathrm{Mg} + \mathrm{n} - 2.6\ \mathrm{MeV}, \tag{3.5}$$

which is important for heavy element nucleosynthesis, discussed in Sec. 3.4.

During the AGB phase, helium is burning in a thin shell surrounding the contracting core, and shell-hydrogen burning is powered by both the pp chain and the CNO cycle. The ashes of hydrogen burning, i.e. helium, builds up between the two burning layers. The increasing mass experiences increasing temperature and pressure until helium burning erupts. Similar to the He-core flash, the ignition of the helium layer burns at a rate that cannot be radiated outward, and thus thermonuclear runaway occurs in a helium-shell flash. This enormous burst of energy pushes out the hydrogen-burning layer, extinguishing nuclear burning. The star continues to expand eventually cooling to a temperature that cannot sustain helium burning, and once again, the star contracts, hydrogen burning is re-ignited, and the thermal-pulse (TP) process repeats every $\sim 10^5$ years. The TP-AGB stage is very short relative to the star's MS lifetime. Between thermal pulses, strong convective mixing occurs, each pulse "dredging up" deeper, more-processed material to the surface, and changing its observed chemical composition.

The star becomes a post-asymptotic giant branch star (post-ABG) with the last thermal pulse ends. AGB stars develops a stellar wind that pushes away the outer layers which results in significant mass loss. As more and more of the hydrogen envelope blows away, hotter layers are exposed, which ionizes the surrounding ejected material, creating a planetary nebula (PN). At the PN center is a white dwarf (WD), a compact stellar object consisting of carbon-oxygen ($0.4\ M_\odot < M < 9\ M_\odot$) or oxygen-neon ($9\ M_\odot < M < 11\ M_\odot$). Left alone, the WD will continue to radiate energy and fade away.

3.3 Advanced Burning Stages

Massive stars ($M > 11\ M_\odot$) begin their life on the MS, just like lower mass stars, however their time is drastically reduced, spending only millions of years in the hydrogen-core burning stage, rather than billions. Their massive size produces stronger gravitational compression, which results in hotter temperatures throughout the star. When hydrogen-core burning ceases, the core contracts, heats up, and helium-core burning ignites with a surrounding hydrogen-burning shell. Fig. 3.3 shows the HR diagram track of a massive star compared to that of the sun. As core nuclear fuel

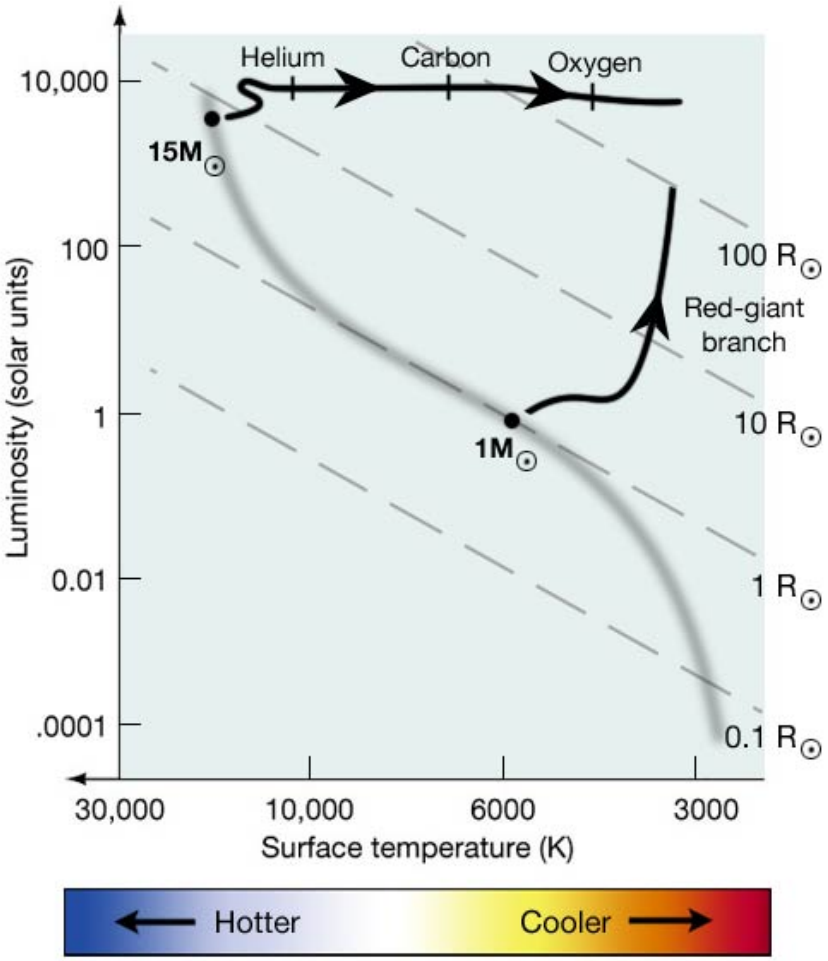

Figure 3.3 HR diagram depicting the evolutionary path of a massive star and a star of solar mass. (Image: Penn State Astronomy & Astrophysics)

is extinguished, the process of contraction-heating-ignition repeats with each subsequent fuel type. After core-burning phases of helium, carbon, neon, oxygen, and silicon, the star consists of an iron core surrounded by layers of nuclear ashes separated by thin burning shells of each prior phase, illustrated in Fig. 3.4. Advanced burning stages release energy by radiating neutrino-antineutrino pairs, and each successive burning phase is shorter than the previous, with silicon-core burning lasting only $\sim$ 1 day. The star's evolution accelerates at such a high rate that convective mixing cannot occur within the rapidly decreasing burning time frame.

Under the stars enormous gravity, the iron core becomes degenerate and continues to grow in mass as more nuclear ashes are produced. Eventually, the core reaches the Chandrasekhar limit

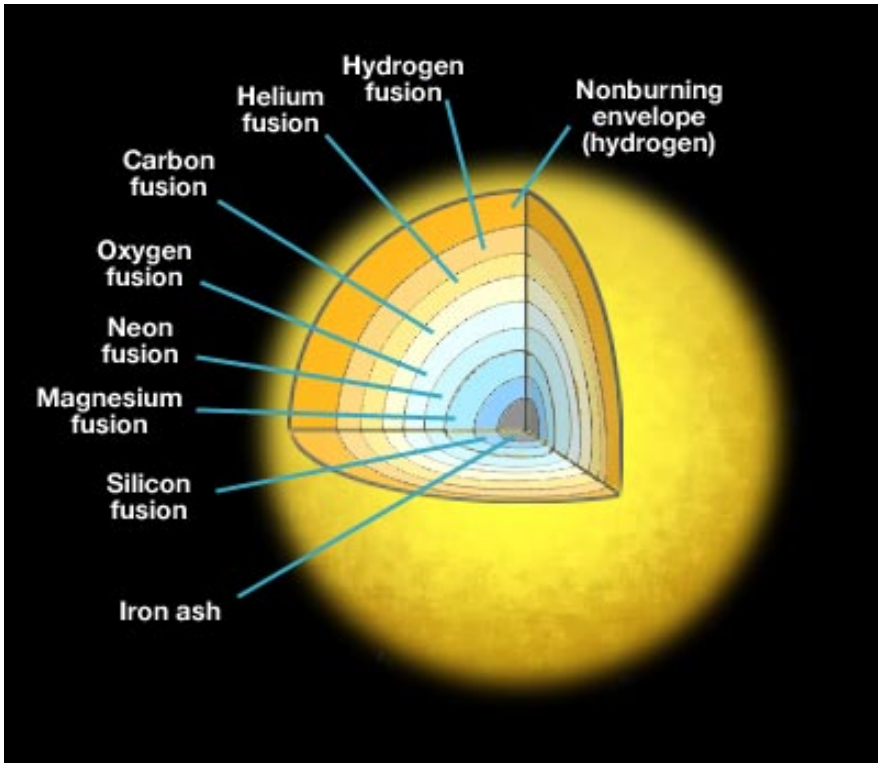

Figure 3.4 Illustration of the interior of a massive star at the end of stellar burning processes. (Image: Penn State Astronomy & Physics)

($\approx$ 1.4 $M_\odot$) and collapses. Density increases to that of nuclear matter ($\approx$ 10^{14}g/cm^3), and the nuclear strong force causes the in-falling material to rebound off the core, which produces a shock wave and leaves behind a neutron star. During the seconds it takes for the shock wave to travel out from the core, explosive nucleosynthesis proceeds, producing radioactive ^{56}Ni among other iron peak nuclei. Core collapse of massive stars are classified as supernovae (SNe) of types II and Ib/Ic. Astronomers can observe the light curve associated with supernovae and, using models, can determine which nuclei are present. The observation of radioactive nuclei with relatively short half-lives provides evidence for the nucleosynthesis occurs during these events.

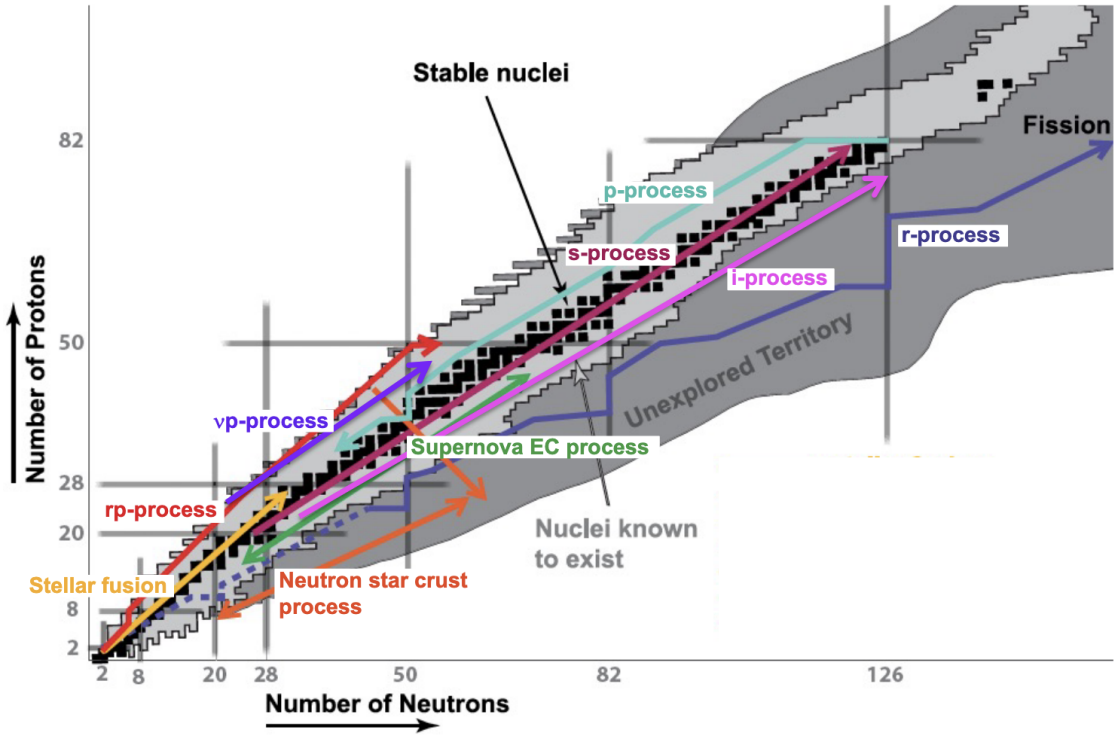

Figure 3.5 Chart of nuclei with nucleosynthesis processes displayed. (Image: Schatz 2022 J.Phys.G A Nucl. Part. Phys. 49 110502)

3.4 Heavy Element Nucleosynthesis

Stellar burning is responsible for the creation of elements up to iron (Z = 26), however, fusion is not a viable mechanism to produce heavier elements, as the reactions are no longer exothermic. Instead, neutron-capture processes are predominantly responsible for creation of the heavy elements, as described in the landmark B^2FH paper published in 1957 [35]. Fig. 3.5 depicts the chart of nuclides with nucleosynthesis processes overlaid in their region of influence. The primary processes that will be discussed in the following sections are the s process, r process, and p process.

3.4.1 s process

In general, neutron-capture nucleosynthesis entails seed nuclei capturing neutrons and emitting a gamma ray in succession until a radioactive isotope is reached and, through beta decay, produces stable isotopes with higher Z. This mechanism depends on the neutron density, neutron flux, neutron-capture rates, and beta-decay rates.

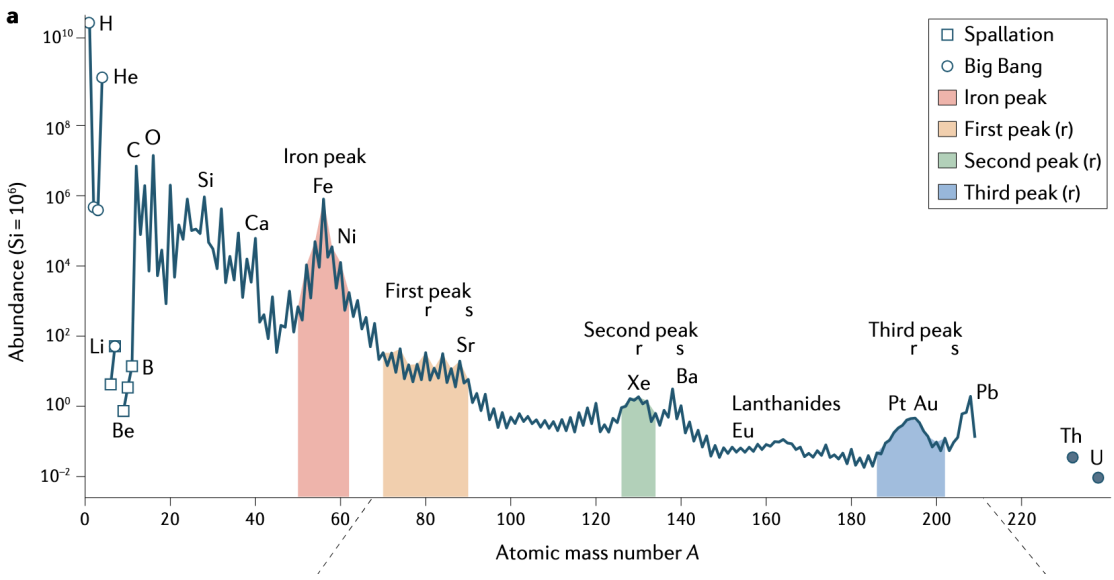

Figure 3.6 Solar System abundance pattern, with labels for s process and r process elements. (Image: D. Siegel, Nature Reviews Physics volume 4, pages 306–318 (2022))

The slow (s) process starts with the end products of stellar burning, namely ^{56}Fe nuclei, in an environment with neutron density $N_n \lesssim 10^{11}$ neutrons/cm^{-3}, in which neutron-capture rates are much smaller than corresponding beta-decay rates [cite]. The small neutron density and low neutron-capture rate result in a single neutron capture by a nucleus that will beta decay before capturing another neutron. In this scenario, nuclei along the valley of stability are slowly built up over a period of thousands of years. The s process is responsible for the synthesis of the majority of elements with mass numbers $23 \leq A \leq 46$, as well as a considerable portion of $63 \leq A \leq 209$ elements. Fig. 3.6 shows the abundance pattern of the sun with s-process peaks indicated by "s" label. The peaks are located at elements with A = 90, 138, 208 that correspond to nuclei with filled neutron shells at magic numbers N = 50, 82, 126. The s process is believed to occur in red giants, evidenced by radioactive technetium observed in the stellar atmosphere [cite].

3.4.2 r process

The rapid (r) process operates similarly to the s process, but at far shorter time scales ($\sim 0.01-10$ seconds) and significantly higher neutron density ($N_n \geq 10^{24}$ neutrons/cm^{-3}). Astrophysical r process environments involve (n,γ), λ_n, and (γ,n), λ_γ, rates that are much larger than β-decay rates, λ_β. A nucleus will continue to capture neutrons until $\lambda_n(A, Z) \approx \lambda_\gamma(A+1, Z)$, at which

point no further build-up can occur until beta decay increases Z. As nuclei approach the neutron drip line, β-decay rates shrink while neutron-binding energy decreases to zero. The abundance peaks for the r process are located at A = 80, 130, 194, about 8 − 14 neutrons from the magic numbers, shown in Fig. 3.6. This process is responsible for the synthesis of most elements with $70 \leq A \leq 209$. Evidence of r-process nucleosynthesis has been confirmed in the observed light curve of the neutron-star merger multi-messenger event GW170817, which agree with r-process models [36].

3.4.3 p process

Proton-rich nuclei (p-nuclei) are shielded by the stable isotopes from neutron-capture processes. The p process describes the mechanism that is responsible for the synthesis of p-nuclei and can be described by photodisintegration (p, γ) reactions on s- and r-process elements. The p process is believed to occur in type II supernova.

3.5 Intermediate i process

The intermediate (i) process was first proposed by Cowan and Rose in the 1970s [1]. They performed calculations that suggested a new neutron-capture process that is triggered in certain astrophysical environments where a neutron density of $N_{\mathrm{n}} \sim 10^{13-15}$ neutrons/cm^{-3} can be achieved. The proposed i-process neutron density is between those of the s and r process, with a predicted timescale on the order of minutes and reaction path several nucleons away from the stable isotopes. Recent observations of abundance distributions that could not be described by the s, r, or s+r process have been successfully predicted with i-process models [citations].

3.5.1 Astrophysical Environment

As for the s process, i-process neutrons are produced by the $^{13}\mathrm{C}(\alpha, \mathrm{n})^{16}\mathrm{O}$ reaction. The ^{13}C nuclei are replenished from the proton capture $^{12}\mathrm{C}(\mathrm{p}, \gamma)^{13}\mathrm{N}$ followed by the β decay $^{13}\mathrm{N}(\mathrm{e}^{+}\nu)^{13}\mathrm{C}$. In a stable stellar structure, the H-burning and He-burning layers remain separate. However, during a disruptive event, such as a He-shell flash, the convective zone extends from the He layer into the H-rich envelope. With strong mixing, ^{12}C is able to interact with protons in the H envelope forming ^{13}N, which can then be carried down to the He layer by convection. The mixing turnover time

scale is $\sim$ 15 minutes, long enough for ^{13}N to undergo beta decay ($T_{1/2}(^{13}N)$ = 9.96 minutes) into ^{12}C, which can then interact with the He-shell layer. Possible astrophysical sites for the i process include TP-AGB stars, post-AGB stars, super-AGB stars, rapidly accreting white dwarfs (RAWDs), and low-mass red giants undergoing a He-core flash [citations].

Sakurai's object (V4334 Sagittarii), a post-AGB star, is the first observation to show strong evidence for the i process. A carbon-oxygen white dwarf can undergo a He-shell flash that results in the star being "born-again" as an AGB red giant, a process called a late thermal pulse or very late thermal pulse (VLTP). Sakurai's object is believed to be such a star that is experiencing a VLTP, which was discovered in 1996 [37] and has been of interest to i-process modelers ever since.

3.5.2 Nuclear Input

Astrophysical models that simulate stellar evolution and predict abundance distributions require astrophysics, nuclear physics, and thermodynamic inputs. Examples of astrophysical input parameters include profiles for temperature, density, and radius, as well as diffusion coefficients from He-convective zone models. Nuclear physics parameters include nuclear masses, reaction rates, beta-decay rates, and beta-delayed neutron emission rates for all participating nuclei, which adds up to thousands of possible input values. Uncertainties exist for every parameter, but neutron-capture rates are of particular interest because very few (n, γ) rates have been measured for radioactive isotopes. Hence, the vast majority of reaction rates are determined by theory alone which are less accurate further away from the stable isotopes. Reducing (n, γ) reaction rate uncertainties will ultimately reduce model uncertainty and improve predictive power.

3.5.3 Sensitivity Studies

The observed abundance distribution of carbon-enhanced metal-poor (CEMP) stars has been an interesting problem for the i process model. Current models underproduce strontium in comparison to observations, even though the same model is in agreement with neighboring isotopic abundances. Understanding i-process Sr production requires constraining uncertainties for reaction rates with high impact. Sensitivity studies are performed to identify individual reactions that, if experimentally-constrained, will significantly reduce uncertainties of i-process model predictions.

Denissenkov *et al* performed a sensitivity study to determine the (n, γ) reaction rates that most impacted the i-process abundance prediction for Sakurai's object. Multi-zone simulations were used to model the stellar evolution of a TP-AGB star, followed by post-processing nucleosynthesis calculations where nuclear reaction rates were randomly chosen within uncertainties. In addition, one-zone models were performed to identify single reaction rates that may impact the abundance pattern. The reaction rates of 52 isotopes were varied both randomly and systematically in order to analyze the impact on the predicted abundances of Rb, Sr, Y, and Zr. The Hauser-Feshbach statistical model code `TALYS` was used to calculate reaction rates for 20 different combinations of NLD and γSF, concepts discussed in Sec. 2.4.2 and 2.4.3. It was found that the Sr abundance of Sakurai's object was most affected by two reactions, ^{87}Kr(n,γ)^{88}Kr and ^{88}Kr(n,γ)^{89}Kr. Additionally, the latter reaction strongly affected the Sr/Y ratio.

Another sensitivity study was carried out by Martinet *et al*, which looked into the model (systematic) and parameter (statistical) uncertainties of theoretical (n, γ) reaction rate calculations [4]. Nine specific combinations of NLD and γSF models were used to calculate reaction rates and cross sections in `TALYS` in order to understand the model/systematic uncertainties. The parameter/statistical uncertainties were studied by locally varying four parameters for two sets of NLD + γSF combinations. Isotopic abundances were then determined by a multi-zone stellar evolution model for the early-AGB phase of a low-mass, low-metallicity star. Again, the ^{88}Kr(n,γ)^{89}Kr reaction was identified as having the strongest impact on Sr production.

The study of neutron-capture reactions relevant to the astrophysical i process is an active area of research due to the advancements in experimental capabilities that make it possible to determine (n, γ) reaction rates away from the valley of stability, thereby reducing model uncertainties. The two sensitivity studies mentioned provided motivation for the experimental measurements reported in this thesis. The first experimental constraint of ^{88}Kr(n,γ)^{89}Kr by indirect technique will be presented, and a discussion of its impact on the Sr abundance predicted by the i process will follow.

CHAPTER 4

EXPERIMENTAL SETUP

The in-beam commissioning of SuNTAN was performed at the NSCL, at Michigan State University. The Coupled Cyclotron Facility produced a ^{48}Ca primary beam at 140 MeV/u impinged on a beryllium target. The subsequent cocktail beam of isotopes created through fragmentation of ^{48}Ca was separated with the A1900 fragment separator, which delivered a secondary beam of ^{42}S. The secondary beam was stopped in the gas stopping area, extracted, and delivered to the experiment end station located in the low-energy area of the laboratory [38, 39]. The beam was implanted on the tape in the center of SuN. The implantation point is laterally surrounded by the SuNSPOT β-detector. The NSCL Digital Data Acquisition System (DDAS) was used to digitize and record signals from all detectors [40, 41]. A hardware trigger created from a coincidence between the two halves of SuN and at least one of the SuNSPOT PMTs was used to tune the radioactive beam after an initial stable beam tuning.

The SuNTAN setup was later moved to Argonne National Laboratory where it was used to study isotopes produced by the CARIBU facility [42]. The commissioning of the setup at ANL took place using a ^{142}Cs beam, which was chosen partly due to its high fission yield from the ^{252}Ca source of CARIBU. In addition to ^{142}Cs (half life of 1.68 s), the beam composition included isobaric contamination of its decay product ^{142}Ba (half life of 10.6 minutes), as well as ^{142}Xe (half life of 1.23 s)[43]. The Multi Reflection Time-Of-Flight (MR-TOF) mass separator was used to effectively remove ^{142}Xe from the beam implanted on the tape inside SuN [44]. Due to the large time difference between parent and child β-decay half lives, further beam contamination could be minimized with the tape cycle sequence, a procedure discussed in detail in Section 5.1.

4.1 Detectors and Setup

4.1.1 SuN

The Summing NaI(Tl) detector is a total absorption spectrometer developed at the National Superconducting Cyclotron Laboratory at Michigan State University [6]. It consists of a 16-inch diameter NaI(Tl) crystal cylinder with a 1.8-inch diameter bore hole through its symmetrical axis.

The cylinder is divided into a top half and a bottom half, each of which consists of four optically-isolated segments, shown in Fig. 4.1. Each segment has three photomultiplier tubes (PMTs) attached. The 24 SuN PMTs are biased by iseg high voltage modules housed in a WIENER MPOD crate, which can be controlled by other computers in the network (see Fig. 4.15 for details) or a designated website. The energy spectrum of each segment is sensitive to the individual γ-rays in a cascade, while the total absorption spectrum (TAS), in which all energy deposited in SuN is summed, indicates the initial excitation energy of the nucleus.

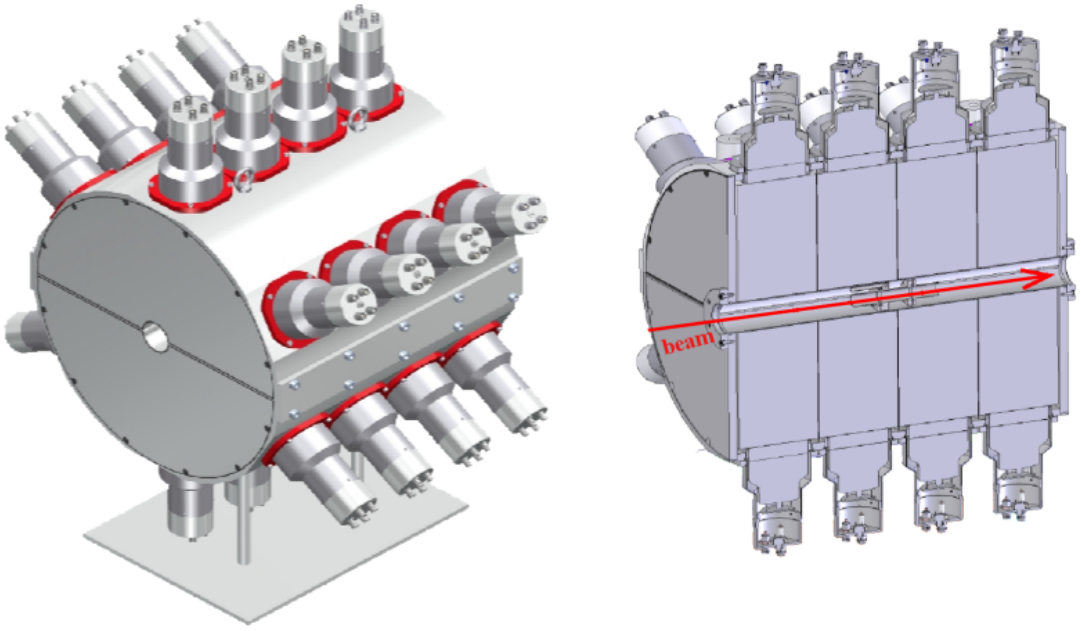

Figure 4.1 Schematics of the SuN detector.

The SuN background spectrum is dominated by natural background in the room and cosmic rays at a rate of over 500 counts/sec per PMT. During a β-decay experiment, the emitted γ-rays need to be isolated from room background. To achieve this, the individual segment and TAS spectra are recorded in coincidence with the emitted β-particle.

β-decay studies using SuN can be divided into three categories depending on the half-life of the parent and child nuclei. (1) If the child is stable, then low energy beam ions are implanted in a small silicon surface barrier detector at the center of SuN. The signal from the β-particles is fed through

the back flange of the beam pipe directly into the data acquisition system [8, 45]. However, this method allows for build-up of radioactive decay products which can create background γ-rays. (2) If the child is unstable, but the parent half life is less than 2-3 seconds, a fast beam is implanted in a double-sided silicon detector (DSSD) [9]. The DSSD detects the implantation and the subsequent β particles emitted, which can be correlated in time, thus providing the ability to separate different isotopes in a decay chain. (3) If the child is unstable with a parent half life greater than 2-3 seconds, a tape transport system is needed to remove child activity, and a new β detector (SuNSPOT) was developed to fit around the implantation point in the tape and within the limited space inside SuN. Development of a tape transport system with associated β detector for β-decay experiments with longer-lived isotopes comprised a large portion of this thesis work.

4.1.2 SuNSPOT

The SuN Scintillating Plastic Optical Transport (SuN SPOT) β detector is a barrel-shaped plastic scintillator detector fabricated at Hope College, shown in Fig. 4.3. It consists of eight 20 cm $\times$ 3 mm $\times$ 9 mm. scintillator bars (BC-408) arranged around the beam axis in an octagonal shape and held in place with Eljen EJ-500 optical cement. Each side has four grooves in which four 1-mm multi-clad wavelength shifting optical fibers (BCF-91A) are embedded and held in place with epoxy. The entire detector is painted with multiple coats of reflective paint until opaque. The optical fibers extend along the length of the detector and down the beam pipe, a total length of roughly 30 cm long. Alternating fibers are fed through one of two flat acrylic plastic discs, optically coupled to two Hamamatsu photomultiplier tubes (PMT) (mod. R1104) downstream from SuN. Each PMT is powered by one of the channels of an iseg NHQ 213M high voltage power supply with a voltage of -1100 V (leakage current of -0.278 μA). The signals from each PMT are fed directly into DDAS. In the original design, each side held only three optical fibers instead of four. In this configuration, each PMT would receive light from either 1 or 2 fibers from each optically isolated side. The result was a loss of counts in the low energy regions of the energy spectrum.

When a β-particle is emitted from the implantation point at the center of SuN, it deposits energy in the surrounding scintillator detector. The light produced in the scintillator travels to

the PMTs located downstream from SuN. The energy spectrum contains contributions from dark noise in the PMT. To reduce the background contribution to the energy spectrum, a coincidence condition between the two PMTs can be imposed in software, shown in Fig. 4.4. To tune a low-rate radioactive beam into SuN, an external hardware coincidence signal between the two PMTs can be used as a tuning signal.

The high efficiency of SuN results in significant background detection. For lower beam rates, features of the energy spectrum can be lost beneath the background γ rays. Applying a $\beta - \gamma$ coincidence reduces the background contribution and reveals features in the total energy spectrum that were previously hidden, as shown in Fig. 4.5. The solid black line is the SuN energy spectrum without a β-trigger for a ^{42}S beam implanted at the center of SuN. Multiple peaks of the spectrum correspond to the decays of naturally occurring isotopes, such as ^{40}K and ^{228}Th. When a β-trigger is implemented, the room background peaks disappear and peaks from the β decay of ^{42}S into ^{42}Cl are revealed, shown in the solid blue line. A ^{207}Bi source is used to set the timing parameters required for a coincidence signal between the SuN and SuNSPOT PMTs.

4.1.3 SuNTAN

Away from the region of stability on the nuclear chart, half-lives decrease and the decay products from β-decay are increasingly radioactive. This results in additional background from decay products of the isotope of interest. In addition to the β detector, a tape transport system was also required to successfully reduce the background from radioactive build-up in low-rate beam experiments away from stability.

The SuN Tape system for Active Nuclei (SuNTAN) was designed in collaboration with Louisiana State University (LSU) and Argonne National Laboratory (ANL) and was constructed at the National Superconducting Cyclotron Laboratory (NSCL). The tape system consists of a continuous loop of 0.5-in $\times$ 35 μm mylar tape with metallic coating and can hold a maximum capacity of 150 meters of tape. More than this amount of tape will cause the system to become jammed. Black watch "9-track" tape, such as 3M No. 700 6250 CPI metallic tape, is an excellent tape to use in such a system, as the metallic coating reduces the buildup of electrical charge. This tape was originally

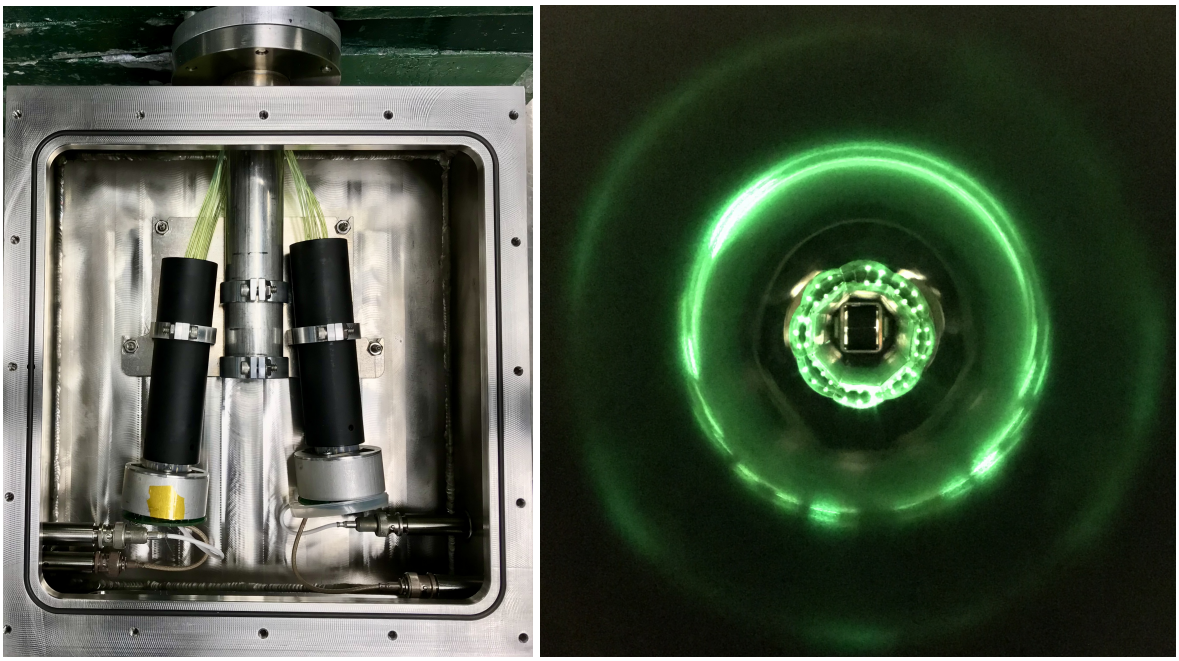

Figure 4.2 (Left) Overhead view of the PMT chamber with SuNSPOT PMTs in place and attached to the ends of the fibers. Each PMT is connected to one BNC feedthrough and one SHV feedthrough, one for the signal out, and one for the high voltage bias.(Right) View from the "beam" of the upstream end of the SuNSPOT detector. The other end is open to light, which illuminates the 24 optical fibers embedded in the exterior of the detector. The implantation area of the tape can be seen inside.

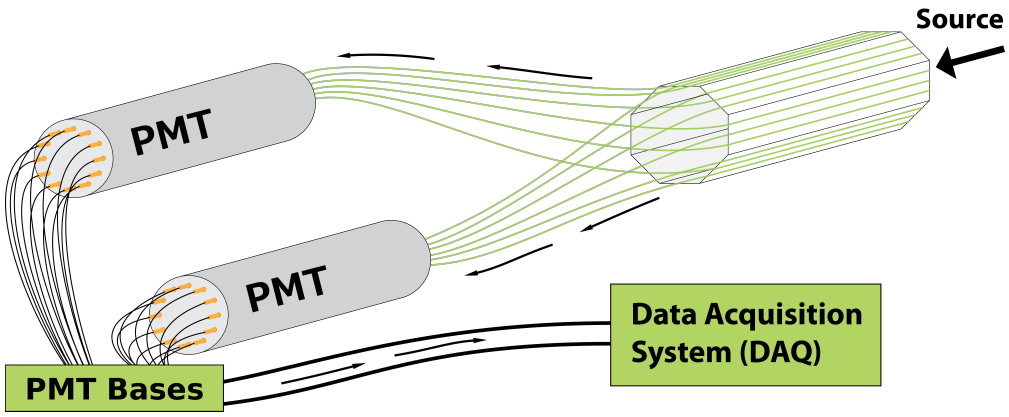

Figure 4.3 Schematic of the SuNSPOT detector. Optical fibers are presented in green.

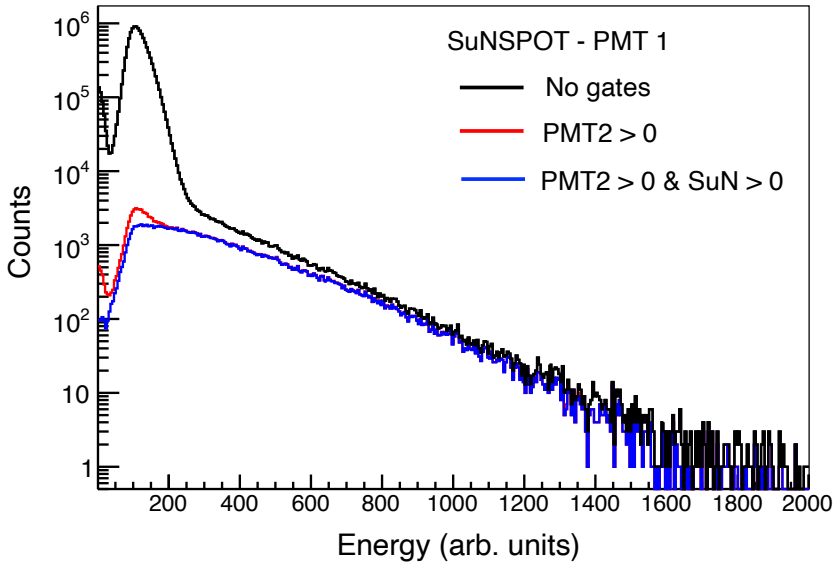

Figure 4.4 The solid black line shows the energy deposited in the scintillator detector, measured from a single SuNSPOT PMT. The red line is the energy requiring a coincidence with the second PMT. The blue line shows the energy deposited with requirement of a triple coincidence between both SuNSPOT PMTs and SuN.

used in IBM computers starting in the 1960's but became obsolete by the early 2000's. There are still supplies of this tape that can be acquired for relatively low cost from many online retailers. Re-purposing black watch tape for nuclear experiments provides additional uses for a product destined for the landfill.

The tape is stored in a thin aluminum box within the main tape box located downstream of SuN. A schematic of the tape system is shown in Fig. 4.7. (A), (B), and (C) refer to the key locations involved in cycling of the tape throughout the system. (A) Tape is extracted from the box by tension from a stepper motor and moves clockwise throughout the system. From the storage box, it moves up the shaft and to the right at (D), where is travels past the SuNSPOT PMTs and into SuN. (B) At the center of SuN and SuNSPOT, the tape is held perpendicular to the beam axis, creating a 0.5-in $\times$ 1-in surface area for the beam to implant. During an experiment, radioactive beam is implanted in the area of tape at the center of SuN. After implantation and subsequent decay, the tape is moved approximately 20 cm, out of detection radius within SuN. (C) The tape is then pushed into the storage box by a roller driven by the stepper motor. The timing of this process, primarily beam collection, decay time window, and movement of tape from center of SuN, is defined as the tape

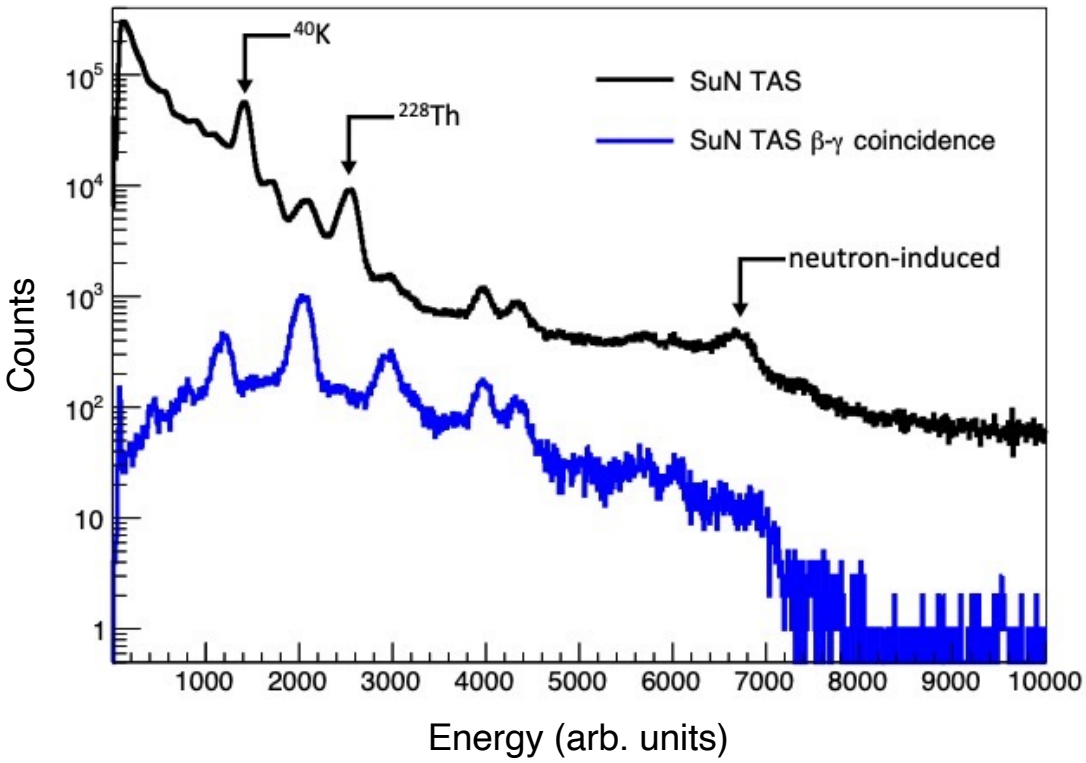

Figure 4.5 SuN TAS energy spectrum for ^{42}S decaying into ^{42}Cl. The black line is the spectrum without a β-trigger. The blue line is the same spectrum, but with a $\beta - \gamma$ coincidence applied in software.

cycle sequence, further detailed in Section 5.1.

The entire tape system is held under vacuum during experiments. SuNTAN can maintain a vacuum of $< 1 \times 10^{-6}$ Torr by an Agilent Navigator V551 turbomolecular pump, mounted on the back side of the main tape box, backed by an Agilent dry scroll roughing pump. All pumps are oil-free, as low-energy beam lines are typically held at higher vacuum than fast beam lines. The SuNTAN vacuum setup at ANL is shown in Fig. 4.8. SuNTAN is connected to the rest of the beam line with a gate valve upstream of SuN. Pressure is maintained where the motor connects to the tape box by an O-ring surrounding the drive shaft. If vacuum loss occurs, this site is the most probable leak point. Indeed, the pressure spikes locally each time the motor is turned. Thus, it is critical to have spare O-rings of the correct size, in case of failure. An additional turbo pump can

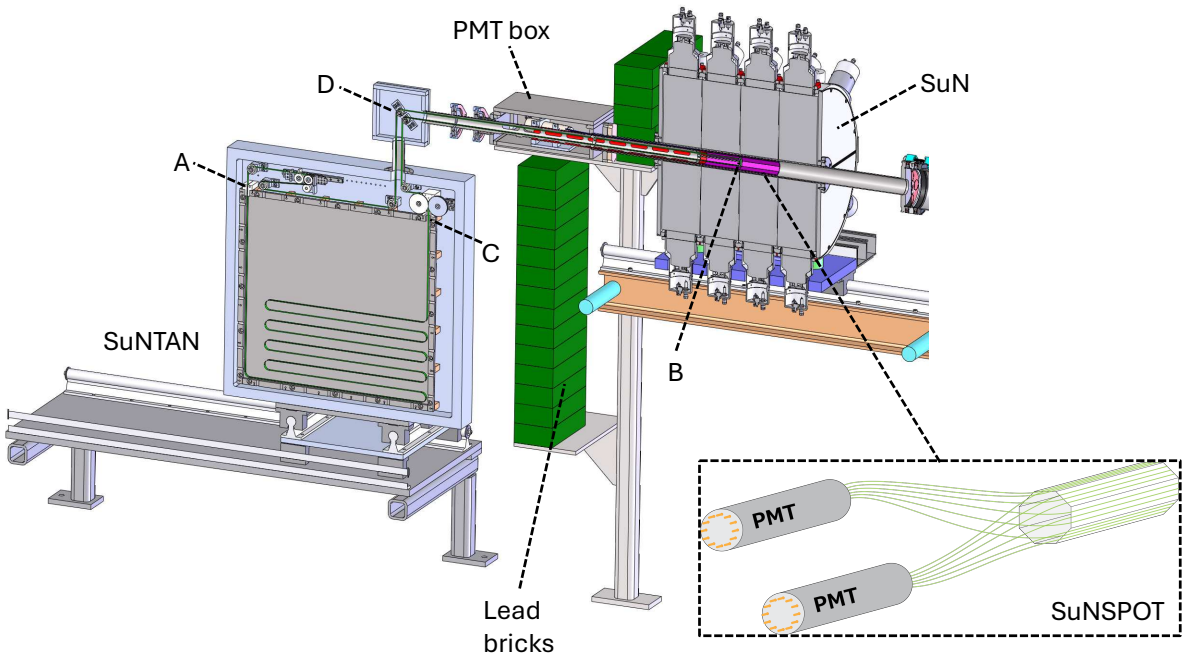

Figure 4.6 Schematic drawing of the SuNTAN setup.

be placed at a cross upstream of SuNTAN to improve pumping efficiency. The black watch tape takes significantly more time to pump down to vacuum upon its first use, due to out-gassing. The system should be held in vacuum as much as possible, so as to reduce pumping time with each subsequent pressurization.

Vacuum System Valves: The backside of SuNTAN has three vacuum valves: Valve A connects the interior volume of SuNTAN to the roughing pump and is opened immediately upon rough pumping down; Valve B is opened prior to turning on the turbo pump, as it needs to be backed by a roughing pump; Valve V is the vent valve for the system. SuNTAN can be vented with air, but preferably, dry nitrogen is used to prevent build up of water in the system, which increases pumping time.

Vacuum Gauges: The Super Bee Pirani gauge has a pressure range from atmospheric pressure down to mTorr. For accurate reading of pressure above 1 Torr, the gauge must be installed horizontally, but due to the limited space on the backside of SuNTAN, it must be installed at an angle. This produces an inaccurate reading of 680 Torr at atmospheric pressure (1 atm = 720 Torr). However, installation angle does not affect pressure readings below 1 Torr, which is the pressure

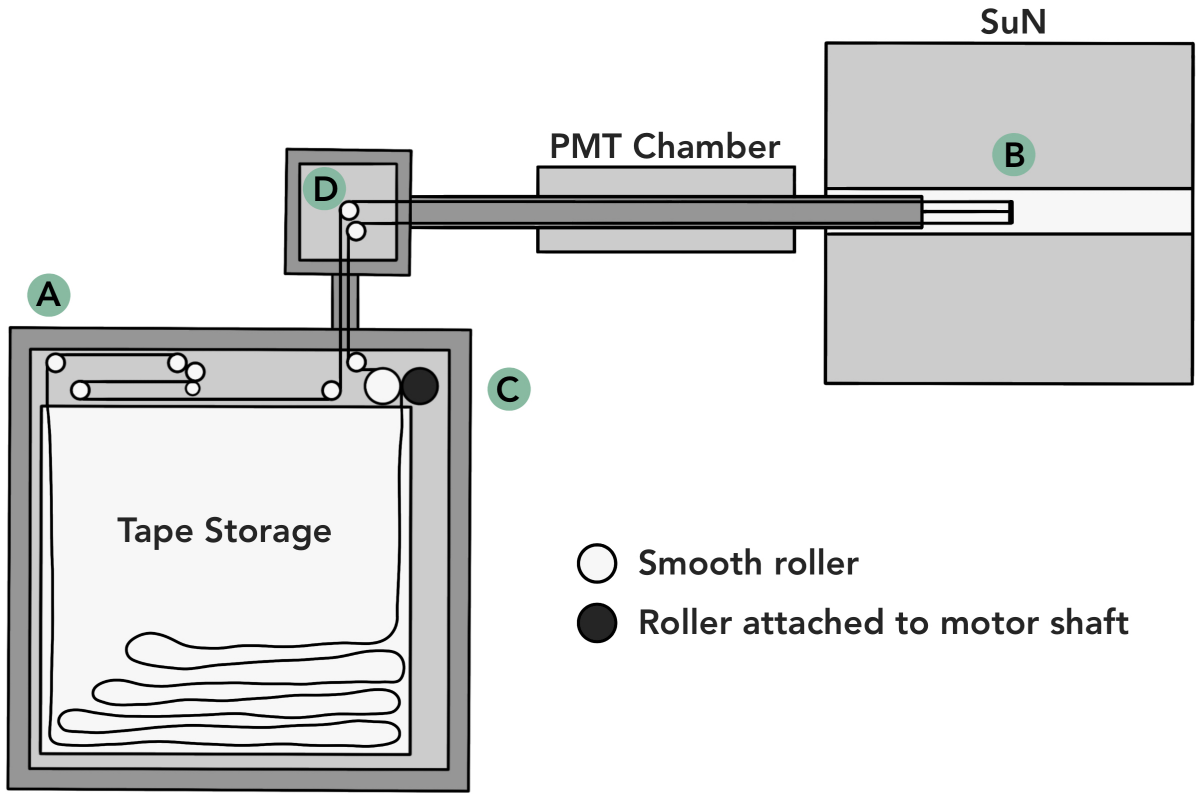

Figure 4.7 Schematic of the SuNTAN tape system. Tape is extracted from the storage box at (A), ions from the beam are implanted in the tape at (B), and the radiated tape is pushed into the storage box at (C), where the motor holds tape tension. A sensor that monitors the tape status (cycling/not cycling) is located at (D).

range important for turbo pump operation. The HORNET cold cathode gauge should not be turned on until the system reaches a pressure below 5 mTorr.

Vacuum Operation: When going from atmospheric pressure to high vacuum, the pumping procedure begins with closing all three valves (A, B, and V) and removing any voltage to the SuNSPOT PMTs. First, the roughing pump is turned on, followed by slowly opening Valve A to begin pumping the SuNTAN system. When the Super Bee Pirani gauge reads < 50 mTorr, Valve A is closed and Valve B is opened. The turbo pump is turned on when the pressure stabilizes below 50 mTorr, and the HORNET cold cathode gauge is turned on at < 5 mTorr. Voltage to the SuNSPOT PMTs can be applied once the HORNET gauge reads < 10^{-6} Torr.

Venting Procedure: Venting the system occurs prior to breaking vacuum and accessing the

inside of SuNTAN for any reason. Prior to venting SuNTAN, the gate valve upstream from SuN must be closed, the PMT voltage must be removed, and the turbo pump must be turned off. Valve B is closed and the turbo pump blades are given time to slow down, as venting while the blades are spinning at too high a frequency will damage the pump. It can take the turbo pump almost an hour to fully stop spinning after operating at the highest frequency setting. While waiting, the cold cathode gauge is turned off and a dry nitrogen line is attached to Valve V. When the turbo spins down, Valve V can be slowly opened to allow nitrogen to fill the system. Once the Super Bee gauge reaches atmospheric pressure, SuNTAN can be opened.

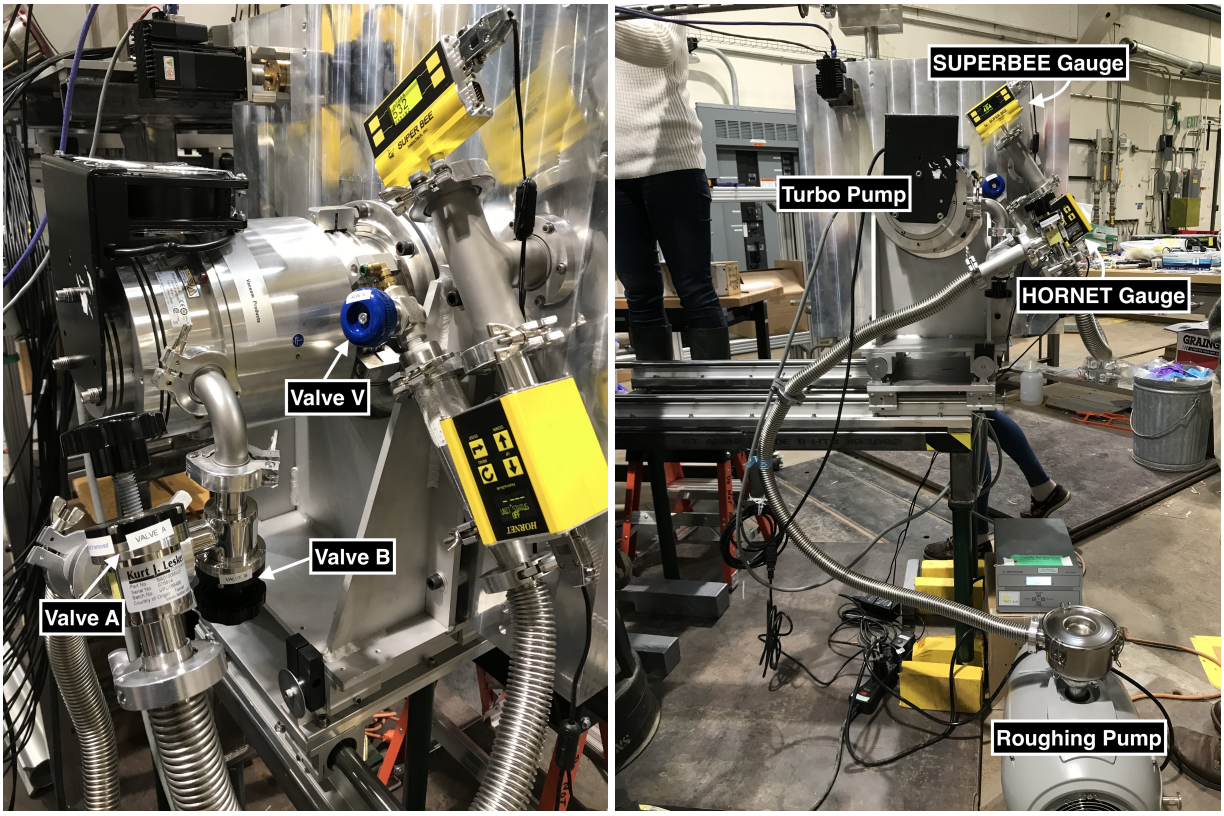

Figure 4.8 The SuNTAN vacuum setup at ANL. (Left) The backside of SuNTAN has three vacuum valves: Valve A connects the interior volume of SuNTAN to the roughing pump; Valve B connects the turbo pump to the roughing pump; Valve V is the vent valve for the entire system. (Right) The two pumps and two vacuum gauges on the backside of SuNTAN. The SUPERBEE is a Pirani gauge with a pressure range from 10^{-3} – 1 Torr, and the HORNET is a cold-cathode gauge (10^{-10} – 10^{-3} Torr) for high vacuum.

The tape system is operated locally on a designated computer. A graphical interface is used to start and stop the motor, set the tape sequence, change the distance of the tape movement, adjust

the motor speed, and monitor the system. This program also outputs a +/-5 V signal to the facility for beam on/off control. The stepper motor that cycles the tape was originally a Parker Accu-Coder stepper motor controlled by a Gemini GT6K-L5 controller. However, this motor/controller combination induced significant electronic noise and time inconsistencies and was replaced after the first experiments at the NSCL. Further improvements to the experimental setup are discussed in Section 4.2.

4.1.4 Electronics and Data Acquisition

The entire electronics setup is installed in a mobile electronics rack that houses the MPOD crate for the SuN PMTs' voltage supply, as well as an XIA crate that contains the digitizer modules and data collection computer (SPDAQ). Each PMT outputs an analog signal that is digitized and recorded by the data acquisition system (DAQ), specifically the FRIB (formerly NSCL) Digital Data Acquisition System (DDAS) [40]. The DAQ data stream is illustrated in Fig. 4.9.

The output signal of each SuN PMT is fed into a pre-amplifier and then into two PIXIE-16 100 MSPS (sampling rate) digitizer modules. The SuNSPOT PMTs output signals are attached directly to the first two channels of a PIXIE-16 250 MSPS digitizer module. The following channels are connected to the tape program signals, which are discussed in more detail in Section 5.1.2. Each channel is configured for the specific signal it is digitizing. For example, the SuN PMT low-energy threshold is set by placing an ^{241}Am source inside SuN. Parameters are adjusted until the 59 keV γ ray is visible in the energy spectrum, but most of the noise is still rejected. In addition to the energy threshold, the 100 MSPS modules' channels are divided into five groups each with a multiplicity coincidence that requires all three PMTs in a segment to fire for the data to be recorded, further reducing (bad events??).

The 250 module applies an 8 by 2 channel grouping coincidence requirement *for beam tuning only*. In this setting, the SuNSPOT PMTs are recorded in coincidence providing a less noisy signal for use by the facility to tune the radioactive beam into SuN. However, the tape signals cannot be recorded as they are never in coincidence, which complicates analysis. Thus, all experimental data needs to be recorded in "singles" with no coincidence requirement between the SuNSPOT PMTs.

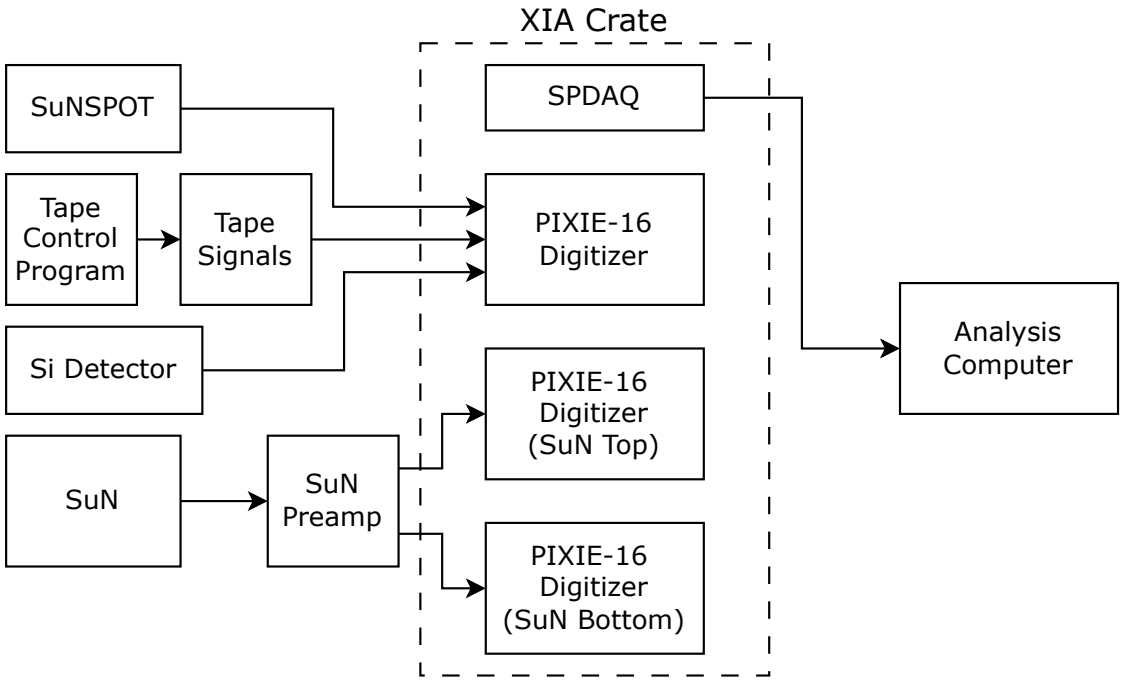

Figure 4.9 Schematic drawing of the DAQ electronics. Further detail of the tape signals wiring is shown in Fig. 4.11.

The energy threshold and time parameters of the SuNSPOT PMTs is also adjusted to reduce noise without cutting out real signals and ensure that SuN and SuNSPOT are detecting decay events at the same time. All settings from the experiment later described are shown in Appendix A as reference for future experiments.

A digitized "event" is defined by the energy output signal and the time of detection within a time window of 300 ns, as well as the crate ID number, module number, and channel number of the individual PMT that fired. The raw experimental data consists of a time-ordered list of event information that is converted into a ROOT software framework data structure for analysis. Further discussion of experimental data analysis is found in Section 6.1.

4.2 Improvements and Changes to Experimental Setup

4.2.1 Reduction of Motor-Induced Noise

While successful, there were multiple problems discovered during the initial in-beam experiments of SuNTAN. Primarily, inconsistencies in the tape cycle timing and noise were observed

from the original motor/controller. The original SuNTAN setup used the Parker Accu-Coder stepper motor/Gemini GT6K-L5 controller combination remotely controlled by a Programmable Logic Controller (PLC). This motor/controller setup is widely used through beam facilities, however, it is primarily used to insert targets, beam stoppers, etc. When enabled for longer periods of time, a significant amount of electronic noise is produced in nearby electronics. The level of noise overwhelmed nearby DAQs while the motor/controller was enabled. In addition to the induced noise, it was also discovered that the Parker motor/Gemini controller has low timing resolution, which resulted in inconsistent tape sequence timings. For these reasons the Parker motor was replaced with a National Instruments combined stepper motor and controller (NI-ISM-7412E) powered with +24 V with 1606-XLE DC Power Supply. The new motor is connected to the network via ethernet cable.

A LabView GUI, shown in Fig. 4.10, was created in collaboration with colleagues at Hope College to set the tape cycle sequence of SuNTAN, manually operate the stepper motor, and control beam on/off signals sent to the facility.

[Explain screenshot figure]

In addition, output signals from the LabView application via National Instruments network box were converted to TTL signals, which could be directly input into the DAQ. These signals, detailed in Section 5.1.2, indicated time signatures for the start of beam on, start of beam off, and start of motor enabling. Table 4.1 list the channel descriptions of the NI USB-6008 I/O box used to convert signals to send to DDAS. Overall, the newer stepper motor significantly improved the accuracy of the timing signals, and the new LabView GUI improved remote operation of SuNTAN.

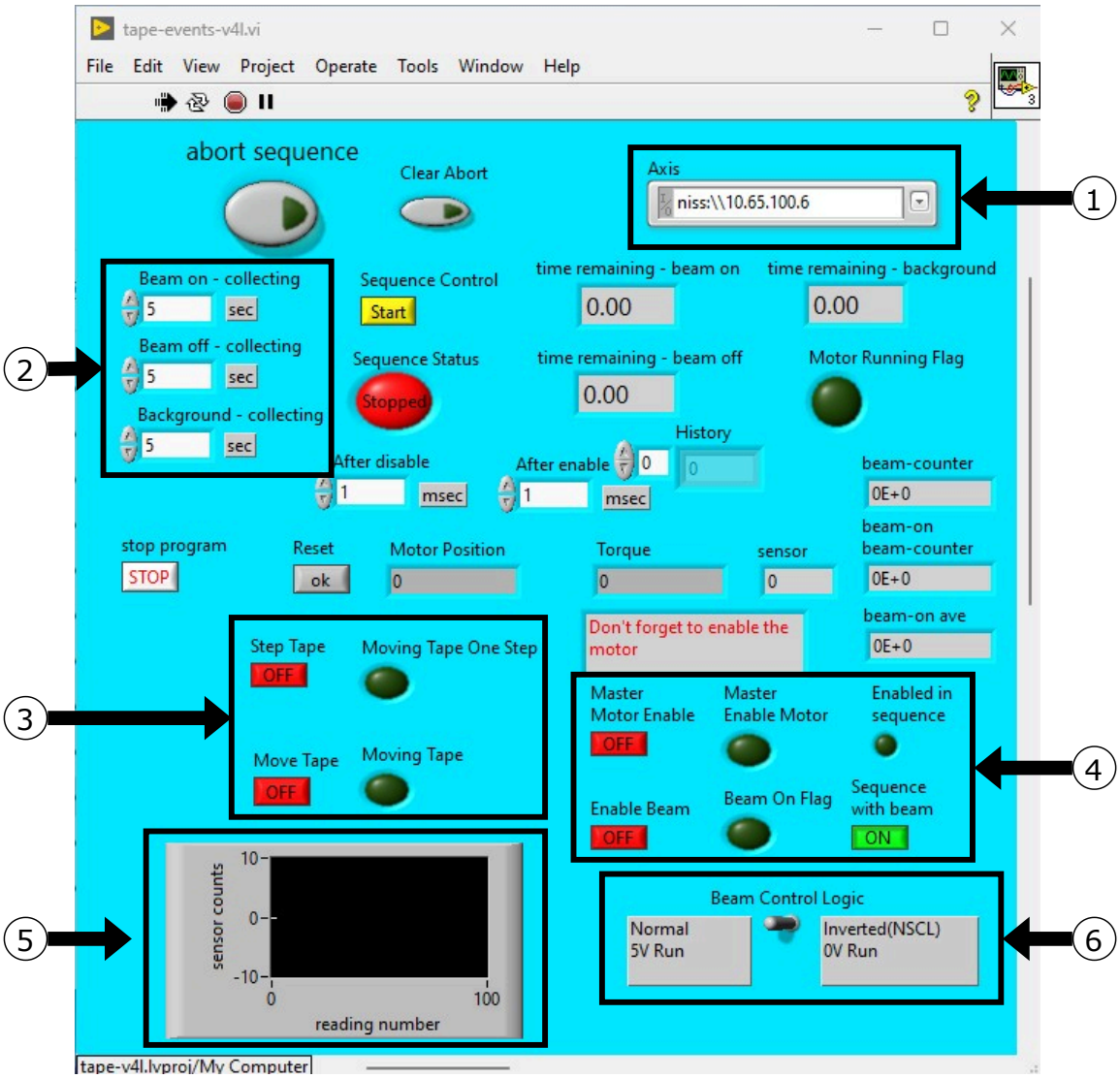

Figure 4.10 Screenshot of the LabView GUI tape control program, courtesy of Paul DeYoung, Hope College, MI.

Channel	Description	Signal Name
17	P0.0	Beam On (to ANL)
18	P0.1	
19	P0.2	Motor Enab (DAQ)
20	P0.3	
21	P0.4	Beam On (DAQ)
22	P0.5	
23	P0.6	Beam Off (DAQ)
24	P0.7	
25	P1.0	
26	P1.1	
27	P1.2	
28	P1.3	
29	PF10	Sensor Input
30	+ 2.5 V	
31	+ 5 V	
32	Ground	

Table 4.1 Wiring of the NI Digital I/O box.

4.2.2 Tape Status Monitoring

An additional upgrade to the tape system, shown in Fig. 4.12, is a sensor that monitors the status of the tape in real-time. Since the system is light-tight, there is no way to determine if there is an issue with the integrity of the tape without breaking vacuum (e.g. the tape is jammed, broken, or has fallen off the rollers - all events that occurred in the early operation of SuNTAN) . This adds significantly more time to troubleshoot potential problems, as the entire system requires turning off the pump and re-pressurizing, which can take hours. A DC Metallic-Object Proximity Switch was installed to monitor the integrity of the tape. It is powered with a +24 VDC from a SOLA SDP2-24-100T Power Supply. A three-pronged stainless steel disc is attached beneath the top roller inside the 90°-bend box, located at (D)is in Fig. 4.7. The proximity sensor sends a signal if one of the prongs is in sensing range (< 1.4 mm), shown in Fig. 4.13. The disc rotates each time the tape is moved, which sends a fluctuating signal for the time that the motor is turning the tape. The sensor sends no signal if the motor turns but the roller is stationary, which means that the tape has been compromised in some way. This signal is shown on the LabView GUI and can be used to monitor the current tape status without breaking vacuum.

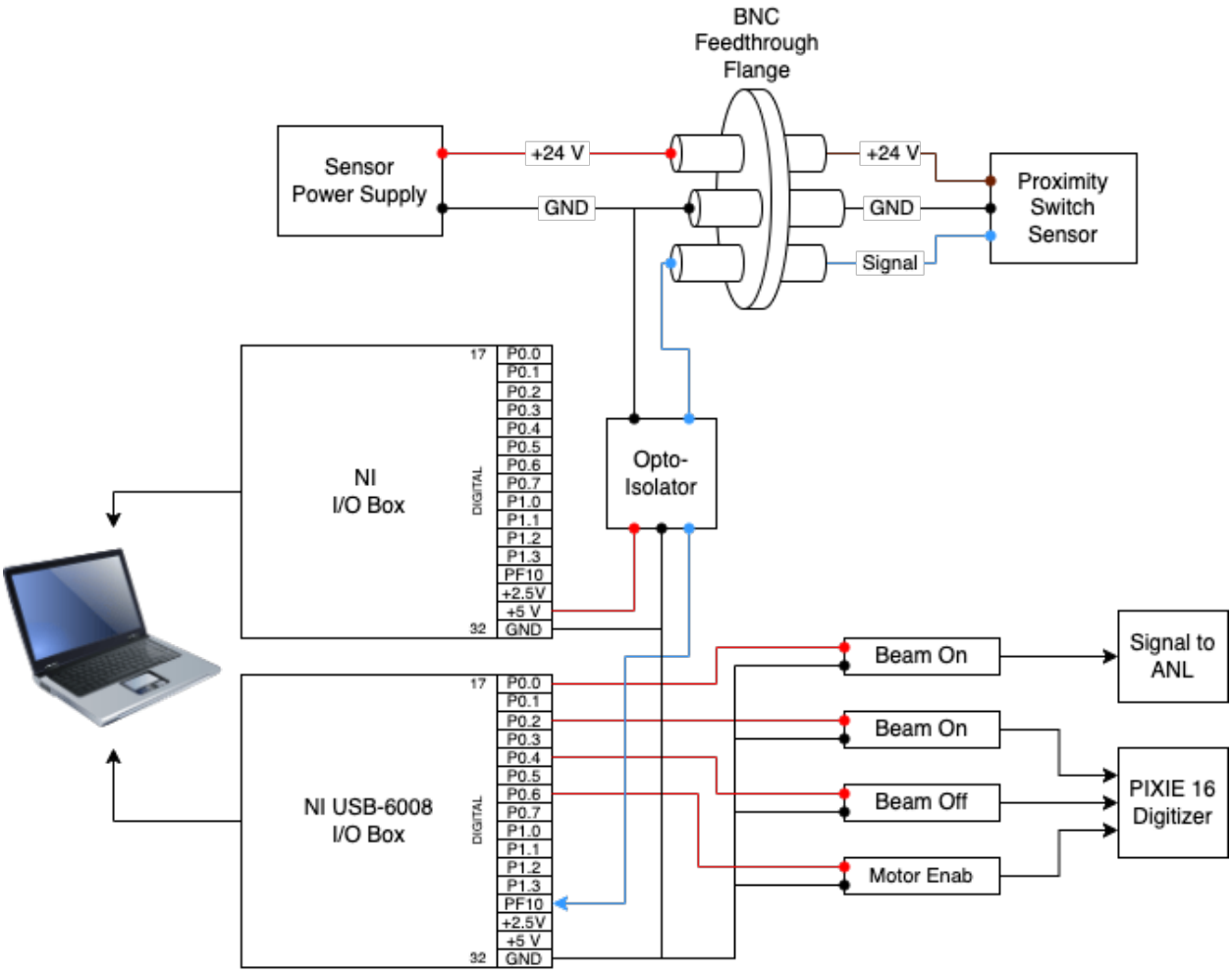

Figure 4.11 Schematic drawing of the wiring for the tape signal electronics.

4.2.3 Silicon Detector for Beam Tuning

While more intense radioactive beams can be tuned using the β-coincidence between the two SuNSPOT PMTs following implant of the beam, this method is not sensitive enough for low intensity radioactive beams, for which a silicon detector is needed. Therefore, we designed a plastic mount for a Si surface barrier detector that attaches at the end of the tape arm, shown in Fig. 4.14. The detector is connected to the DAQ via the BNC feedthrough used for the SuNSPOT PMT. A collimator mask for tuning was also machined and was designed to sit in front of the detector and attached with tape.

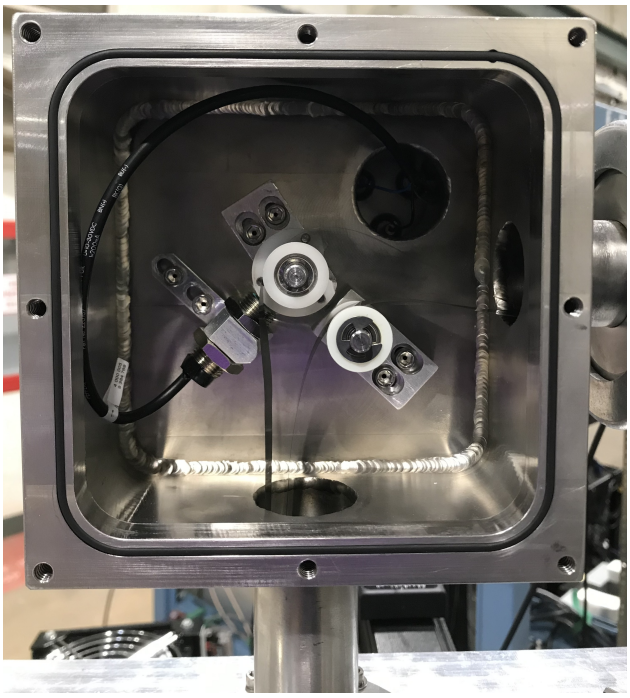

Figure 4.12 The proximity sensor used to provide information about the status of the tape when system is sealed during an experiment.

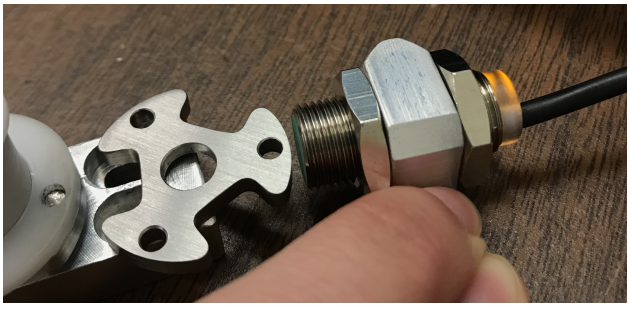

Figure 4.13 Testing of the proximity sensor with the three-pronged roller attachment. The yellow light indicates that the sensor is working.

4.2.4 Standalone DAQ

Further challenges arose when SuNTAN was moved to Argonne National Laboratory. Without the FRIB network, a local network was created between the DAQ computer, primary analysis computer, SuNTAN laptop, SuNTAN motor, and SuN HV supply (MPOD). This was achieved using a network switch located near the setup. A schematic of the network connections mapping is shown in Fig. 4.15. Additionally, moving to Argonne required a standalone DAQ that could operate without the FRIB DAQ framework, including storage of raw data. This was achieved through the creation of a designated desktop computer that replicated the FRIB DAQ system. The DAQ located

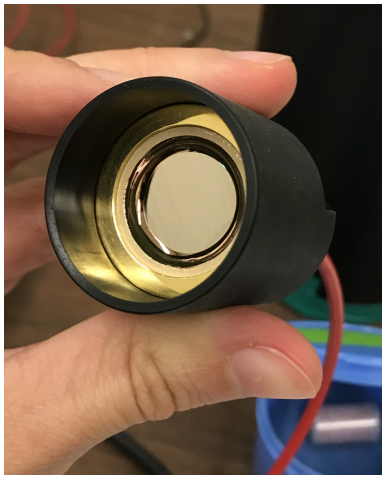

Figure 4.14 Si detector used for tuning low intensity radioactive beam into SuN. The black case was custom-made to attach to the end of the tape arm at the center of SuN.

on the electronics crate (spdaq52) was responsible for taking data and writing it to the raw files directory. The desktop computer (spdaq54) was used for dumping and converting raw data files, as well as on-line analysis. The spda52 computer was connected to the new spdaq54 computer via the network switch and an external hard drive was used to store and backup data and analysis codes. ANL provided a ZBOX mini computer that allowed for remote connection to the SuNTAN setup from facility computers in the experimental user area. This allowed for remote operation of all experimental electronics and easy online data monitoring.

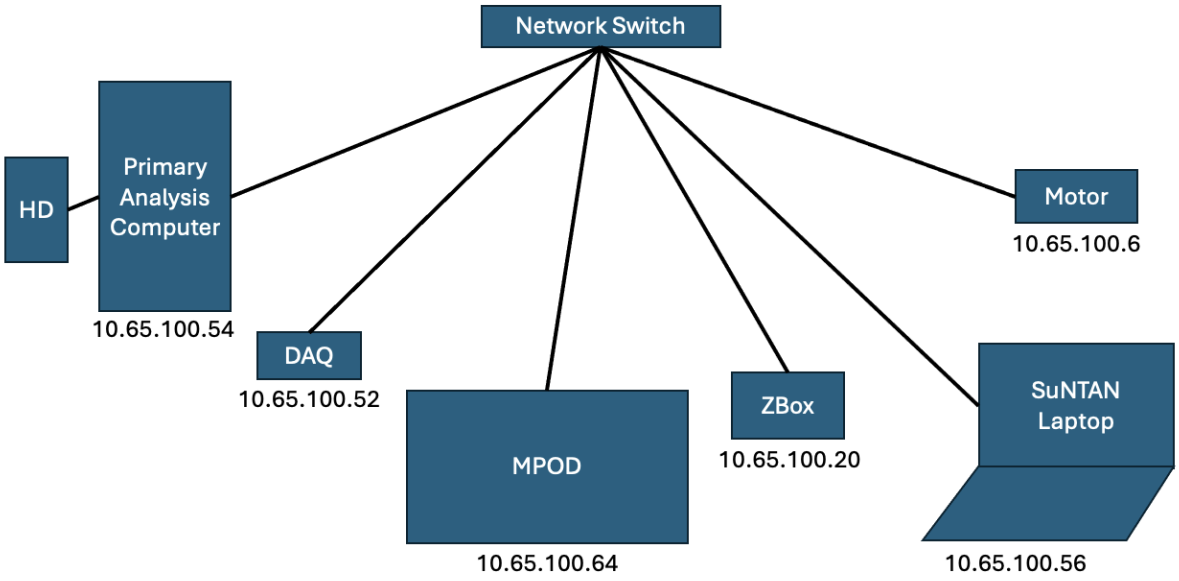

Figure 4.15 Local network map for SuNTAN electronics at ANL. Any one device can connect to any other device within the network. Device IP address are labeled under each device symbol.

CHAPTER 5

EXPERIMENTAL TECHNIQUES

This chapter will discuss the techniques used to analyze the experimental data from SuNTAN β-decay experiments. First, the tape sequence logic will be explained in Section 5.1.1. Then, the β Oslo Method will be discussed in Section 5.2, followed by a discussion of the Shape Method in Section 5.3.

5.1 Tape Cycles Analysis Techniques

Several techniques were developed alongside the first SuNTAN experiments and analysis, as this was the first time SuN was used with a tape cycling system.

5.1.1 Tape Sequence

A tape cycle, or tape sequence, is defined by three quantities: (1) beam on, which is the amount of time during which radioactive beam is implanted at the center of SuN and (2) beam off, the amount of time after a beam stop is inserted upstream of the detectors, and the implantation point on the tape remains in SuN to measure γ rays from the decay. In shorthand, a tape sequence is given as (beam on time (s), beam off time (s)), as multiple sequences are used during a single experiment. The primary purpose of the tape system is to separate the parent decay from its subsequent decay products. To do so, the tape sequence must be optimized for the parent decay, allowing it to reach decay rate saturation during beam on time, but not so long that the decay products begin to increase to a decay rate that would compete with the parent decay. In some cases, the parent decay can be isolated by an appropriate tape sequence alone, without further subtraction of the daughter contribution through offline analysis. However, many isotopes have decay products with half-lives too short for any tape sequence to successfully capture the parent decay without any contamination. In these cases, the daughter decay needs to be characterized for a clean subtraction from the parent decay spectra. This is achieved by choosing an appropriate tape sequence that optimizes the daughter decay.

The tape sequence beam-on and beam-off values are determined through the calculation of grow-in and decay curves of the parent and child isotopes. A python code was developed to calculate

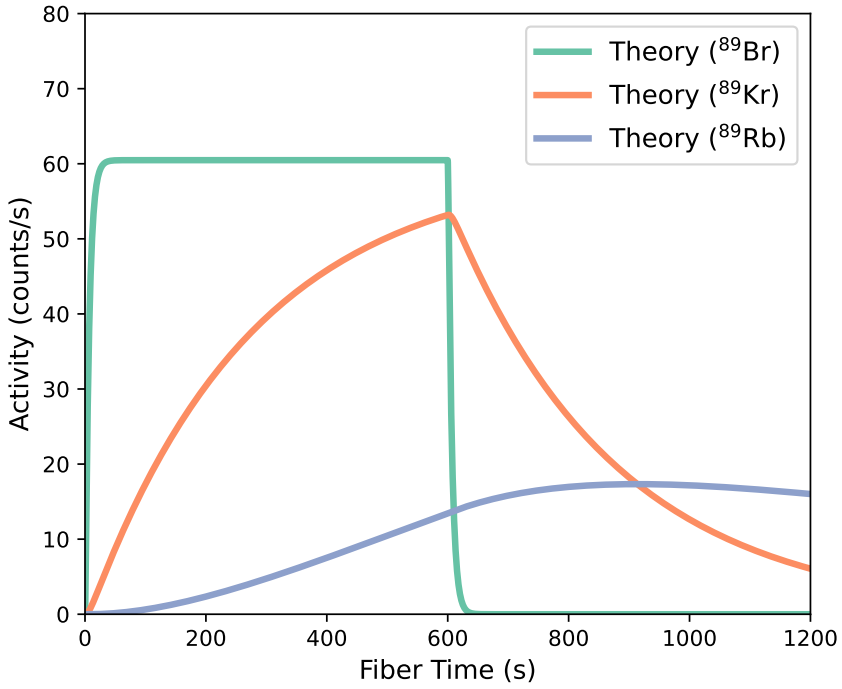

Figure 5.1 Output from the Bateman calculation code for 600 s of grow-in and 600 s of decay for a ^{89}Br beam. The green, orange, and blue line represent the activity of the parent isotope, daughter ^{89}Kr, and granddaughter ^{89}Rb.

these functions through numerical integration of the Bateman equation, derived in Section **??**. The code requires the following input parameters: beam rate, beam-on (grow-in) time, beam-off (decay) time, and beam contamination percentage, if other isotopes are present. Calculations are made prior to a SuNTAN experiment, in order to plan the tape sequences in advance, but need to be re-calculated once the beam rate is known. Then, the number of counts as a function of time from a short experimental run can be exported as text file of x and y values. The experimental rate can be read in by the code and can be plotted on top of the calculated decay rates for the same tape sequence; the beam rate can be adjusted accordingly. As facilities improve, more isotopes are available further from the valley of stability. Therefore, the ability to include additional isotopes on the decay chain was included. An example of a three-step decay chain (^{89}Br $\rightarrow$ ^{89}Kr $\rightarrow$ ^{89}Rb) is shown in Fig 5.1.

During the SuNTAN commissioning experiment, two tape sequences were used. The beam

isotope ^{42}S has a half life of 1030 ms, and reaches saturation within a few seconds. The child nucleus, ^{42}Cl, with a half life of 6.8 s, takes about 20-25 s to reach saturation. Thus, the two tape sequences that were chosen to optimize decay of the parent or child isotope were (2 s, 2 s) and (25 s, 25 s), respectively. Figure 5.2 shows the output plots from the code for the two settings. The light red and blue noisy lines are experimental data for ^{42}S and ^{42}Cl, respectively. The overlaid solid lines are the calculated rates using the Bateman equation code, with half-lives fit to literature values. The calculated rates also include a small percentage (7% and 15%, respectively) of parent isotope decay counts in the child rate because the γ gates used to create the histograms are not 100% clean.

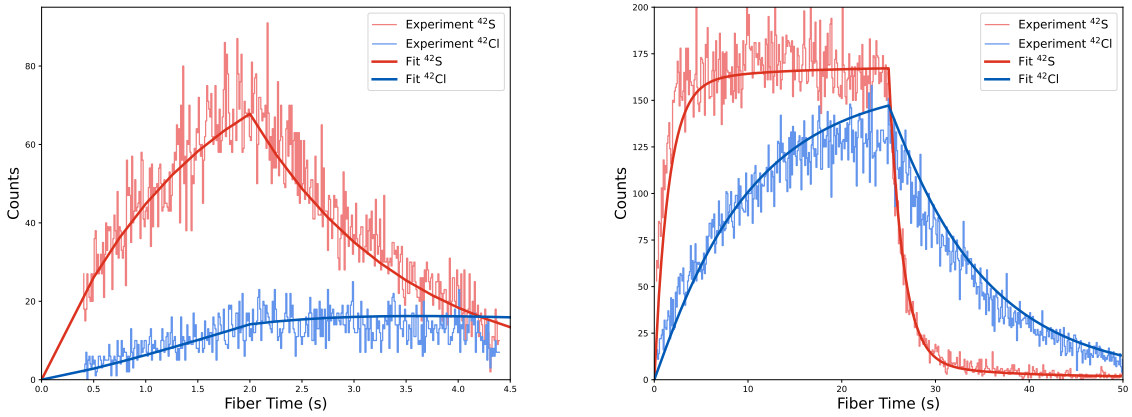

Figure 5.2 Grow-in and decay rates for the (2 s, 2 s) (top) and the (25, 25) (bottom) tape cycle settings. The light red and blue lines are experimental data for ^{42}S and ^{42}Cl, respectively. The overlaid solid lines are the calculated rates using the Bateman equations, with half-lives fit to literature values.

5.1.2 DAQ Parameters

Constructing a Time Marker

SuN low-energy β-decay experiments can operate with very small beam rates, as low as 1 particle per second [8, 9]. During analysis, the number of decay events in a detecter can be plotted as a function of energy or time. For a cycling implantation point, the spectrum of detector time may show few counts if the beam rate is low. Therefore, analysis of SuNTAN data is aided by having a timing marker that can be used to mark the starting point of each tape cycle in order to stack the

histograms of each low-rate run.

For early experiments with SuNTAN, the only consistent time signature of the tape cycle was the noise created when the Parker motor was enabled to cycle the tape. When plotting the entry number as a function of time in the SuN detector, it was observed that the number of entries written to the DAQ greatly increased over the time that the motor was enabled and reduced back to the previous rate when the motor was disabled, as shown in Fig. 5.3. By calculating the slope of this line at various data entries, we were able to differentiate in the data when the motor was enabled or disabled. This gave us a unique time signature that could be used to mark the start/end of a tape cycle.

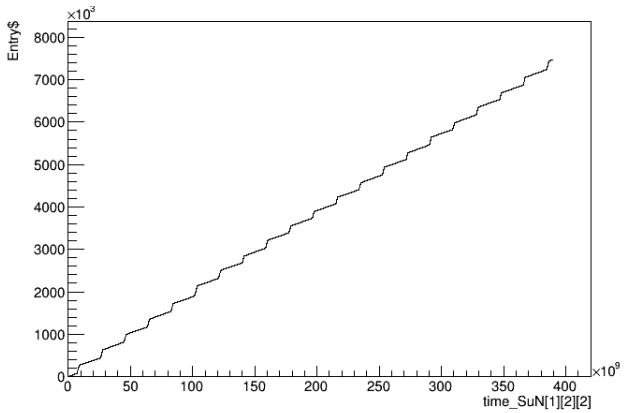

Figure 5.3 The rate of data written to the DAQ has a stair-like shape, where each increase in the slope is due to a change in the motor status (enabled/disabled). The y-axis is the entry number of the root file and the time of a single SuN PMT is the x-axis.

Every 100 entries, a slope is be calculated and, if the slope is above a user-defined threshold, that time is marked as "motor enabled". Once this condition is met, the slope continues to be calculated, and marks another time as "motor disabled" when the slope falls below the threshold. The slope is given by

$$\delta_{slope} = \frac{N_i - N_{i-1}}{t_i - t_{i-1}} \tag{5.1}$$

where N_i and N_{i-1} are the entry numbers for the current entry i and the previously stored entry $(i-1)$, respectively, and t is the SuNSPOT PMT time with the corresponding index i and $(i-1)$. The number of entries between those used for slope calculation and the threshold value had to be

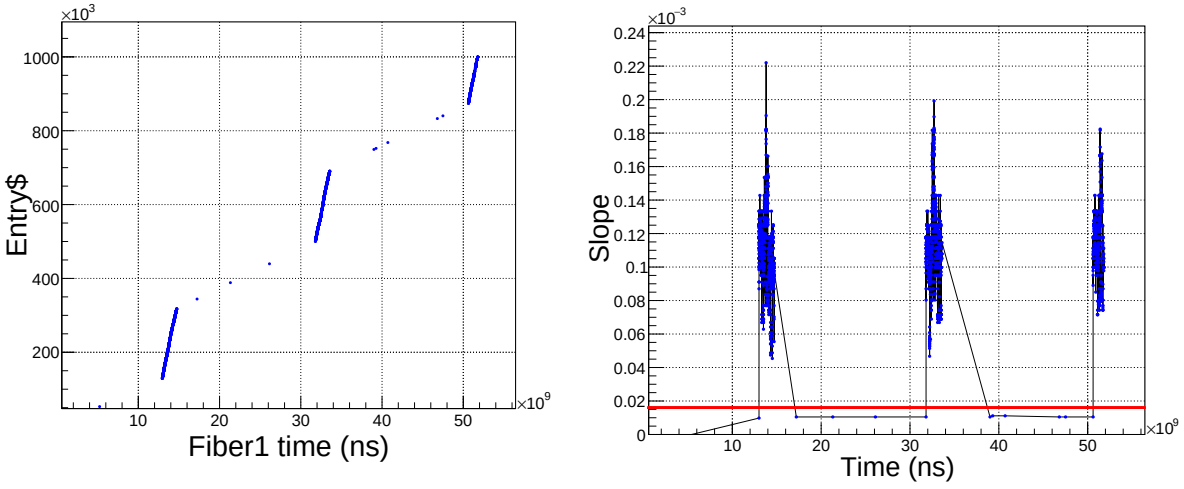

(a) (b)

Figure 5.4 The left plot (a) shows the rate of entries written per unit time, where each data point is the entry number and time a slope was calculated. On the right, (b) the slope is given for each time that it is calculated. The blue data points are the slope value at the time it was calculated and the red line is the threshold, which is 1.6×10^{-5}. See text for further discussion.

tuned such that the noise was caught early on, but the fluctuation in the slope value did not falsely trigger the threshold. This is depicted in Figure 5.4, where the first 1×10^6 event entries are plotted. The number of events written greatly increases during the time the motor is enabled, as seen in the steep sloped line that contains thousands of counts in the left figure (a). In contrast, the roughly 14 seconds between tape cycles contain only three or four data points. Figure 5.4 (b) shows the large fluctuation in slope values within the motor-enabled time window. These two points emphasize the need to precisely choose the distance between entries used in the slope calculation, as well as the threshold value, to accurately represent the tape cycle.

Modulo Operator

As previously discussed, after the first SuNTAN experiments, the Parker motor was replaced with an NI motor that was significantly less noisy and had good time resolution. The consistent tape cycle eliminated the need for the determination of a unique time signature to flag the start of a new tape cycle. One simply has to plot the time parameter acted upon with the modulo operator available in ROOT, which returns a remainder after dividing by the tape sequence, which we call

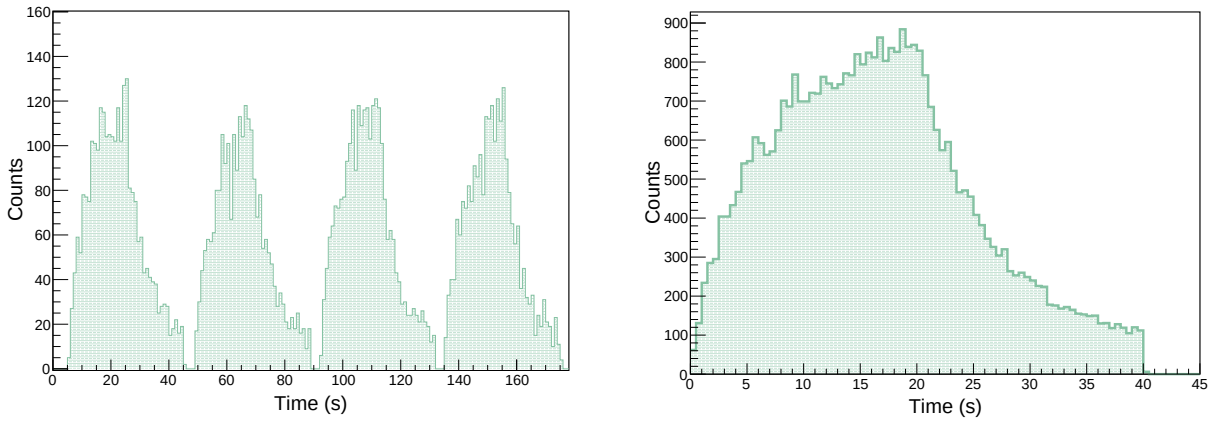

(a) (b)

Figure 5.5 (a) Counts in a PMT for a (20 s, 20 s) tape sequence. (b) Folded time spectrum after applying the modulo operator.

the folded time. The tape sequence is given by,

$$T_{cycle} = T_{BeamOn} - T_{BeamOff} + T_{MotorEnab} \tag{5.2}$$

where $T_{MotorEnab}$ is the time it takes for the motor to enable, cycle the tape, and disable, all of which takes exactly 3 seconds.

Figure 5.5 shows the unfolded and folded time spectra of the SuNSPOT detector. The folded time can then be shifted, so the start of the tape cycle starts at zero. To do so, the amount of time to be shifted, T_{shift}, is subtracted from the time parameter, t_{PMT} prior to applying the modulo operator, expressed as $(t_{PMT} - T_{shift})\%T_{cycle}$.

Tape Signals in DDAS

While the previous method is much simpler than the first method described in this subsection, time markers directly written to the DAQ would further streamline data processing. The tape sequence program was revised to include output signals for "Beam On", "Beam Off", and "Motor Enabled" that connect directly to the DAQ, shown in Figs. 4.9 and 4.11. The DDAS parameters are given in Fig. A.1 of Appendix A. The data processing code utilizes these signals in the following manner:

1) The "Motor Enabled" channel is used to reject all detector events during the period of the tape cycling, as most events are noise.

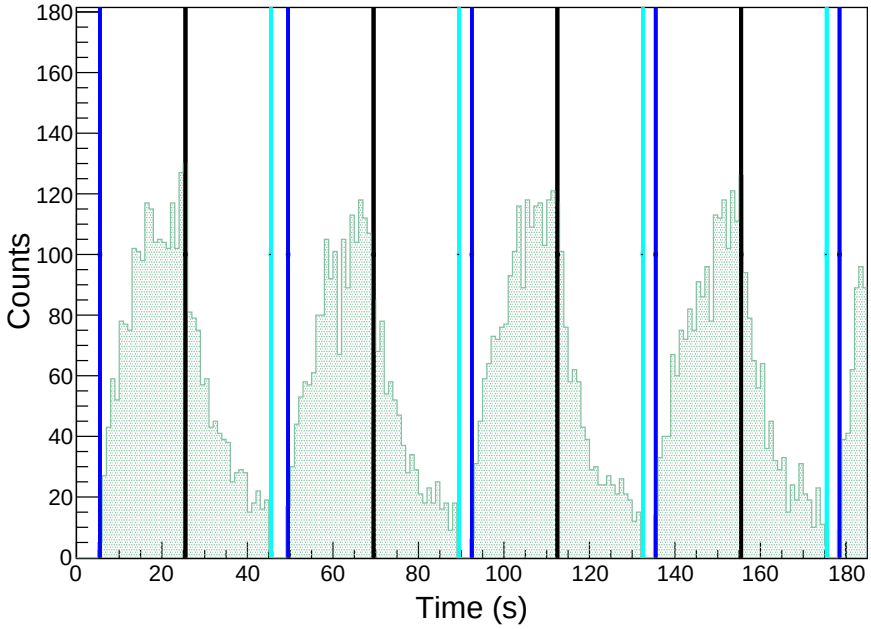

Figure 5.6 A time spectrum overlaid with the DDAS tape signals for beam on (dark blue), beam off (black), and motor enabled (cyan).

2) The "Beam On" channel is used to create a folded time parameter for the SuNSPOT PMTs without creating a histogram first. This additional parameter allows for easier application of coincidence gates, which is discussed in the following subsection.

3) The "Beam Off" channel can be used to mark the beginning of a decay, which may be less obvious in a low beam rate experiment.

Fig. 5.6 shows the three signals superimposed on a PMT time spectrum. Each signal is clearly defined and parallels the grow-in and perfectly matches the shape of the data, including the zero counts between the "Motor Enabled" and "Beam On" counts.

5.1.3 Coincidence Spectra

Coincidence requirements, also called energy or time gates, are used to investigate the data from multiple angles. The SuNTAN commissioning used a ^{42}S beam that decayed into ^{42}Cl. The parent isotope ^{42}S decays predominantly into energy levels at 1267 keV, 2123 keV, and 3029 keV, while ^{42}Cl decays into 4045 keV and 4416 keV [46]. These levels can be seen in the TAS spectrum in Fig. 5.7a for different regions of time in a (25 s, 25 s) tape cycle. The spectrum from the first 5 seconds

of the beam on time period clearly show the three energy peaks of ^{42}S, while the last 20 seconds of the decay time period have prominent peaks at the energies populated by the decay of ^{42}Cl. For the tape sequence optimized for the parent decay, the two peaks from the child decay energies are highly suppressed compared to the sequence that allows for full saturation and subsequent decay of both parent and child nuclei.

Another useful diagnostic is to plot the energy deposited in SuN as a function of time. For this purpose, multiple runs from the ANL Commissioning are overlaid. The β decay of ^{142}Cs most strongly populates the energy level at 1326 keV of ^{142}Ba, which can be seen in the bright yellow line in Fig. 5.8. It is clearly evident that the parent decay drops to zero very shortly after the beam is turned off at 600 s. The β decay of ^{142}Ba into ^{142}La feeds levels at 1078, 1204, and 1457 keV, as well has some lower-lying levels, which appear as light blue lines that continue well past the 600 s mark. This detail allows for background subtraction of the child decay products from the isotope of interest. Hence, SuNTAN experiments need to run with multiple tape sequences in order to characterize background decays as best as possible.

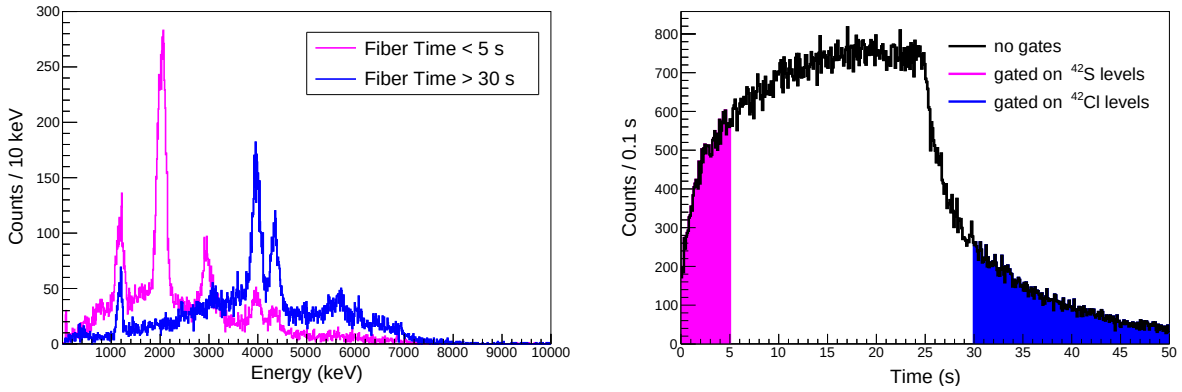

(a) (b)

Figure 5.7 The top plot shows two TAS spectra with gates on fiber detector time. The magenta line shows events from the first five seconds (see shaded region of the same color below) of 25 s beam on, 25s beam off tape cycle. The blue line corresponds with events in the fiber detector from 30 to 50 seconds (blue shaded region in plot below). The bottom plot is fiber detector time in coincidence with SuN with shaded regions that correspond with the TAS plot above.

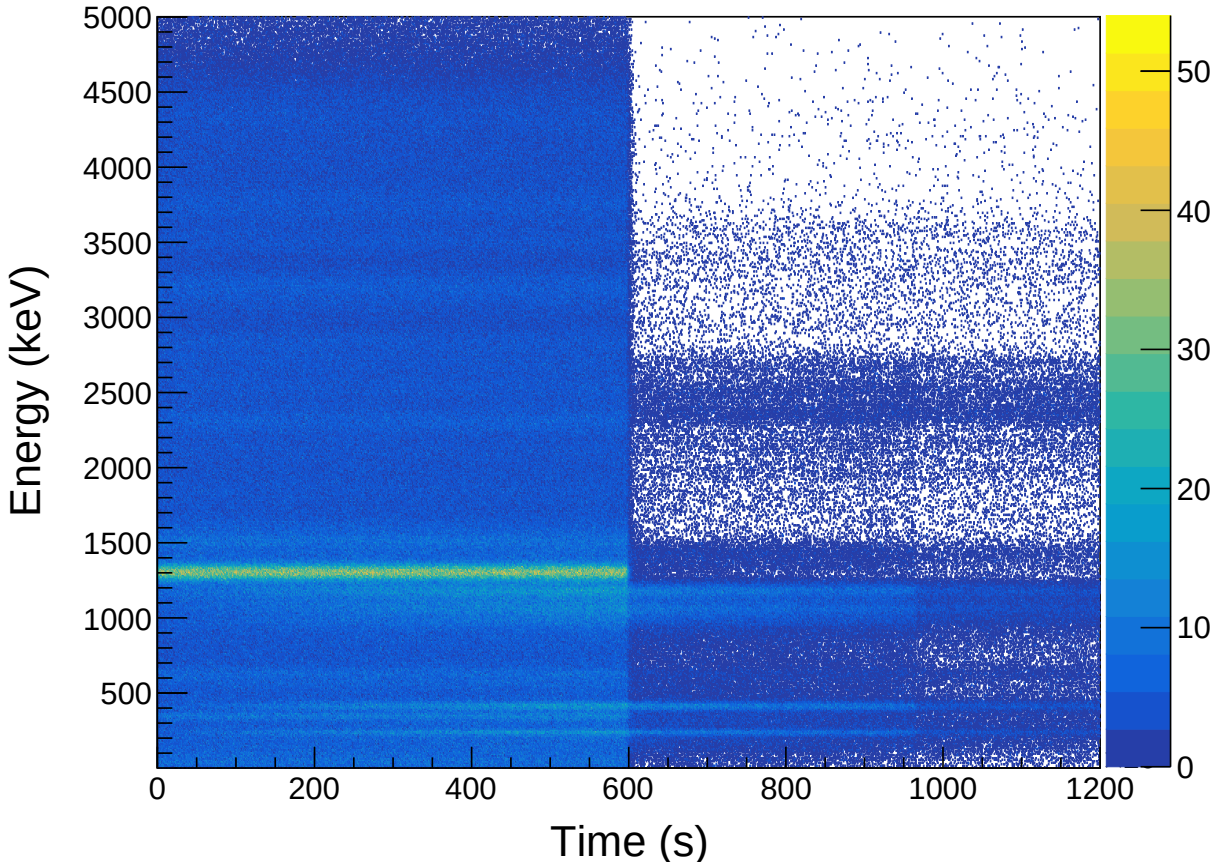

Figure 5.8 Time is on the x-axis, in which beam is implanted at the center of SuN for 600 s, then the beam is cut off upstream and decays only are measured for 600 s. The y-axis is energy deposited in the entire detector. Each horizontal line of lighter coloring corresponds to an energy level in the isotopes of the decay chain, starting with ^{142}Cs. ^{142}Cs levels begin to grow in counts as time increases, but disappear almost immediately after the beam is stopped at 600 s. Energy levels from the decay of ^{142}Ba grow in slower over the 600 s beam on period and continue to decay long after the beam stops implanting.

5.2 β-Oslo Method

The Oslo method [] has existed for decades and continues to be improved and expanded upon. The goal of this method is to measure the nuclear level density (NLD) and γ-ray strength function (γSF) from experimental data. Oslo measurements have been used to make significant contributions to the field of nuclear physics. Nuclear structure contributions include study of the M1 scissors resonance [], the E1 pygmy resonance [], and the discovery of the Low-Energy Enhancement ("LEE" or "upbend") of the γSF []. These measurements have constrained (n,γ) reaction rates relevant to astrophysical models [47]. The Oslo method has been expanded to include data from β decay, called the β-Oslo method [8, 9], as well as from inverse reactions [48]. The main assumptions of the Oslo method are as follows,

1) The γ decay of excited nuclear states in the statistical region is independent of the mode of formation, e.g. via particle reaction, β decay, scattering, etc.

2) The γ decay from the statistical excitation energy E_x region is primarily dipole radiation.

3) The γSF is independent of initial or final excitation energies and is dependent only on γ-ray energy E_γ.

4) The NLD consists of equal numbers of positive and negative parity states.

That being said, the Oslo method will be outlined in the following subsections for the purpose of familiarizing the reader with the basic steps involved, as well as discussing any limitations to the method.

5.2.1 Coincidence Matrix

The starting point of the Oslo Method is to obtain a $E_x - E_\gamma$ matrix ("raw matrix"), which requires experimental measurements of the excitation energy E_x and the γ-ray transition energy E_γ. An example of this matrix is shown in Fig. 5.9. The experiments traditionally utilized are transfer reactions, such as (^{3}He, $\alpha\gamma$) and (p,tγ), and inelastic scattering reactions, including (^{3}He,^{3} He$'\gamma$) and (p, p$'\gamma$) on enriched targets surrounded by detectors to measure the ejected charged particles

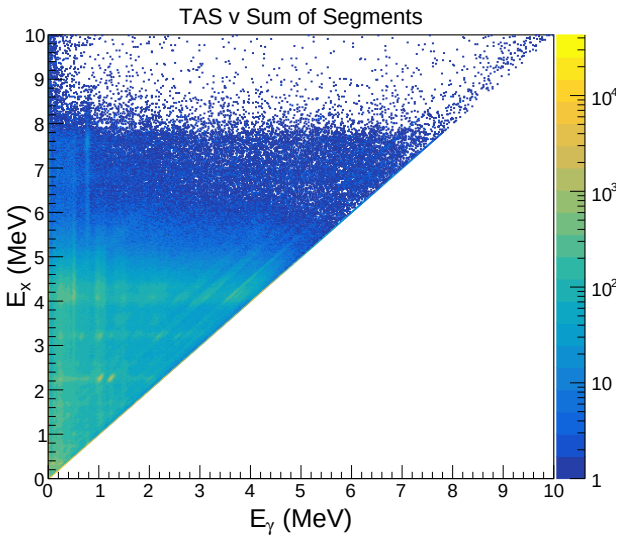

Figure 5.9 Raw experimental β-decay matrix of the excitation energy E_x vs. γ-ray energy E_γ.

in coincidence with emitted γ rays [47]. More recently, the Oslo method has been performed using inverse kinematics for the d(^{86}Kr, pγ)^{87}Kr reaction to measure the NLD and γSF of ^{87}Kr. The ^{87}Kr results will be compared to this work in Section 6.2.3.

In addition to reactions, excited states of the compound nucleus can be populated by β decay. An advantage to using β decay rather than reactions, is that isotopes further from the valley of stability are accessible, even for low beam rates. However, this method is limited by the β-decay Q-value and γ-decay selection rules. For that reason, the beam isotope Q-value should be around or above the neutron separation energy S_n of the daughter nucleus.

5.2.2 Unfolding

Once a raw matrix is obtained, it must be corrected for the detector response to γ-ray interactions. This process, called "unfolding", is described in detail in Ref. [49]. It is the deconvolution of the experimental E_γ spectrum into the true unfolded spectrum where detector effects are removed.

Response Function

The detector response function $\mathbf{R}(E, E_\gamma)$ is a matrix that captures the energetic processes given an incident γ ray of energy E_γ. The response function contains all of the ways emitted γ-rays interact with the detector, including the photoelectric affect, Compton scattering, single and double escape, and annihilation, discussed in Section 2.2.3. Each detector array requires a unique response

function that is determined through measurements of monoenergetic γ rays from radioactive sources and in-beam experiments for a range of E_γ. For example, the 662 keV γ ray from ^{137}Cs, as well as the 1173 keV and 1333 keV γ rays of ^{60}Co are γ-lines from common sources used the construct the response function for those energies. Furthermore, peak full width at half maximum (FWHM) and detector efficiency are also measured for the range of E_γ. Since it is not possible to measure the response function at every incident energy, simulations are used for interpolation between measured energies and extrapolation beyond the highest energy measured γ ray. The response matrix for the NaI(Tl) segments of SuN was generated with GEANT4 [ref GEANT] and validated with standard γ sources and known resonances [6].

Difference Approach

Once a response matrix has been constructed, an iterative subtractive procedure is performed, in which a trial spectrum is "folded" by the detector response matrix and compared to the observed spectrum. The difference in the folded spectrum and observed spectrum is then added to the trial function, created the next iteration trial function. This process is repeated until the folded trial function resembles the observed spectrum. The unfolding procedure is performed for each excitation energy bin of the raw experimental matrix. The folded function f can be defined as

$$f = \mathbf{R}u \tag{5.3}$$

where $\mathbf{R}$ is the response matrix and u is the unfolded spectrum. For the first iteration, the trial function is chosen to be the observed matrix r, given by

$$u^0 = r \Rightarrow f^0 = \mathbf{R}r \tag{5.4}$$

The second trial function u^1 consists of the previous trial u^0 function plus the difference between the real spectra and the calculated folded spectra f^0, denoted as

$$u^1 = u^0 + (r - f^0) \tag{5.5}$$

Following the same pattern, the next trial function is given by

$$u^2 = u^1 + (r - f^1) \tag{5.6}$$

which can be generalized as

$$u^{i+1} = u^i + (r - f^i) \tag{5.7}$$

for each iteration step i.

The steps of the unfolding, or difference approach, are:

1. Define the trial function u^i.
2. Calculate f^i, by folding u^i with the response matrix $\mathbf{R}$.
3. Calculate the difference between $r - f^i$.
4. If $r - f^i \approx 0$, then the process is done, otherwise steps two through four are repeated with a new trial function defined by Eq. 5.7.

The trial function of the last iteration is now the unfolded spectrum, denoted u_0.

Difference Method as Approximation of $\mathbf{R}^{-1}$

Mathematically, the unfolding approach is essentially approximating the inverse of the response matrix in order to determine the unfolded spectra u. Starting with Eq. 5.3, the unfolded spectra u, can be expressed as the inverse of the response matrix multiplied by the folded spectra f:

$$f = \mathbf{R}u \Rightarrow u = \mathbf{R}^{-1} f \tag{5.8}$$

From the Neumann series, the inversion of a matrix can be written

$$\mathbf{R}^{-1} = \sum_{i=0}^{\infty} (1 - \mathbf{R})^i \tag{5.9}$$

where 1 is the identity matrix. Therefore, u can be expressed as,

$$u^n = \mathbf{R}^{-1} f = \sum_{i}^{n} (1 - \mathbf{R})^i f \tag{5.10}$$

where n is the number of terms in the expansion. If we let $f = r$, we get

$$u^0 = (1 - \mathbf{R})^0 r = r \tag{5.11}$$

which was our original trial function in Eq. 5.4. Continuing onto the next term, u^1 is given by

$$\begin{aligned} u^1 &= (1-\mathbf{R})^0 r + (1-\mathbf{R})^1 r \\ &= r + r - \mathbf{R}r \end{aligned} \tag{5.12}$$

Replacing one of the r's with $u^0 = r$ and recalling that $f^i = \mathbf{R}u^i$, we get

$$u^1 = u^0 + r - f^0 \tag{5.13}$$

Writing out the expansion one more time for $n = 2$, the unfolded spectra for a three-term expansion is given by

$$u^2 = (1-\mathbf{R})^0 r + (1-\mathbf{R})^1 r + (1-\mathbf{R})^2 r \tag{5.14}$$

The first two terms are equivalent to u^1. Now we will show that the last term is equal to $r - f^1$.

$$\begin{aligned} (1-\mathbf{R})^2 r &= (1 - 2\mathbf{R} + \mathbf{R}^2) r \\ &= r - 2f^0 + \mathbf{R}f^0 \\ &= r - 2f^0 + \mathbf{R}(u^0 + r - u^1) \\ &= r - f^1 \end{aligned} \tag{5.15}$$

Plugging Eq. 5.15 into Eq. 5.14, we get

$$u^2 = u^1 + r - f^1 \tag{5.16}$$

It follows that for i expansion terms, the unfolded spectra can be expressed

$$u^{i+1} = u^i + r - f^i \tag{5.17}$$

which is identical to Eq. 5.7, thus showing that the iterative difference approach is equivalent to the Neumann series expansion of the inverse response matrix on the observed spectra. One can continue to calculate additional terms of the expansion until $r - \mathbf{R}u^n \approx 0$.

Compton Subtraction Method

The unfolding procedure has several challenges, including unknown uncertainties for every E_γ in the response matrix, as well as the statistical variance between channels of recorded data. These

uncertainties are propagated through the calculation and result in large fluctuations in the unfolded spectra [12]. Therefore, the Compton iterative subtraction method was developed and included in the unfolding procedure, described in .

The observed spectrum can be defined as the sum of all components of the γ-ray interactions within the detector given by,

$$r = u_f + u_s + u_d + u_a + u_C \tag{5.18}$$

where each term represents the spectra associated with the full energy peak u_f, single escape peak u_s, double escape peak u_d, annihilation peaks u_a, and the Compton background u_C, respectively. Each term can be written as the interaction probability p_{int} multiplied by the unfolded spectrum,u_0, shown below for the ith channel:

$$\begin{aligned} u_f(i) &= p_f u_0 \\ u_s(i - i_{511}) &= p_s u_0 \\ u_d(i - i_{1022}) &= p_d u_0 \\ u_a(i_{511}) &= \sum_{i_{min}}^{i_{max}} p_a u_0 \end{aligned} \tag{5.19}$$

where the channel number i corresponds to the γ-ray energy. Each spectrum is smoothed to match the experimental energy resolution. The Compton spectrum is then calculated by

$$u_C = r - (u'_f + u'_s + u'_d + u'_a) \tag{5.20}$$

where u' denotes the smoothed spectrum. The resulting spectrum is smoothed such that the content of each channel is replaced by a weighted average over a defined number of adjacent channels. The smoothed spectrum will be denoted u'_C. Rewriting Eq. 5.18 to solve for u_f gives,

$$u_f(i) = [r(i) - (u'_s(i) + u'_d(i) + u'_a(i) + u'_C(i))]/p_f(i) \tag{5.21}$$

Finally, the true unfolded spectrum U_{true} is written

$$U_{true}(i) = \frac{u_f(i)}{\epsilon_{tot}(i)} \tag{5.22}$$

where $\epsilon_{tot}(i)$ is the detector efficiency at the ith channel.

5.2.3 First Generation

After unfolding the raw matrix, the next step is to extract a matrix that contains the first γ ray emitted for every decay from an initial state E_i. This γ ray is called the primary, or first generation, γ ray. The first generation iterative procedure is performed for every excitation energy bin and is discussed in detail in Ref. The primary γ-ray spectrum for excitation bin i is defined as

$$h_i = u_i - g_i \tag{5.23}$$

where u_i is the unfolded spectrum for channel i, and g_i is the weighted sum of all unfolded spectra. The weighted spectrum can be expressed as

$$g_i = \sum_j n_{ij} w_i u_i \tag{5.24}$$

where w_i is the probability of decay from bin 1 to bin i, u_i is the unfolded spectrum for excitation energy bin E_i, and n_i is a normalization factor. The normalization factor can be written,

$$n_{ij} = \frac{\langle M_i \rangle A(u_j)}{\langle M_j \rangle A(u_i)} \tag{5.25}$$

where $\langle M \rangle$ is the multiplicity of the cascade for a decay from excitation energy E, and $A(u)$ is the area under the spectrum. The normalization is calculated for the ith and jth energy bin, but generally $j = 1$. With these equations, the first generation iterative subtraction method can proceed.

For the first iteration, a trial function is chosen for w_i, such as the Fermi gas model [REF]. However, it has been shown that the method is not very sensitive to the initial trial function [50]. Second, the primary spectrum h is calculated for excitation bin i with Eq. 5.23. Then, h is transformed into a new function called w_i', which is given by

$$w_i' = \mathbf{R}^{-1} h_i \tag{5.26}$$

Afterwards, w_i' is calibrated with the known energy calibration and its area is normalized to 1. If $w_i' \approx w_i$, then the primary matrix has been obtained, otherwise the procedure continues to the next iteration. Each iteration process can be summarized as follows:

1. Calculate $h_i = f_i - g_i$ for trial function w_i.

2. Transform h to get w_i', calibrate, and normalize the area to 1.

3. Compare the calculated w_i' with the original w_i.

4. If $w_i' \approx w_i$, stop, else repeat steps 1-4.

5.2.4 Extraction of NLD and γSF

The fourth step in the Oslo method is the simultaneous extraction of NLD and γSF functional from the primary matrix $P(E_i, E_\gamma)$ using external normalization, thoroughly discussed in Ref. [51]. We assume that $P(E_i, E_\gamma)$ is normalized such that the sum of $P(E_i, E_\gamma)$ over γ-ray energies from E_γ^{min} to $E_\gamma = E_i$ is unity. We also assume that $P(E_i, E_\gamma)$ is proportional to the level density of the final state $\rho(E_f)$ and the γ-ray transmission coefficient $\mathcal{T}(E_\gamma)$, where the γ-ray energy is equal to the difference in energy between the initial and final states, i.e. $E_\gamma = E_i = E_f$. Theoretically, the primary matrix can be approximated by

$$P_{theory}(E_x, E_\gamma) = \frac{\mathcal{T}(E_\gamma)\rho(E_x - E_\gamma)}{\sum_{E_\gamma'=E_\gamma^{min}}^{E_i} \mathcal{T}(E_\gamma')\rho(E_x - E_\gamma')} \tag{5.27}$$

Furthermore, the transmission coefficient $\mathcal{T}(E_\gamma)$ is related to the γ-ray strength function $f(E_\gamma)$ by

$$\mathcal{T}_{XL} = 2\pi E_\gamma^{(2L+1)} f_{XL}(E_\gamma), \tag{5.28}$$

where$X$ is the electromagnetic character (E for electric and M for magnetic) and L is the multipolarity. For the Oslo method, we assume that the radiation is primarily dipole radiation ($L = 1$). Moreover, the Brink hypothesis states that $\mathcal{T}$ is dependent only on E_γ and has no dependence on the initial state populated E_i, the final state of the transition E_f, or their spins [24].

It has been shown [51] that there exists an infinite number of solutions that satisfy Eq. 5.27. For any given solution ρ and $\mathcal{T}$, there exists a $\tilde{\rho}$ and $\tilde{\mathcal{T}}$ that form another valid solution, which can be expressed by

$$\begin{aligned} \tilde{\rho}(E - E_\gamma) &= Ae^{\alpha(E-E_\gamma)}\rho(E - E_\gamma) \\ \tilde{\mathcal{T}}(E_\gamma) &= Be^{\alpha E_\gamma}\mathcal{T}(E_\gamma) \end{aligned} \tag{5.29}$$

for any real A, B, and α. The goal is to find the ρ and $\mathcal{T}$ for the nucleus of interest, however, we only have access to the experimental matrix $P(E_x, E_\gamma)$, which as discussed above does not uniquely determine ρ and $\mathcal{T}$. This highlights the need for a method to find the solutions that fit the experimental data.

Starting with the experimental primary γ-ray matrix $P(E_i, E_\gamma)$, a ρ and $\mathcal{T}$ are determined through a χ^2 minimization method. This procedure is done simultaneously for both functions. After a ρ and $\mathcal{T}$ that can produce the experimental first gen matrix $P(E_x, E_\gamma)$ have been found, we must determine the A, B, and α that lead to the $\tilde{\rho}$ and $\tilde{\mathcal{T}}$ which uniquely describe our nucleus of interest.

5.2.5 Normalization of NLD and γSF

The final step of the Oslo method is to normalize the extracted $\rho(E_f)$ and $\mathcal{T}(E_\gamma)$, a unique process for each experimental data set. This step is not as standardized, because availability of experimental data varies across the nuclear chart. Nevertheless, there is a general approach for obtaining the parameters A, B, and α in Eq. 5.29. The first two parameters determine the absolute scaling of ρ and $\mathcal{T}$, respectively. The third parameter α is common to both functions and corresponds to the slope.

The NLD is fitted to the low-lying discrete energy levels at low excitation energy, typically up to 1-3 MeV. The upper end of the NLD is fit to the level density at the neutron separation energy, calculated from neutron resonance spacing data D_0 (if available). However, due to limitations in the ρ extraction energy range, the level density can only be determined up to $E_x^{max} - E_\gamma^{min}$, which is often 1-3 MeV below the separation energy S_n. Therefore, the NLD will need to be extrapolated to that energy. This inputs model-dependence to the level density. In addition, D_0 has not been measured for many isotopes. Physicists are always trying to figure out how to remove the need for theory in experimental measurements. This has led to development of the Shape method [28], which is discussed in Section 5.3. Normalization of the γSF uses $\langle\Gamma_\gamma(S_n)\rangle$, the average radiative width at the neutron separation energy from neutron resonance experiments, a fit to the extrapolation of the giant dipole resonance (GDR) to low energies, and other lower-energy γSF measurements

for nearby isotopes.

5.3 Shape Method

The Shape Method is a particular prescription of the Ratio Method, which is a model-independent technique utilized to extract the E_γ-dependence and slope of the γSF. The Ratio Method involves identifying the primary γ rays emitted during the decay from the quasi-continuum to low-lying discrete levels [52, 30], usually from a $particle$-γ-γ coincidence from average resonance capture experiments. The energy dependence of the γSF is preserved in the relative γ-ray intensities of primary transitions from a given E_i in the quasi-continuum region to two different low-lying levels of the same spin and parity (J^π), E_{L1} and E_{L2}. A ratio can be expressed as

$$R = \frac{N_{L1}(Ei)(E_i - E_{L2})^3}{N_{L2}(Ei)(E_i - E_{L2})^3} = \frac{f(E_i - E_{L1})}{f(E_i - E_{L2})} \tag{5.30}$$

where N_{L1} and N_{L1} are the γ intensities for the transitions to E_{L1} and E_{L1}, respectively [28] .

The first use of the Shape Method was published by Wiedeking et al. [] in which the authors presented a thorough comparison between the shape results from analysis on previously published Oslo data and the original Oslo Method results. The authors demonstrate the good agreement between the two methods, but with noted differences at higher E_γ, where the Oslo method underestimates the strength function, possibly due to structural effects [52]. The first implementation of the shape method using ?????? decay was presented in Meucher et al. []. Following this method eliminates one of the theory-based normalization points in the Oslo Method and replaces it with an experimentally-determined value, thus reducing systematic uncertainty.

5.3.1 Matrix Diagonals

The first step of the Shape Method is to obtain a E_x vs. E_γ matrix. This can be done via charged particle or scattering reactions, such as experiments used for the Oslo Method determination of the γSF, or β decay, like β-Oslo experiments. Thereafter, the spectra need to be corrected for the detector response in the same way as the Oslo unfolding process, described above. In the Oslo Shape method detailed in Ref. [52], the unfolding is followed by the first generation iterative subtraction method. The β-Oslo Shape method found that results did not change significantly when

using the raw matrix or the first generation matrix, therefore they chose to perform the analysis with the raw matrix to reduce theory input. At this point, a γ-ray matrix $P(E_i, E_\gamma)$ has been obtained and the next step is the to identify the diagonals D_j.

The initial excitation energy is defined by a range of energies within energy bin E_i. The γ transition energy is expressed as the difference between the initial and final excitation energies, $E_\gamma = E_i - E_f$. A direct decay to the ground state has $E_\gamma = E_i$. Each diagonal D_j is projected over a range ΔE_i and each pixel contains the intensity (number of counts) as a function of $E_x - E_\gamma$. If there are two diagonals, D_1 corresponding to the lower E_f level and D_2 corresponding to the higher E_f state. Each diagonal will appear as a peak around $E_{\gamma 1} = E_i - E_{f1}$ and $E_{\gamma 2} = E_i - E_{f2}$, respectively. The corresponding peaks can be fit with a Gaussian function on top of a linear background which provides N_{Lj} in Eq. 5.30.

5.3.2 Sewing Method

Pairs of points with x and y values $(E_{\gamma j}, N_{Lj}/E_{\gamma j}^3)$ are plotted for each of the excitation bins that cross with a diagonal. Each pair is linearly interpolated and the lower energy point of the neighboring pair is shifted to lie on the interpolated line. This process is performed for each pair until the energy-dependence, or shape, of the γSF is revealed. The strength function is further corrected for detector efficiency that depends on the multiplicity, but the details on this are beyond the scope of this thesis. The γ strength function corrected for detector efficiency has a slope determined directly from experimental data, which is then used to normalize the level density as well.

CHAPTER 6

ANALYSIS

The data analyzed in this thesis work was recorded during an experiment that took place at Argonne National Laboratory. The CARIBU fission source was used to produce a beam of ^{89}Br that was delivered to the experimental end station, which was described in detail in Chapter 4. Two tape sequences were chosen to characterize the γ spectra of the parent ^{89}Br ($t_{1/2}$ = 4.4 s) and daughter ^{89}Kr ($t_{1/2}$ = 3.15 min) nuclei. The tape sequence used for the parent ^{89}Br decay was 20 s beam on, 2 s beam off, and the ^{89}Kr daughter sequence was 20 s beam on, 20 s beam off. An additional sequence of 600 s on, 600 s beam off was used to characterize any further decay chain isotopes.

The data acquisition process produces files that contain the raw event information for every digitizer channel. The data is repackaged from a raw event file into a `ROOT` `TTree` file format using a DDAS tool called ddasdumper [53]. A `TTree` is a `ROOT` data structure in which each "branch" is an independent column that contains all of the time-ordered events for each channel. The generated `TTree` files are converted into SuN `TTree` files, where the channels are mapped such that each branch corresponds to a specific PMT energy and time. This chapter details the data analysis process, which utilized C++ and python programming languages, Jupyter data science software, the `ROOT` data analysis framework (version 6.32.08) [54], and the Oslo method software (version 1.1.6) [55].

6.1 Experimental Data

6.1.1 Gain Matching and Calibration

Gain Matching

Prior to any data analysis, several corrections must be made to the SuN PMTs and segments, specifically two processes called gain matching and calibration. Each PMT outputs an electrical signal that corresponds to the amount of energy deposited in the detector. That analog signal is digitized and converted to a channel number that must be calibrated to the correct energy. Since each PMT is unique, their responses are normalized such that the output signals are assigned the same channel number. This normalization process, called gain matching, is used to align

the PMTs' output channels for a given γ-ray energy. Gain matching is performed twice for each SuN experiment. Both instances use the room background spectrum of SuN, which is the energy spectrum of measurements of energy deposited in SuN without any radioactive sources present. One might think that this spectrum would be empty, but SuN is sensitive enough to detect radiation from the surroundings. ^{40}K is a naturally-occurring radioactive isotope that is present in common construction materials, such as concrete and cement. ^{40}K emit a 1460.8 keV γ ray that appears as a peak on top of continuum background. This peak is fit with a Gaussian plus linear function that gives the channel number of its centroid.

In the first instance of gain matching, the channels are normalized and a new voltage for each PMT is calculated. Each PMT is biased with the new voltage to align the ^{40}K peaks, and a new background spectrum is recorded. The second instance of gain matching is applied in software. The centroid channel number of each PMT is used to calculate a multiplicative factor that gives the same channel number when applied. Typically all PMTs are aligned to one of the central PMTs in segment 2 or 3. Fig. 6.1 shows the ^{40}K in each PMT, organized by segment, before and after gain matching. The gain matching values used in this analysis are listed in Table. 6.1.

Top PMT	A	Bot PMT	A
T1-1	0.9814	B1-1	0.9965
T1-2	1.0092	B1-2	0.9891
T1-3	1.0169	B1-3	1.0007
T2-1	1.0472	B2-1	0.9987
T2-2	0.9949	B2-2	1.0000
T2-3	1.0217	B2-3	1.0038
T3-1	1.0038	B3-1	1.0115
T3-2	0.9994	B3-2	0.9764
T3-3	1.0211	B3-3	0.9875
T4-1	1.0125	B4-1	0.9954
T4-2	1.0276	B4-2	1.0001
T4-3	1.0253	B4-3	1.0001

Table 6.1 Gain matching factors for $x'_{chan} = A\ x_{chan}$, where x_{chan} is the original channel number and x'_{chan} is the gain matched channel, for the SuN top and bottom PMTs.

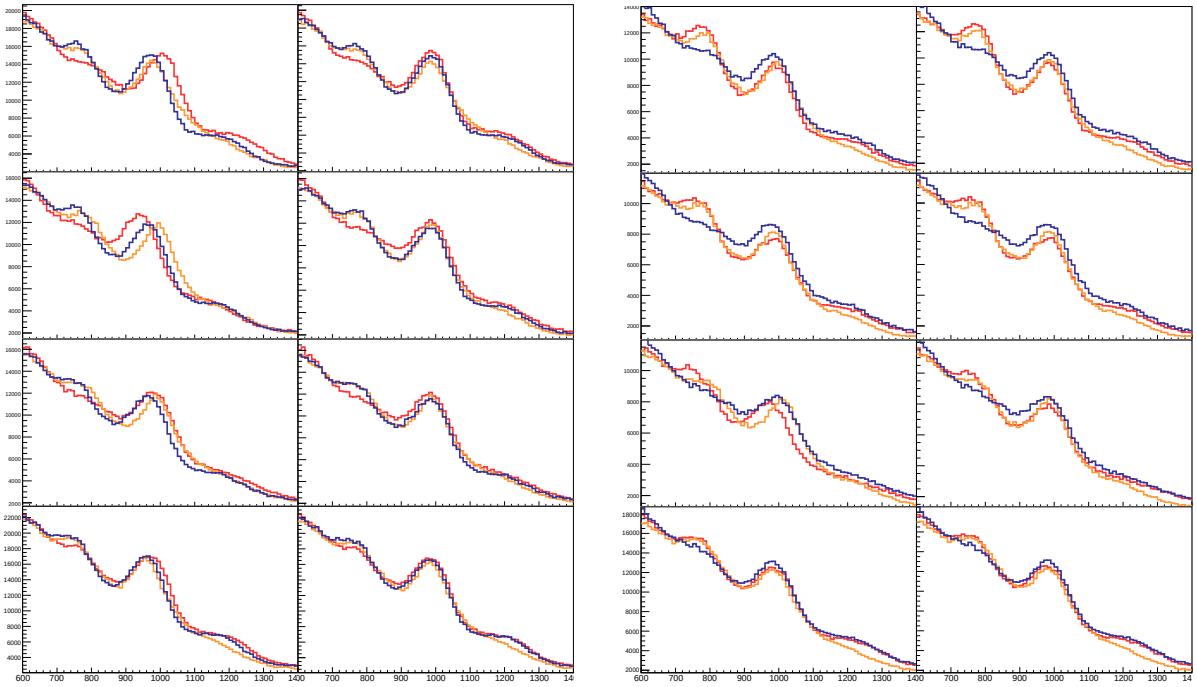

(a) SuN Top PMTs (b) SuN Bottom PMTs

Figure 6.1 SuN PMTs for the (a) top and (b) bottom segments. The left plots of (a) and (b) show the 1460 keV ^{40}K peak before gain matching. The right plots of both figures are the same plots after gain matching is performed. The central PMT of each segment is in orange, while the two side PMTs are shown in red and blue.

Calibration

After the SuN PMTs have been gain matched, their energies of the three PMTs of a single segment are added together on an event-by-event basis to create a SuN segment. This summing procedure is performed for the PMTs in each of the eight SuN segments. The spectrum of a SuN segment is given in channel number, so each segment needs to be calibrated to the correct energy for each channel. The calibration process begins with E_γ measurements of radioactive sources of known γ emission placed at the center of SuN. The amount of time required to accurately record the decay of each source depends on the source's activity level. The γ lines used for calibration are from ^{60}Co, located at 1173 and 1333 keV, ^{137}Cs at 662 keV, and ^{241}Am at 59 keV. Each peak is fit similarly to the gain matching fitting, but for a segment spectrum, not the individual PMT spectrum. The centroid channel numbers are plotted against the corresponding γ-ray energies and a linear fit is performed for each segment. Whereas some SuN experiments, such as reaction experiments,

require a polynomial fit, a linear calibration is typically sufficient for β-decay experimental data. The slope and y-intercept values for the SuN segments are given in Table 6.2. Plots of the calibrated segments are provided in Fig. 6.2.

SuN Segment	A	B
T1	0.4610	-36.77
T2	0.4700	-39.22
T3	0.4598	-32.24
T4	0.4644	-35.02
B1	0.4627	-34.54
B2	0.4644	-28.23
B3	0.4545	-21.68
B4	0.4602	-31.39

Table 6.2 Fit parameters A and B from a linear fit $E_\gamma = A * x_{chan} + B$. E_γ is the known γ-ray energy and x_{chan} is the centroid channel number. T is used to designate SuN top segments and B for the bottom segments, not to be confused with the y-intercept parameter B.

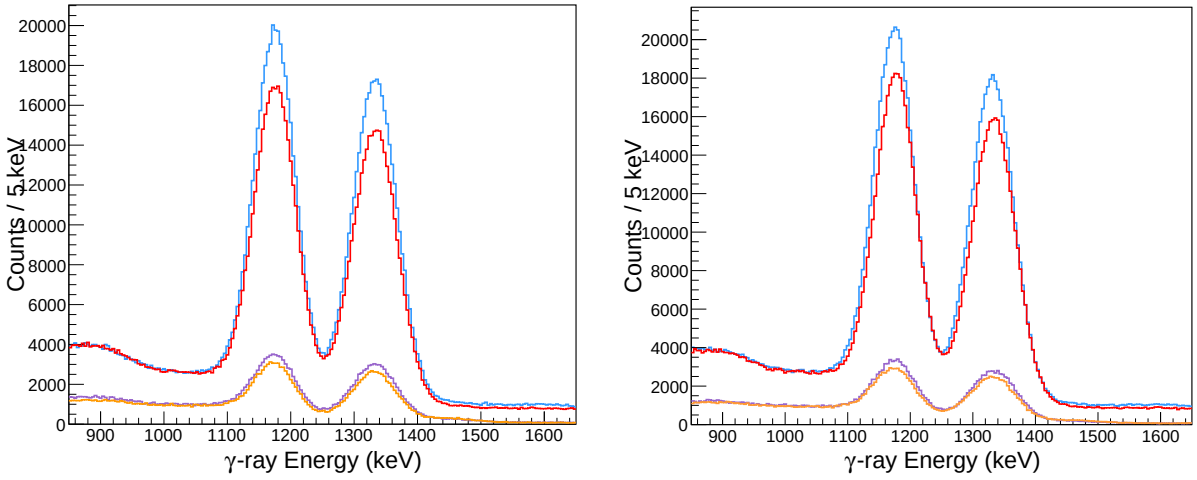

(a) (b)

Figure 6.2 Calibrated ^{60}Co spectra for SuN (a) top and (b) bottom segments.

6.1.2 Filtering Data

TAS Summation

One of the unique features about the SuN detector is its ability to measure both the individual γ rays emitted in a cascade and the total energy deposited in the detector which gives the initial excitation energy populated from β decay. A prime example of the summing technique is illustrated

by the β decay of ^{60}Co which populates the 2505 keV state of the ^{60}Ni nucleus that de-excites by a cascade of two γ rays, depicted in Fig. 6.3 [56]. The upper right panel shows the sum of segments spectrum for the decay of ^{60}Co, while the lower panel depicts the total absorption spectrum, or TAS. It is clear that the segment spectrum contains the γ-ray energies, whereas the TAS peak corresponds to the populated level at 2505 keV. This feature of the SuN detector allows for the use of analysis techniques that require measurements of individual γ transitions and populated states, such as the Oslo method.

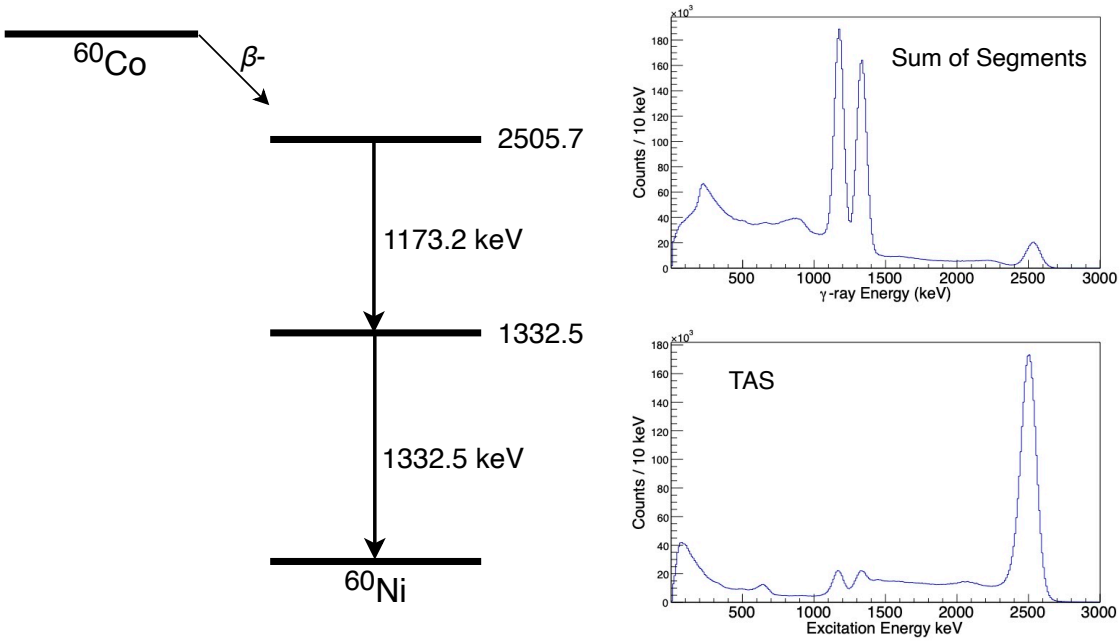

Figure 6.3 (Left) Cartoon decay scheme of the β decay of ^{60}Co. The upper right panel shows the sum of SuN segments, displaying large peaks that correspond to the γ-ray energies of the decay, and the lower right panel is the total absorption spectrum (TAS) with a large peak at the initially-populated energy level.

ROOT Files

Once the gain matching and calibration parameters are determined, the experimental data is processed on an event-by-event basis. The SuN `TTree` contains branches of the time and energy information for every SuN PMT, the two SuNSPOT PMTs, and the tape program signals. A similar procedure to creating the SuN `TTree` file is used to generate a new `ROOT` file that has the

same branches and three additional branches for the SuN segments, total energy (TAS), and folded SuNSPOT PMT time, which is discussed in more detail in Sec. 5.1.3. In each event, the SuN PMTs are gain matched and summed to create segments. The segments are calibrated and then summed to obtain the total energy deposited in the detector. The folded time is calculated by subtracting the time of the initial `BeamOn` event from the SuNSPOT PMT time, which shifts the time such that the grow-in starts at $t = 0$. A diagram illustrating this process is provided in Fig. 6.4.

The process of generating a new `TTree` implements several filtering algorithms. The first filter uses the tape status signals to label each event into one of three categories: `BeamOn`, `BeamOff`, or `MotorEnabled`. Events with the `MotorEnabled` label are rejected because that data includes noise induced from the motor. A second filter requiring a $\beta - \gamma$ coincidence can be applied, which reduced the data to events that contain β-decay coincidences. Finally, a lower threshold is set for the SuN segments, rejecting all events below the energy threshold. In this analysis, a segment threshold of 10 keV was used.

6.1.3 Background Subtraction

The next step of the analysis is to obtain a clean coincidence matrix of the excitation energy (TAS) versus the γ-ray energy (sum of segments) for ^{89}Kr, free from contamination from the daughter and granddaughter decays. To isolate the parent decay of ^{89}Br, the daughter-characterized spectrum is scaled and subtracted from a spectrum that contains both parent and daughter decays. This is done by applying gates in the folded time spectrum for the $\beta - \gamma$ coincidence events. Fig. 6.5 shows the TAS spectrum created with the events from the first 20 seconds of the folded time, shown in blue. The spectrum in purple is the TAS spectrum from the last 5 seconds of the decay, scaled by a factor of 6.3.

The peak at 2280 keV is primarily populated from the daughter decay of ^{89}Kr into ^{89}Rb, illustrated in Fig. 6.6. The counts above 3.6 MeV primarily consist of decays from the parent, and are shown to disappear shortly after the beam-off time at 20 s, however, the 2280 keV peak can be seen increasing in counts during the beam on time and subsequently decays at a slower rate during the decay period. The 2280 keV peak in both spectra was fit with a gaussian + linear function, and

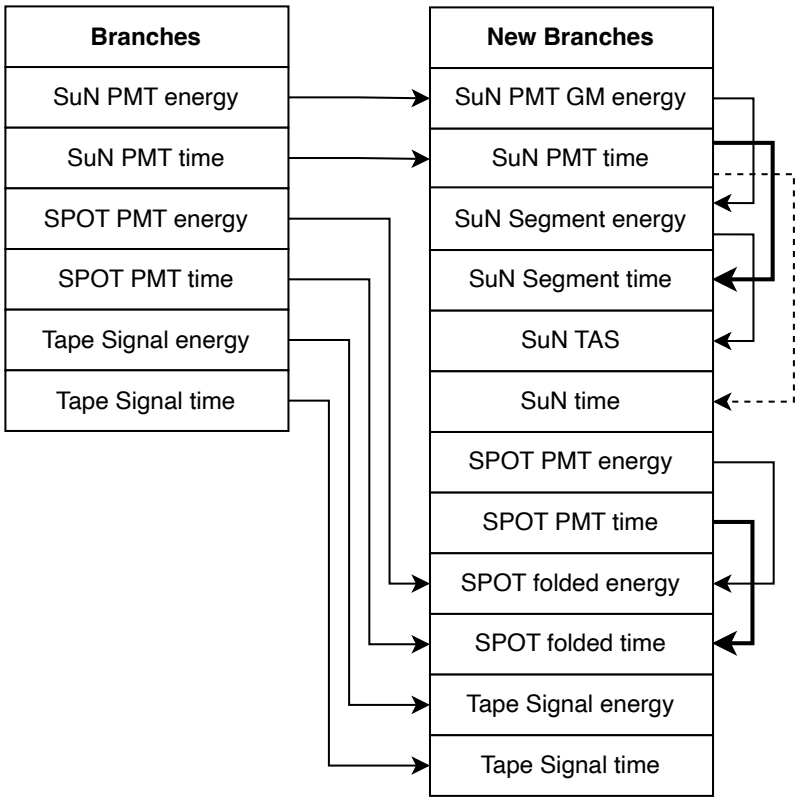

Figure 6.4 Depiction of mapping from SuN `TTree` to filtered `ROOT` file.

the gaussian function with the fit parameters was integrated to get an area. The scaling factor was calculated by finding the ratio between the two areas. Figs. 6.5 shows the TAS spectrum for the first 20 s (blue), the last 5 s (scaled in purple), and subtracted spectrum (gray).

The 2D matrices of excitation energy as a function of γ-ray energy are provided in Fig. 6.7 for the (a) first 20 s of beam on and the (b) last 5 s of the decay (unscaled). Finally, the fully contamination-subtracted 2D matrix is shown in Fig. 6.8. This completes the data processing portion of the analysis, which is following by the Oslo method analysis in described in the next section.

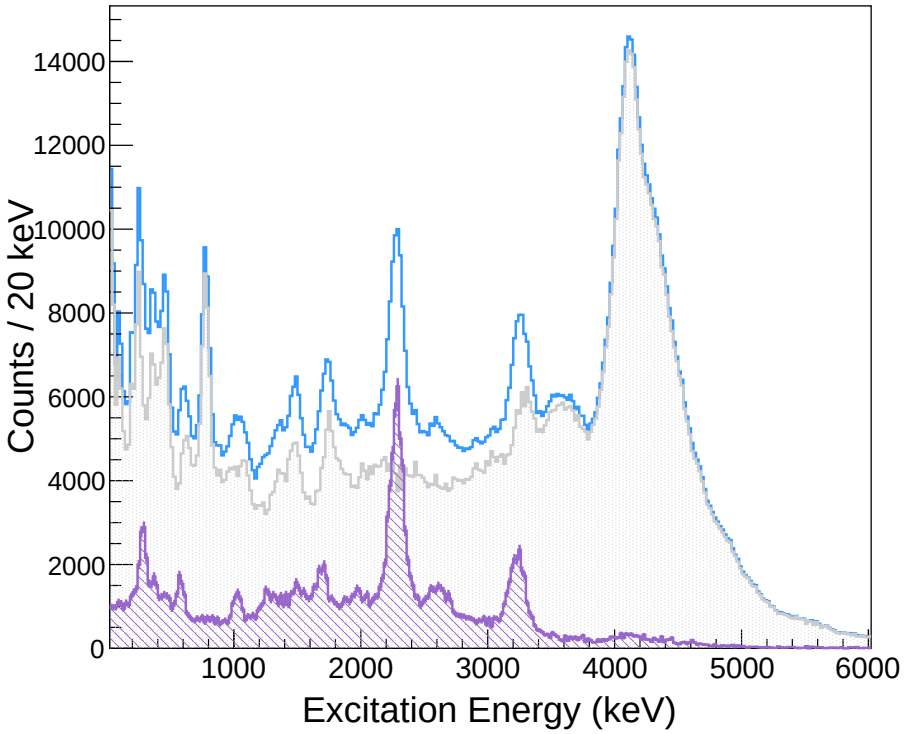

Figure 6.5 TAS spectra for a tape sequence of 20 s beam on, 20 s beam off. TAS with a gate on the first 20 s is shown in black and last 5 s (scaled by 6.3) in purple. The gray spectrum is the daughter-subtracted TAS.

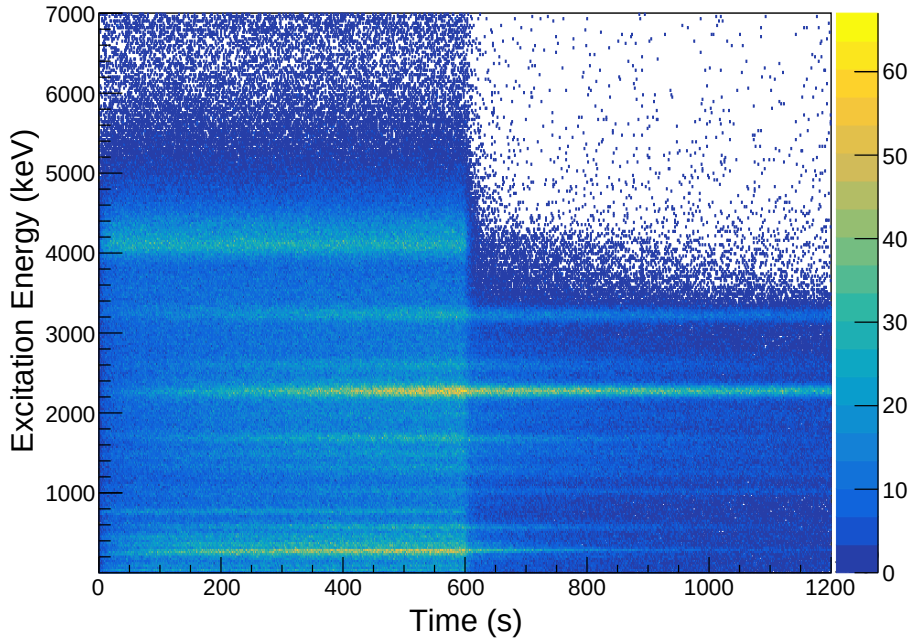

Figure 6.6 Excitation energy as a function of time for a tape sequence of 600 s beam on, 600 s beam off.

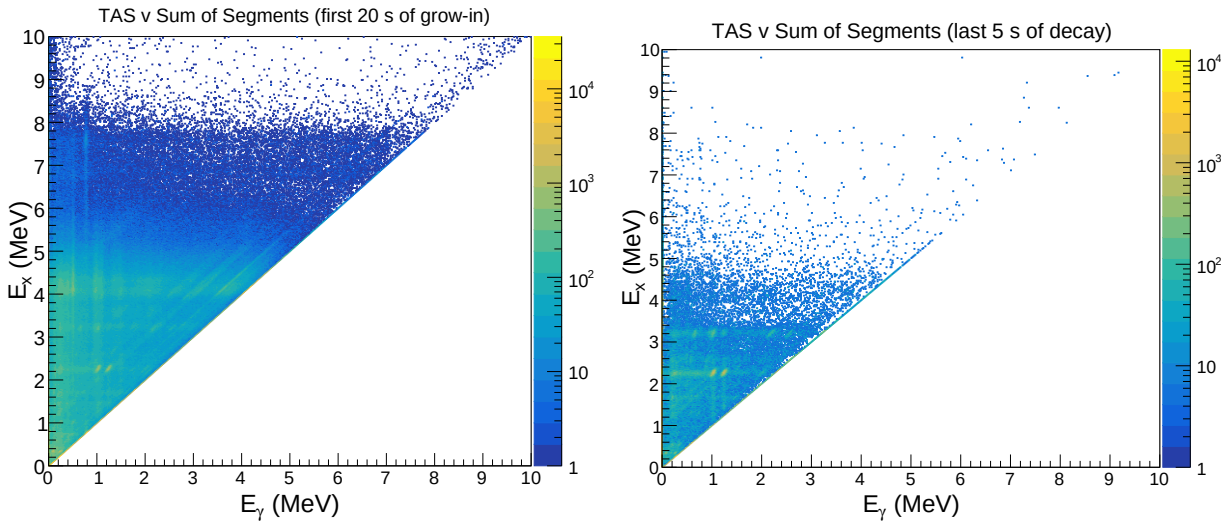

Figure 6.7 (a) TAS vs. Sum of Segments for the (a) first 20 s of the 20 s beam on, 20 s beam off/decay tape sequence and (b) the last 5 s of the 20 s beam on, 20 s beam off/decay tape sequence.

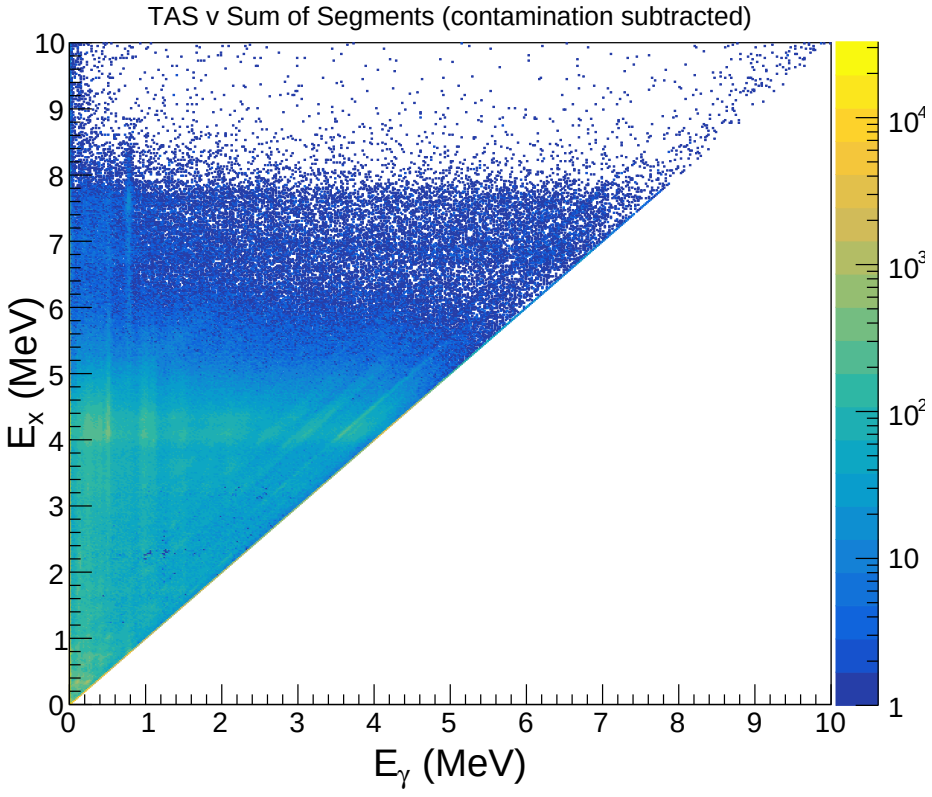

Figure 6.8 TAS vs. Sum of Segments matrix with contamination from the decay products subtracted.

6.2 Oslo Analysis

The Oslo method is performed using the Oslo analysis software, which is free to access through the University of Oslo Cyclotron Laboratory[55]. This software has been updated and improved upon since its creation 30 years ago. The version used in this analysis is written in Fortran, however a new, more user-friendly python version is now available [50]. This section focuses on the user interface side of the Oslo method, however, a detailed description of the procedure is presented in Sec. 5.2. The analysis process is illustrated by the flowchart in Fig. 6.9. The overall steps include (1) the unfolding of the raw experimental matrix, (2) determination of the primary γ rays emitted, (3) extraction of the nuclear level density (NLD) and γ strength function (γSF), and, finally, (4) normalization of the NLD and γSF.

6.2.1 Unfolding

The unfolding and first generation procedures are performed with a code called `MAMA`, which is short for MAtrix MAnipulation. This analysis used `MAMA` Version 7.6. The first step after the raw $\beta - \gamma$ coincidence matrix is obtained is to transform it from a ROOT file to a `MAMA` file in a format that is readable by the software. Next, a response matrix is generated for the experimental setup, in this case `Seg23 - SuN at MSU 2015 with target in center, GEANT4`, which is a response function for the four central segments of SuN. The experimental matrix is unfolded and 50 iterations of the Compton subtraction method are performed. The unfolding process results in a number of bins that have been over-subtracted, so the bins with negative counts are filled with an average of the counts in surrounding bins, and then any remaining negatives are set to zero. The unfolded matrix for ^{89}Kr is shown on the left side of Fig. 6.10.

6.2.2 First Generation

After the unfolding of the experimental matrix, the first γ rays from each cascade are extracted through the first generation method. An upper limit of the excitation energy is chosen to be the neutron separation energy S_n of the compound nucleus, which is 4.9 MeV for ^{89}Kr. The upper threshold for non-statistical γ rays was selected to be 411 keV. Ten iterations of the subtraction procedure were performed to obtain the primary γ-ray matrix shown on the right side of Fig. 6.10.

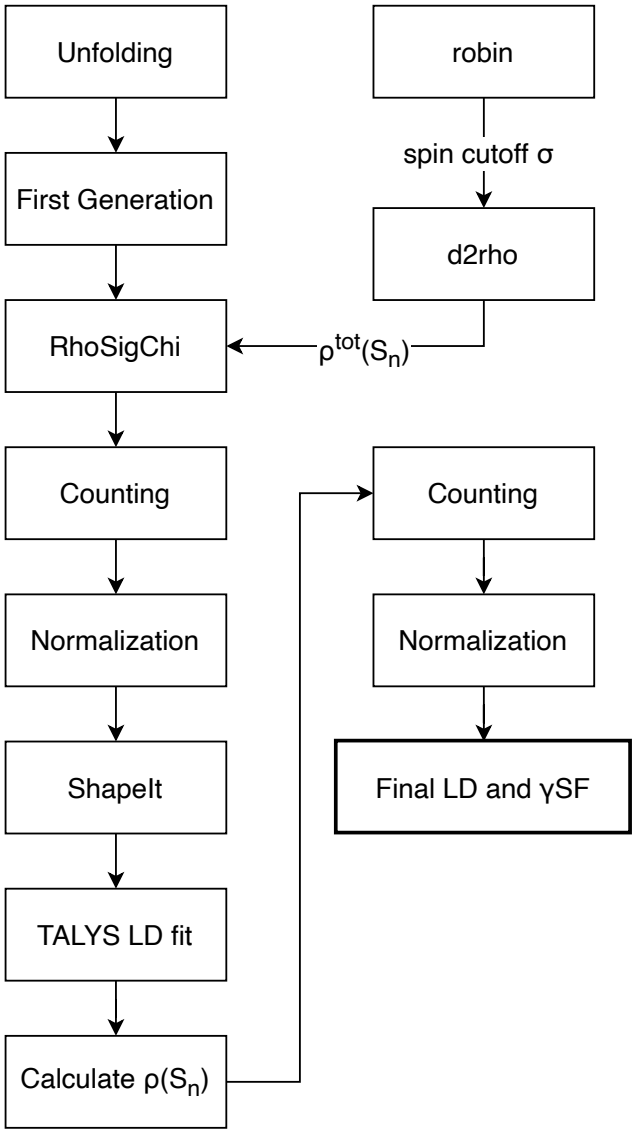

Figure 6.9 Flowchart depicting the analysis steps to obtain a NLD and γSF.

6.2.3 Extraction of NLD and γSF

The next step utilizes the program `rhosigchi` to extract the functional form of the level density and strength function. The input matrix is the first generation matrix compressed from 500×500 channels to 250×250 channels, which is done to reduce the number of empty bins. An upper and lower limit to the excitation energy are chosen, as well as a lower limit of the γ-ray energy. For

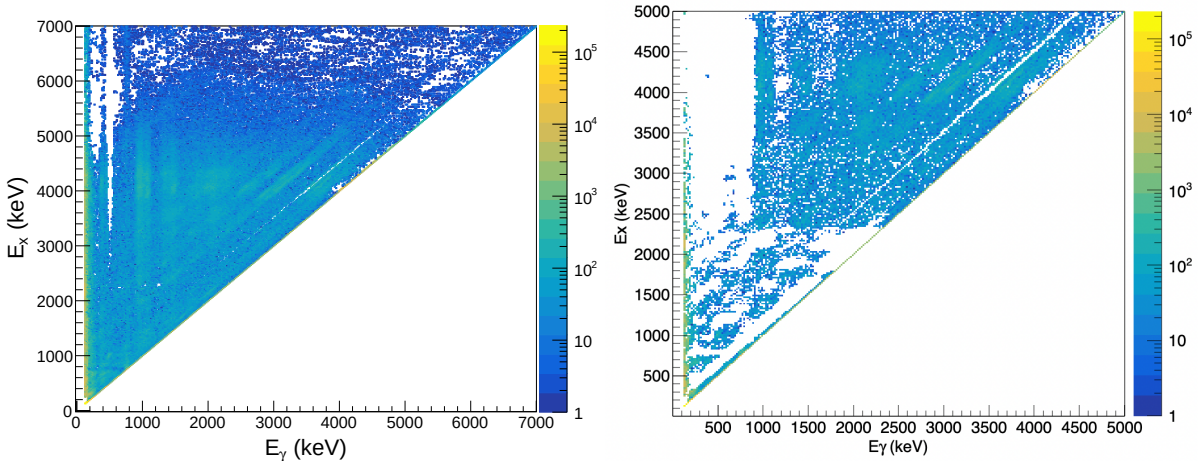

Figure 6.10 (a) Unfolded E_x vs. E_γ matrix. (b) First generation E_x vs. E_γ matrix

systematics, two lower E_x limits were used and are depicted in Fig. 6.11. We chose the excitation energy ranges 2.6 – 5.0 MeV and 3.6 – 5.0 MeV, with a γ-ray energy lower limit of 1450 keV. This results in a NLD $\rho(E_x)$ extracted up to 3.6 MeV for E_x^{min} = 2.6 MeV and up to 4.6 MeV for E_x^{min} = 3.6 MeV. The transmission coefficient, and thus the γSF, were extracted for the γ-ray energies 1450 – 5420 keV.

6.3 Normalization of NLD and γSF

The absolute level density and strength function is one set out of an infinite number of solutions to Eq. 5.27. The physical solution is obtained by normalizing the functions to available experimental data, given by

$$\begin{aligned} \tilde{\rho}(E - E_\gamma) &= Ae^{\alpha(E-E_\gamma)}\rho(E - E_\gamma) \\ \tilde{\mathcal{T}}(E_\gamma) &= Be^{\alpha E_\gamma}\mathcal{T}(E_\gamma) \end{aligned} \tag{6.1}$$

A, B and α are the normalization parameters for the extracted level density (LD) $\rho(E - E_\gamma)$ and transmission coefficient (TC) $\mathcal{T}(E_\gamma)$. A sets the magnitude of $\rho(E - E_\gamma)$, B normalizes the magnitude of $\mathcal{T}(E_\gamma)$, and α is a shared parameter that adjusts the slope of both functions. The normalization procedure involves setting upper and lower energy range in E_x and E_γ to fit $\rho(E-E_\gamma)$ and $\mathcal{T}(E_\gamma)$ to experimental, or, if unavailable, theoretical data. The bounds of the fit ranges are designated by arrows in Figs. 6.12 and 6.13.

First, the LD and TC are normalized with the program `counting`, which requires an input

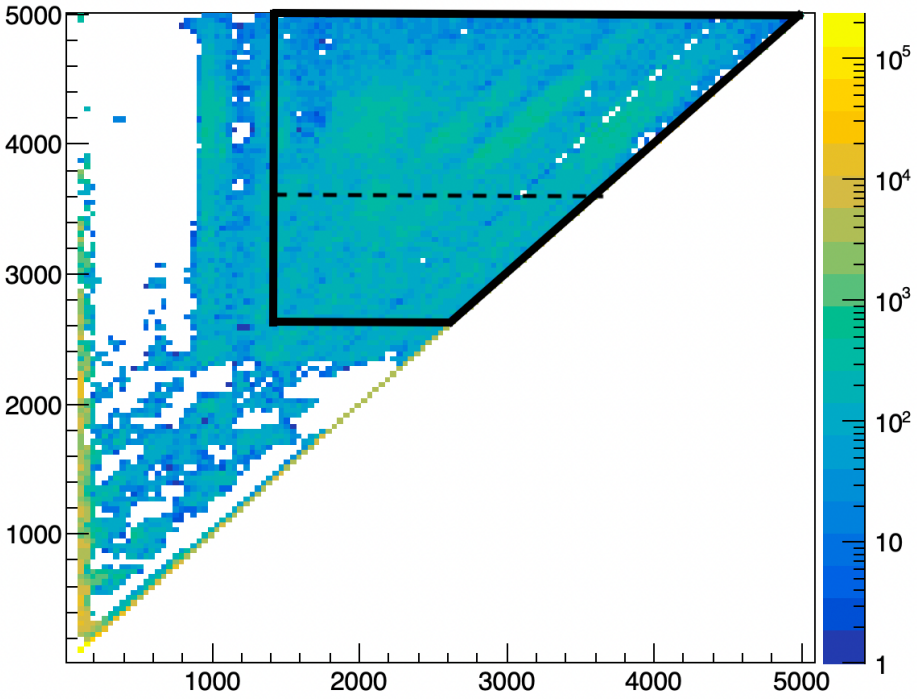

Figure 6.11 First generation matrix with the extraction area outlined by the solid black line. We used two limits for the lower excitation energy boundary, 2.6 MeV shown in the solid line and 3.6 MeV with the dashed line.

file containing the known discrete energy levels, as well as the total level density at the neutron separation energy $\rho^{tot}(E)$. The total level density can be calculated for a given D_0 by the program `d2rho`. The value for the neutron resonance capture spacing D_0 was chosen from the s-wave neutron resonance data for ^{86}Kr, the most neutron-rich krypton isotope available, from the `RIPL-3` database [CITE RIPL-3]. Additionally, the spin cut-off parameter and the level density model parameters are needed, which can be calculated with another Oslo method program called `robin`. Several options for spin cut-off formulas are provided in `robin`, however, the Fermi gas model by Egidy and Bucuescu is recommended [CITE EandB REFERENCE PRC 80, 054310 (2009)]. The spin cut-off σ is given by

$$\sigma^2 = 0.391A^{0.675}(E - 0.5Pa')^{0.312} \tag{6.2}$$

for mass number A, excitation energy E, and pairing energy Pa'. The suggested formulas for the level density are the back-shifted Fermi gas model (BSFG) and the constant temperature model

(CT). The BSFG formula is given by

$$\rho_{\mathrm{BSFG}}(E) = \frac{e^{2\sqrt{a(E-E_1)}}}{12\sqrt{2}\sigma a^{1/4}(E-E_1)^{5/4}} \tag{6.3}$$

where a is the level density parameter, E_1 is the total back-shifted energy parameter, and σ is the spin cut-off parameter from `robin`. The constant temperature model (CT),

$$\rho_{\mathrm{CT}}(E) = \frac{1}{T}e^{(E-E_0)/T} \tag{6.4}$$

has parameters for the constant temperature T and total back-shift energy E_0. This analysis implemented the BSFG model for $\rho(E)$ and the Fermi gas model for σ. After `robin` is used calculate $a, E_1,$ and σ, `d2rho` is used to calculate the total level density at the separation energy. Returning to `counting` the lower energy range of the level density is normalized to the discrete levels under 3 MeV, and the upper range is used to extrapolate $\rho(E)$ to the $E_x = S_n$. We chose to fit the lower energy range to the discrete levels around 2 MeV and the higher range to the 3-3.5 MeV region of the excitation energy. The extracted slope from the NLD is also applied to $\mathcal{T}(E_\gamma)$.

Table 6.3 Parameters used in Oslo analysis of ^{89}Kr.

Parameter	Value
σ	3.6
a	9.921 1/MeV
E1	0.082 MeV
$\rho(B_n)$	923.5 1/MeV
D_0	29000 eV
$\langle\Gamma_\gamma\rangle$	150 meV

The amplitude of the γSF is normalized with the aptly-named program `normalization`. It requires input values for D_0, the spin of the ground state of the target nucleus, and the average radiative width $\langle\Gamma_\gamma\rangle$ for s-wave resonances. The radiative width was also taken from the `RIPL-3`. We chose a range of $\langle\Gamma_\gamma\rangle$ values that spanned the data from other krypton isotopes, that is from 150 to 250 MeV. The normalized NLD, transmission coefficient, and γSF are shown in Figs 6.12 and 6.13.

To summarize, the NLD was fitted to the discrete levels around 2 MeV and the total level density at S_n was calculated and used to fit the slope. The γSF was normalized using D_0 and

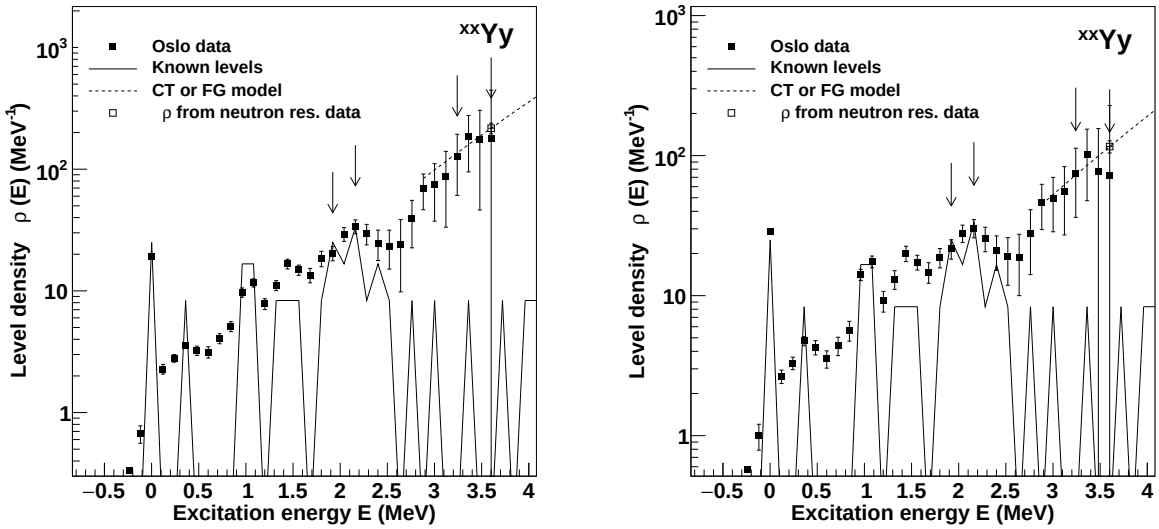

Figure 6.12 Normalized NLD for the minimum (right) and maximum (left) slope values determined with the Shape method.

$\langle\Gamma_\gamma\rangle$ values from lower mass krypton isotopes. All parameters are listed in Table 6.3. Besides the discrete levels, the normalization parameters were obtained from krypton isotopes with three or more fewer neutrons and calculated with theoretical models. Fortunately, the β decay of two additional isotopes were measured during this SuNTAN experiment, ^{88,90}Kr. Incidentally, ^{88}Kr made for an excellent candidate for the application of the Shape method for β-decay experiments described in 5.3. Mücher et. al presented the first model-independent measurement of the absolute partial NLD for radioactive isotopes away from the valley of stability in Ref. [57]. To reduce model-dependency, a new slope was extracted from the fit of the ^{89}Kr γSF from this analysis to the ^{88}Kr γSF from the Shape analysis.

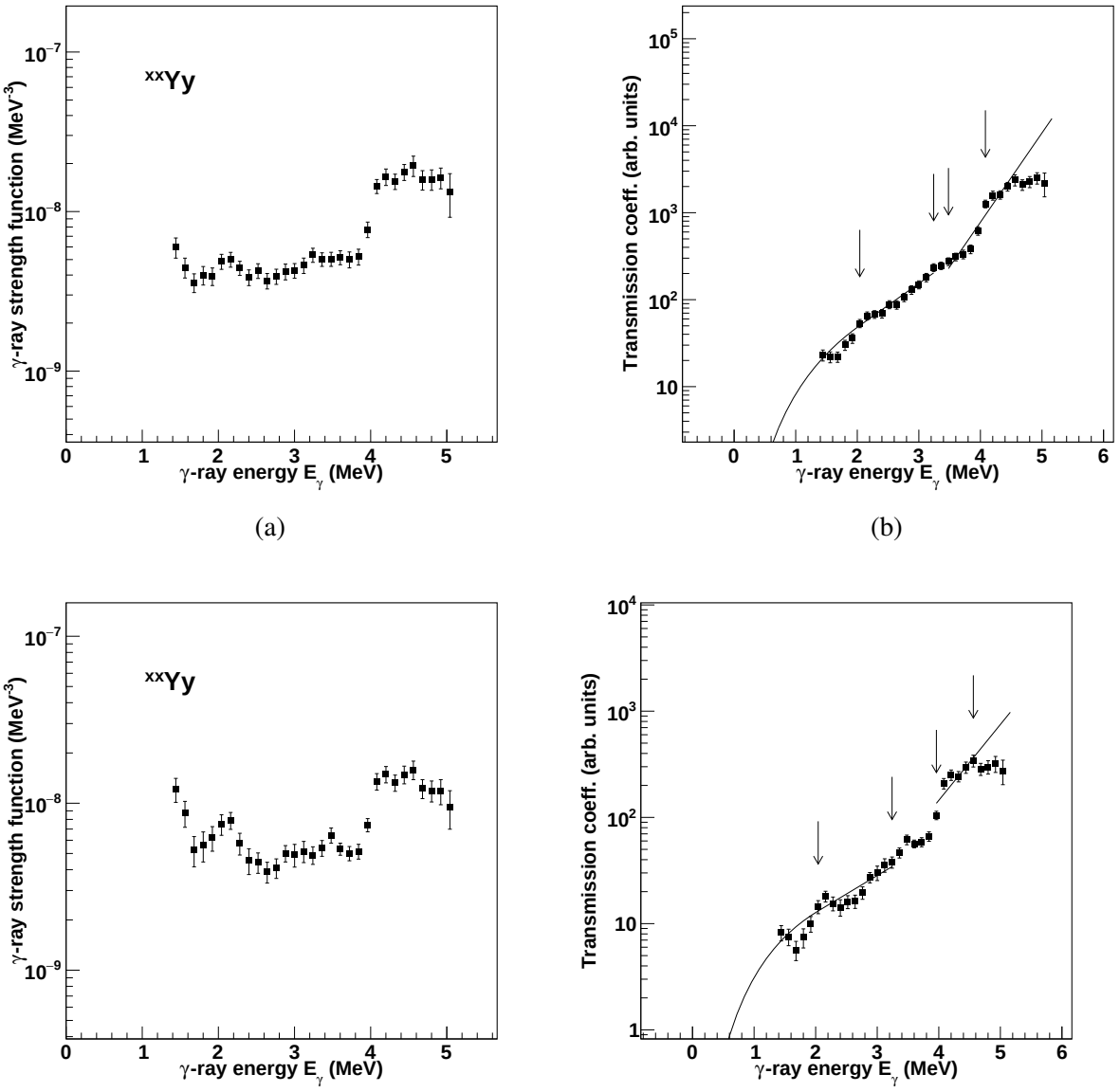

Figure 6.13 γSF (a,c) and Transmission Coefficient (b,d) for SuN upper (top) and lower (bottom) limits of α.

6.3.1 Shape Method

The Shape Method combined with the β-Oslo technique provided a model-independent determination of the α normalization parameter for ^{88}Kr. If the ^{89}Kr strength function can be fit to that of ^{88}Kr, then the only remaining parameter that depends on theoretical models is the absolute normalization of the γSF. The analysis code `ShapeIt` [REF HERE] was used to normalize the ^{89}Kr γSF to the ^{88}Kr γSF by linear interpolation and χ^2 minimization. This is a Monte Carlo process that calculates α for a given number of iterations. Different points of the ^{89}Kr γSF are shifted to the interpolated line, where the y-value of a given E_γ is randomly chosen that falls within its error bars. The output of this procedure is a Gaussian distribution of $\Delta\alpha$ values. Performing this process for the upper and lower γSF limits produced two $\Delta\alpha$ distributions, shown in Fig. 6.14. Each distribution was fit with a Gaussian function, and the centroids of the fit give an upper and lower slope parameter, $\Delta\alpha^{\text{high}} = 0.25 \pm 0.08$ and $\Delta\alpha^{\text{low}} = 0.03 \pm 0.1$. Fig. 6.15 shows the NLD and γSF for the full range of slope values obtained from the Shape procedure. Next, we return to the Oslo method codes to normalize the upper and lower pairs of level density and strength function.

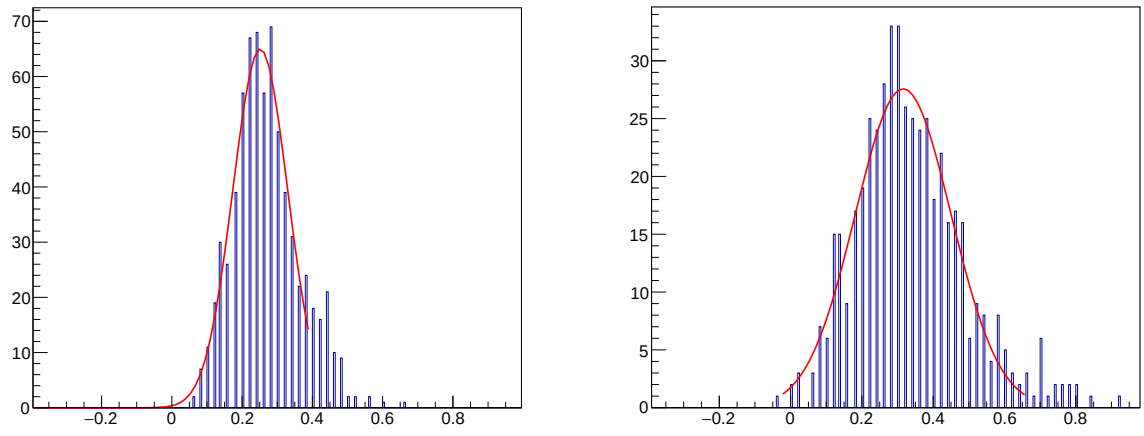

Figure 6.14 The distribution of α values from the MC fit of the ^{89}Kr γSF to that of ^{88}Kr. The centroids for the upper (left) and lower (right) γSF are 0.2538 ± 0.0802 of and 0.0333 ± 0.1042, respectively.

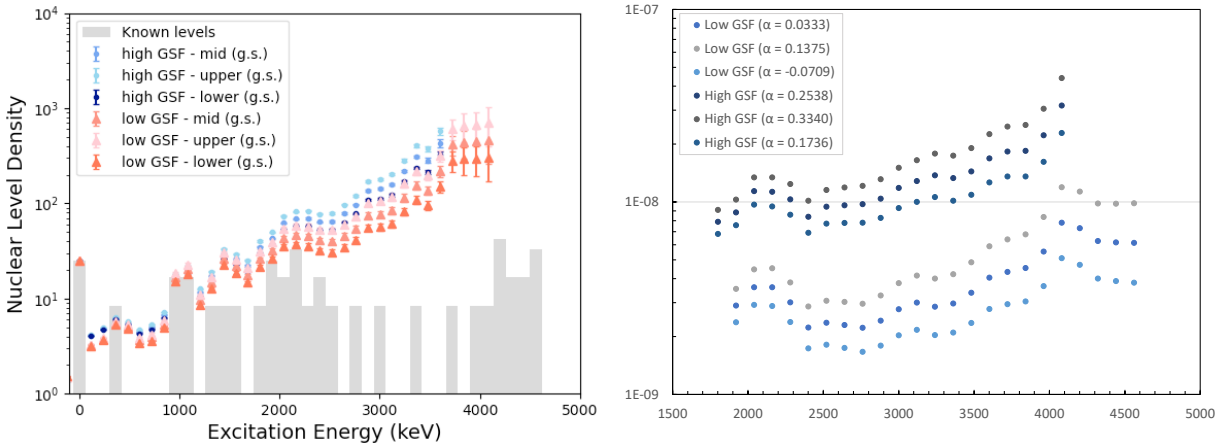

Figure 6.15 The NLD (left) and γSF (right) for all slope values.

6.3.2 Model-independent Normalization

The upper and lower values of the common slope parameter α need to be implemented in the Oslo normalization method. First, the NLD is normalized with `counting`, but rather than using the $\rho(S_n)$ calculated from `d2rho`, we use the y-value of the highest energy data point. This adjusted the NLD to match the slope extracted from `ShapeIt`. The Fermi gas model parameters remain the same, however the slope is unaffected as there is no more extrapolation beyond the NLD data points.

The normalization of the γSF requires a couple more steps as a new D_0 values needs to be calculated. This is done by first finding a NLD model that best fits the slope experimental data above 2.6 MeV. Details of the fitting process are provided in Sec. **??**. The model that best fit was `ldmodel` 5, which is the Hilaire-Goriely tables from TALYS. From this table, the level density can be found for $\rho(S_n, J^\pi = 1/2+)$ from which D_0 is calculated by $D_0 = 1/\rho(S_n, J^\pi = 1/2+)$. With the resonance spacing D_0 obtained, we can run `normalization` for the upper and lower $\langle\Gamma_\gamma\rangle$ values. All parameters used for the final normalization are provided in Table 6.4.

Table 6.4 Final parameters for the NLD and γSF from the Oslo analysis of ^{89}Kr.

Oslo Program	Parameter	$\alpha = 0.334$	$\alpha = -0.0709$
`counting`	E_x	3.6 MeV	3.6 MeV
	$\rho(E_x)$	217(22) 1/MeV	116(12) 1/MeV
	a	9.921 1/MeV	9.921 1/MeV
	E1	0.082 MeV	0.082 MeV
`normalization`	D_0	17956.55	34270.05
	$\langle\Gamma_\gamma\rangle$	150, 250 meV	150, 250 meV

CHAPTER 7

RESULTS AND DISCUSSION

7.1 ^{88}Kr(n,γ)^{89}Kr Cross Section and Reaction Rate

7.1.1 Fitting the NLD and γSF

After the extracted NLD and γSF have been normalized, a function is fitted to each data set to use as input in the HF code `TALYS` [10] for calculation of the (n,γ) reaction rates. TALYS has 6 NLD models and 9 γSF models, which include both microscopic and phenomenological models. In addition, γSF features, such as the upbend, scissors resonance, and pygmy resonance, can be included in the input file to better reproduce the data [48, 58].

The extracted NLD is a partial LD due to β^- decay and γ-emission rules. Assuming allowed β^- decays from the ^{89}Br ground state $(5/2^-)$ and dipole γ-ray emissions, the populated spin range is 1/2 to 9/2 for both positive and negative parity. It is important to only include level densities in the spin range when fitting the NLD. The theoretical NLD models were fit to the upper and lower NLD data sets in the energy region above 2.6 MeV. The best-fitting model was found by adjusting model parameters in the NLD model by Hilaire *et al.* [22] (ldmodel 5), shown in Fig. 7.1. Each NLD data set, named data set A and B, has a corresponding upper and lower γSF. The γSF limits are plotted with literature data from neighboring isotopes $^{85-87}$Kr.

Each γSF data set was fit with a GLO function to align with the tail of GDR data. The lower limit of γSF was fit to the $^{86}\mathrm{Kr}(\gamma,\gamma')$ data (green "down" triangles) by Schwengner *et al.* [58], while the upper limit was fit to the $^{86}\mathrm{Kr}(\gamma,\mathrm{n}')$ data (blue "up" triangles) by Raut *et al.* Below 3 MeV, the γSF was fit with an exponential function to describe the upbend observed in all data sets. There is another feature around 4.5 MeV that may be a signature of the Pygmy resonance, which appears to be more pronounced in data set A. Hence, a SLO function was fit to this energy region. The total γSF is the sum of each individual fit function and is shown as a shaded blue or purple band in Fig. 2.4. All model parameters are given in Table 7.1.

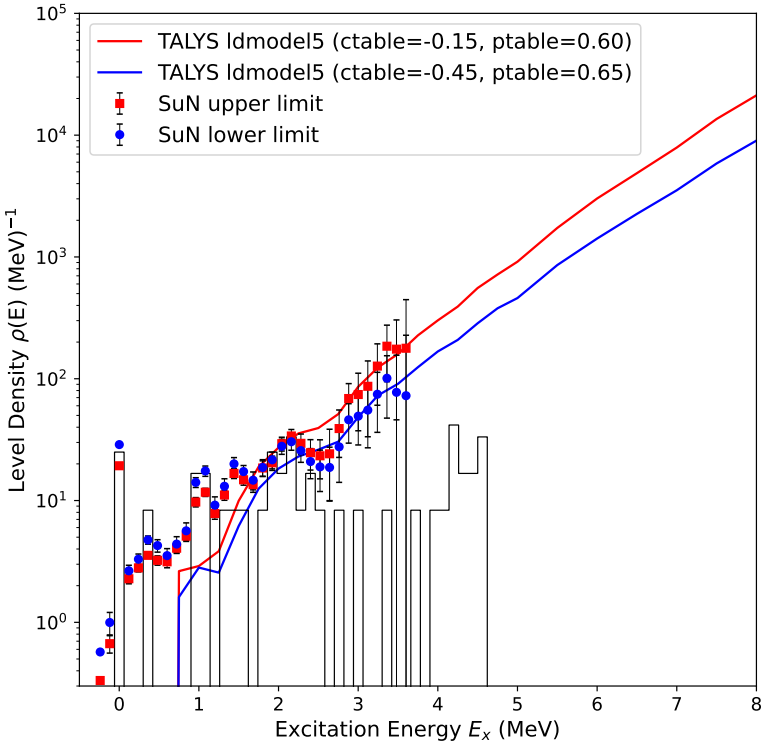

Figure 7.1 Normalized NLD

Parameter	Fit A (150)	Fit A (250)	Fit B (150)	Fit B (250)
E_{GLO}	17.0	17.0	17.0	17.0
Γ_{GLO}	10.0	15.0	10.0	15.0
σ_{GLO}	115	100	115	100
T	0.01	0.01	0.01	0.01
E_{SLO}	4.55	4.55	4.4	4.3
Γ_{SLO}	0.9	0.8	0.5	0.8
σ_{SLO}	0.7	1	0.3	0.3
$M1_{\mathrm{lin}}$	1×10^{-8}	1×10^{-8}	1×10^{-8}	1×10^{-8}
$M1_{\mathrm{exp}}$	0.5	0.5	0.8	0.75

Table 7.1 γSF it parameters

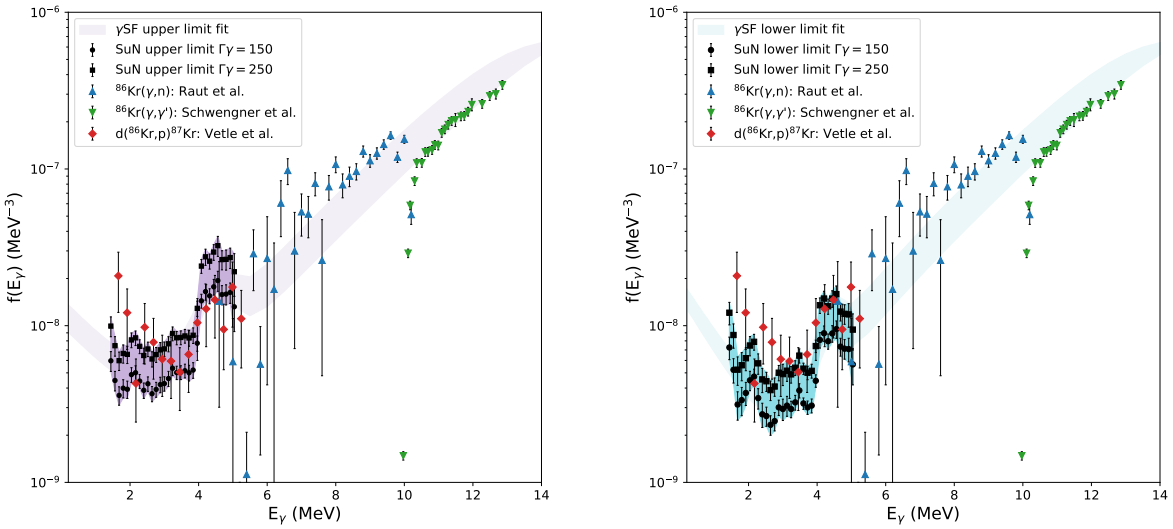

(a) (b)

Figure 7.2 Normalized γSF

7.1.2 TALYS Calculations

With the final fit parameters determined, the neutron-capture reaction rates can now be determined. Calculations for the ^{88}Kr(n,γ) reaction rate were performed with TALYS-1.96 for each pair of NLD and γSF functions. Fig. 7.3 shows the original (blue) band of reaction rates calculated with every combination of NLD + γSF with default parameters. The new reaction rate band (orange) of the present work has reduced uncertainty by a factor of 2. It is of note that the experimentally-constrained rate is systematically lower that the default rate from the REACLIB nuclear reaction library, which is commonly used in astrophysics models in the absence of experimental data.

7.2 Impact on i process

To continue the investigation of the underproduction of Sr calculated by i-process models, the new reaction rate was used to calculate abundance ratios for a range of neutron densities. Using the one-zone model by Denissenkov, 10000 Monte Carlo (MC) simulations were performed for $N_{\rm n} = 3.16 \times 10^{14}$ n/cm^3 and rates chosen randomly from within the theoretical uncertainties. One-zone models hold neutron density constant and utilize simplified astrophysical conditions. Fig. 7.4 (top panel) displays the number of MC simulations for a calculated Sr abundance ratio of that

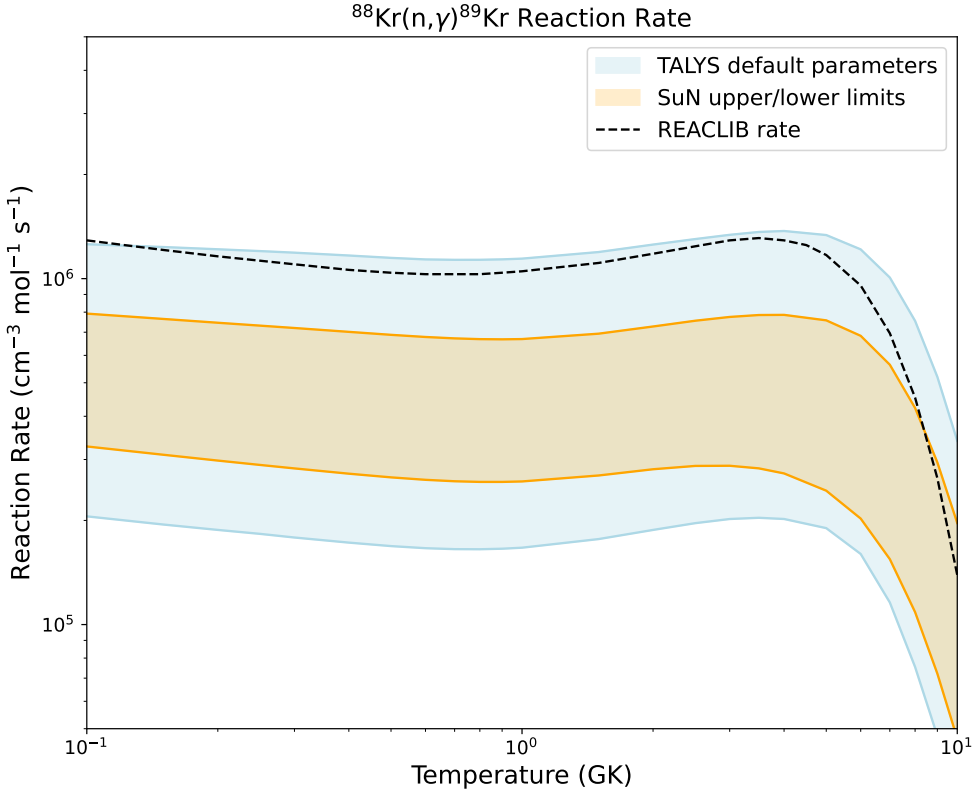

Figure 7.3 ^{88}Kr(n,γ)^{89}Kr reaction rate. The blue shaded band created from all possible combinations of TALYS γSF and NLD models. The orange shaded band is the constrained reaction rate. The black dotted line is the default reaction rate from the REACLIB reaction library used in the astrophysical models.

from the randomly-selected reaction rate to the default rate. Simulations that calculated higher than average rate are shown in blue, while the lower-than-average rate calculations are in yellow. The bifurcation indicates that Sr production is strongly dependent on the ^{88}Kr(n,γ) rate. The bottom panel provides the distribution of new MC simulations for the same ratio, but calculated from the new experimentally-constrained reaction rate from the present work. The new rate significantly reduces model uncertainty, as portrayed by the lack of bifurcation in the bottom figure.

A second set of one-zone simulations were performed for varying neutron densities N_n = 10^{12} – $10^{15.5}$ in an i-process model. Fig. 7.5 shows a collection of CEMP-s and CEMP-i stars, in blue and orange, respectively, plotted by their abundance ratios of Sr/Y and Y/Zr. The one-zone calculations for the default reaction rate are shown in the solid colored circles for the default reaction

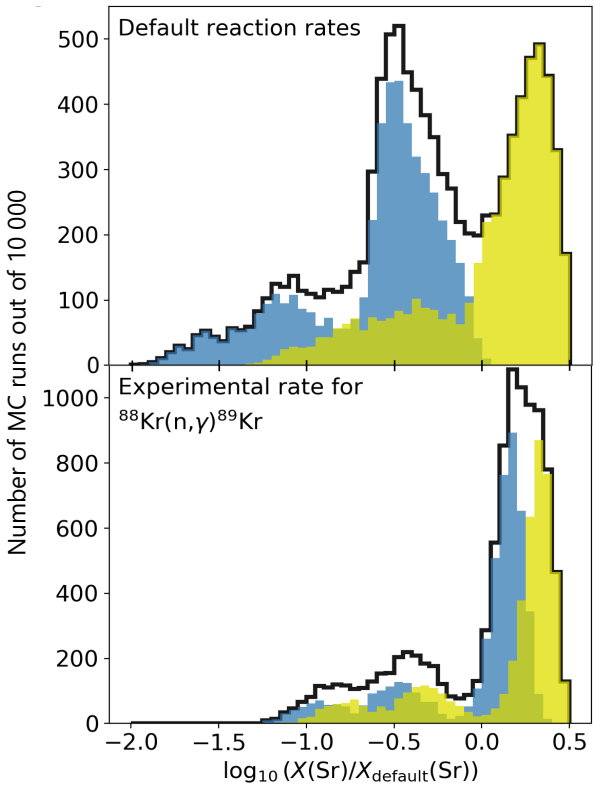

Figure 7.4 Caption

rate and solid colored stars represent those calculated with the rate from the present work. It can be seen that simulations with $N_n = 10^{14} - 10^{15}$n/cm^3 are able to predict the abundance ratios of the majority of stellar observations. However, the new rate does not correct the Sr underproduction for lower neutron densities. Even though one-zone models cannot reliably predict absolute elemental abundances, they are still a useful tool for investigating the impact of nuclear physics input on astrophysical models and were shown to be a reliable tool for predicting rations of neighboring elements.

Multi-zone nucleosynthesis models are more accurate than one-zone models at predicting elemental abundances, because they simulate more realistic stellar structure and conditions. Multi-zone simulations were performed for possible i-process sites, in this case the convective He-shell structure of RAWD model G [Den MNRAS 2019] with a 100 times increase of the H-ingestion rate and a peak neutron density of $N_n = 10^{15.4}$n/cm^3. The calculations for default rates in Fig. 7.5 show shifting to higher [Sr/Y] ratio, but the changes due to the new reaction rate are less drastic

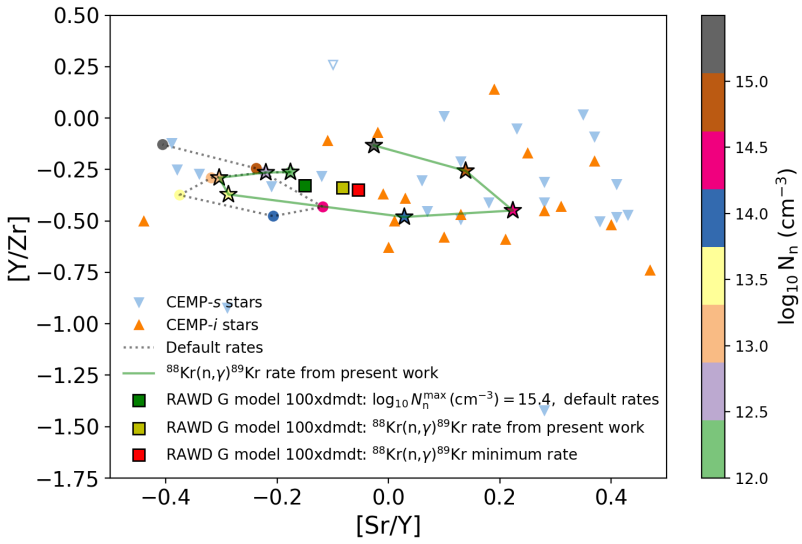

Figure 7.5 Caption

than those of the one-zone model.

CHAPTER 8

SUMMARY AND CONCLUSIONS

This thesis work was motivated by the fundamental goal to understand nucleosynthesis, specifically the neutron-capture processes that are responsible for heavy element production. The i process has gained attraction by the nuclear astrophysics community as more unique stars are studied. Interestingly, observational evidence of CEMP stars exhibit a Sr abundance that is under-produced by current i process models. Two sensitivity studies were performed that identified ^{88}Kr(n,γ)^{89}Kr as the reaction rate that most impacts Sr production in i-process environments.

The first measurement of the ^{88}Kr(n,γ)^{89}Kr reaction rate was presented. It was achieved by indirect techniques that populated the compound nucleus through β^- decay of ^{89}Br, from which the NLD and γSF were extracted, and the reaction rate was calculated with the HF code TALYS. The experiment was performed at ANL where a ^{89}Br beam was implanted in the SuNTAN tape transport system at the center of the SuN detector and surrounded by a β-particle detector (SuNSPOT). A significant portion of this thesis work involved the development, testing, and improvements of a tape transport system designed for use with the SuN detector. Analysis started with the subtraction of the daughter and granddaughter contamination from the E_x-E_γ matrix. The Oslo method was performed to extract the NLD and γSF, which were normalized to available data. Fit parameters were determined in order to use TALYS to calculate the new reaction rate.

To understand the impact the new reaction rate had on the Sr abundance predicted by i-process models, one-zone and multi-zone i-process nucleosynthesis simulations were performed and the results were compared to observational data of CEMP-s and CEMP-i stars. The new reaction rate strongly impacted one-zone simulations with high neutron density (N_n = 10^{14-15} n/cm^3), but the more realistic multi-zone models were not as affected. While one-zone models show improvement at reproducing observational data, multi-zone simulations may require additional modifications in order to make predictions that agree with observations. It is also possible that another reaction rate could further constrain these models. Many sensitivity studies have been performed recently, identifying more nuclear reactions that we aim to measure.

Overall, the i process is of growing interest among physicists and astronomers as a means to understand more evolutionarily-advanced stellar environments. This momentum drives observational discoveries and advancements in experimental capabilities as we reach for isotopes further from the valley of stability.

BIBLIOGRAPHY

[1] John J Cowan and William K Rose. PRODUCTION OF 14 C AND NEUTRONS IN RED GIANTS. *The Astrophysical Journal*, 14:149–158, 1977.

[2] M. R. Mumpower, R. Surman, G. C. McLaughlin, and A. Aprahamian. The impact of individual nuclear properties on r-process nucleosynthesis. *Progress in Particle and Nuclear Physics*, 86:86–126, 1 2016. ISSN 0146-6410. doi: 10.1016/J.PPNP.2015.09.001.

[3] Pavel Denissenkov, Georgios Perdikakis, Falk Herwig, Hendrik Schatz, Christian Ritter, Marco Pignatari, Samuel Jones, Stylianos Nikas, and Artemis Spyrou. The impact of (n, γ) reaction rate uncertainties of unstable isotopes near N = 50 on the i-process nucleosynthesis in He-shell flash white dwarfs. *Journal of Physics G: Nuclear and Particle Physics*, 45(5), 4 2018. ISSN 13616471. doi: 10.1088/1361-6471.

[4] Sébastien Martinet, Arthur Choplin, Stephane Goriely, and Lionel Siess. The intermediate neutron capture process IV. Impact of nuclear model and parameter uncertainties. *A&A*, 684:8, 2024. doi: 10.1051/0004-6361/202347734. URL https://doi.org/10.1051/0004-6361/202347734.

[5] A. C. Larsen, A. Spyrou, S. N. Liddick, and M. Guttormsen. Novel techniques for constraining neutron-capture rates relevant for r-process heavy-element nucleosynthesis, 7 2019. ISSN 01466410.

[6] A. Simon, S. J. Quinn, A. Spyrou, A. Battaglia, I. Beskin, A. Best, B. Bucher, M. Couder, P. A. Deyoung, X. Fang, J. Görres, A. Kontos, Q. Li, S. N. Liddick, A. Long, S. Lyons, K. Padmanabhan, J. Peace, A. Roberts, D. Robertson, K. Smith, M. K. Smith, E. Stech, B. Stefanek, W. P. Tan, X. D. Tang, and M. Wiescher. SuN: Summing NaI(Tl) gamma-ray detector for capture reaction measurements. *Nuclear Instruments and Methods in Physics Research, Section A: Accelerators, Spectrometers, Detectors and Associated Equipment*, 703: 16–21, 2013. ISSN 01689002. doi: 10.1016/j.nima.2012.11.045.

[7] C.M. Harris, M.K. Smith, A. Spyrou, and P.A. DeYoung. SuNTAN: A new tape transport system for beta-decay experiments. *Nuclear Instruments and Methods*, 2025.

[8] A. Spyrou, S. N. Liddick, A. C. Larsen, M. Guttormsen, K. Cooper, A. C. Dombos, D. J. Morrissey, F. Naqvi, G. Perdikakis, S. J. Quinn, T. Renstrøm, J. A. Rodriguez, A. Simon, C. S. Sumithrarachchi, and R. G.T. Zegers. Novel technique for constraining r -process (n, γ) reaction rates. *Physical Review Letters*, 113(23): 232502, 12 2014. ISSN 10797114. doi: 10.1103/PHYSREVLETT.113.232502. URL https://journals.aps.org/prl/abstract/10.1103/PhysRevLett.113.232502.

[9] S. N. Liddick, A. Spyrou, B. P. Crider, F. Naqvi, A. C. Larsen, M. Guttormsen, M. Mumpower, R. Surman, G. Perdikakis, D. L. Bleuel, A. Couture, L. Crespo Campo, A. C. Dombos, R. Lewis, S. Mosby, S. Nikas, C. J. Prokop, T. Renstrom, B. Rubio, S. Siem, and S. J. Quinn.

Experimental Neutron Capture Rate Constraint Far from Stability. *Physical Review Letters*, 116(24):242502, 6 2016. ISSN 10797114. doi: 10.1103/PHYSREVLETT.116.242502. URL https://journals.aps.org/prl/abstract/10.1103/PhysRevLett.116.242502.

[10] Arjan Koning, Stephane Hilaire, and Stephane Goriely. TALYS: modeling of nuclear reactions. *The European Physical Journal A*, 59(6):131, 6 2023. ISSN 1434-601X. doi: 10.1140/EPJA/S10050-023-01034-3.

[11] C Sagan, A Druyan, and S Soter. Cosmos: A Personal Voyage, 1980.

[12] Glenn F Knoll. Radiation Detection and Measurement (4th Edition). *John Wiley & Sons, Inc.*, 2010.

[13] Harry Bateman. Solution of a system of differential equations occurring in the theory of radioactive transformations. In *Cambridge Philos. Soc.*, pages 423–427, 1910.

[14] Walter Hauser and Herman Feshbach. The Inelastic Scattering of Neutrons. *Physical Review*, 87(2):366–373, 7 1952. ISSN 0031-899X. doi: 10.1103/PhysRev.87.366.

[15] G. Breit and E. Wigner. Capture of Slow Neutrons. *Physical Review*, 49 (7):519, 4 1936. ISSN 0031899X. doi: 10.1103/PhysRev.49.519. URL https://journals.aps.org/pr/abstract/10.1103/PhysRev.49.519.

[16] Roger D. Woods and David S. Saxon. Diffuse Surface Optical Model for Nucleon-Nuclei Scattering. *Physical Review*, 95(2):577, 7 1954. ISSN 0031899X. doi: 10.1103/PhysRev.95.577. URL https://journals.aps.org/pr/abstract/10.1103/PhysRev.95.577.

[17] H. A. Bethe. Nuclear Physics B. Nuclear Dynamics, Theoretical. *Reviews of Modern Physics*, 9(2):69, 4 1937. ISSN 00346861. doi: 10.1103/RevModPhys.9.69. URL https://journals.aps.org/rmp/abstract/10.1103/RevModPhys.9.69.

[18] W. Dilg, W. Schantl, H. Vonach, and M. Uhl. Level density parameters for the back-shifted fermi gas model in the mass range 40 < A < 250. *Nuclear Physics A*, 217(2):269–298, 12 1973. ISSN 0375-9474. doi: 10.1016/0375-9474(73)90196-6.

[19] A. Gilbert and A. G. W. Cameron. A COMPOSITE NUCLEAR-LEVEL DENSITY FORMULA WITH SHELL CORRECTIONS. 43(8):1446–1496, 8 2011. ISSN 0008-4204. doi: 10.1139/P65-139. URL https://cdnsciencepub.com/doi/10.1139/p65-139.

[20] S. Goriely, S. Hilaire, and A. J. Koning. Improved microscopic nuclear level densities within the Hartree-Fock-Bogoliubov plus combinatorial method. *Physical Review C - Nuclear Physics*, 78(6):064307, 12 2008. ISSN 1089490X. doi: 10.1103/PHYSREVC.78.064307. URL https://journals.aps.org/prc/abstract/10.1103/PhysRevC.78.064307.

[21] S. Hilaire and S. Goriely. Global microscopic nuclear level densities within the HFB plus

combinatorial method for practical applications. *Nuclear Physics A*, 779:63–81, 11 2006. ISSN 0375-9474. doi: 10.1016/J.NUCLPHYSA.2006.08.014.

[22] S. Hilaire, M. Girod, S. Goriely, and A. J. Koning. Temperature-dependent combinatorial level densities with the D1M Gogny force. *Physical Review C - Nuclear Physics*, 86(6):064317, 12 2012. ISSN 1089490X. doi: 10.1103/PHYSREVC.86.064317. URL https://journals.aps.org/prc/abstract/10.1103/PhysRevC.86.064317.

[23] R. Capote, M. Herman, P. Obložinský, P. G. Young, S. Goriely, T. Belgya, A. V. Ignatyuk, A. J. Koning, S. Hilaire, V. A. Plujko, M. Avrigeanu, O. Bersillon, M. B. Chadwick, T. Fukahori, Zhigang Ge, Yinlu Han, S. Kailas, J. Kopecky, V. M. Maslov, G. Reffo, M. Sin, E. Sh Soukhovitskii, and P. Talou. RIPL – Reference Input Parameter Library for Calculation of Nuclear Reactions and Nuclear Data Evaluations. *Nuclear Data Sheets*, 110(12):3107–3214, 12 2009. ISSN 0090-3752. doi: 10.1016/J.NDS.2009.10.004.

[24] D.M. Brink. *PhD Thesis*. PhD thesis, Oxford University, 1955.

[25] Peter Axel. Electric Dipole Ground-State Transition Width Strength Function and 7-Mev Photon Interactions. *Physical Review*, 126(2): 671, 4 1962. ISSN 0031899X. doi: 10.1103/PhysRev.126.671. URL https://journals.aps.org/pr/abstract/10.1103/PhysRev.126.671.

[26] J Kopecky and M Uhl. Test of gamma-ray strength functions in nuclear reaction model calculations. *Physical Review C*, 41(5), 1990.

[27] A. Voinov, E. Algin, U. Agvaanluvsan, T. Belgya, R. Chankova, M. Guttormsen, G. E. Mitchell, J. Rekstad, A. Schiller, and S. Siem. Large enhancement of radiative strength for soft transitions in the quasicontinuum. *Physical Review Letters*, 93(14): 142504, 10 2004. ISSN 00319007. doi: 10.1103/PHYSREVLETT.93.142504. URL https://journals.aps.org/prl/abstract/10.1103/PhysRevLett.93.142504.

[28] M. Wiedeking, L. A. Bernstein, M. Krti{\u{c}}ka, D. L. Bleuel, J. M. Allmond, M. S. Basunia, J. T. Burke, P. Fallon, R. B. Firestone, B. L. Goldblum, R. Hatarik, P. T. Lake, I. Y. Lee, S. R. Lesher, S. Paschalis, M. Petri, L. Phair, and N. D. Scielzo. Low-energy enhancement in the photon strength of Mo95. *Physical Review Letters*, 108(16): 162503, 4 2012. ISSN 00319007. doi: 10.1103/PHYSREVLETT.108.162503. URL https://journals.aps.org/prl/abstract/10.1103/PhysRevLett.108.162503.

[29] M. Krti\u{c}ka, M. Wiedeking, F. Be\u{c}v\'{a}\u{r}, and S. Valenta. Consistency of photon strength function models with data from the Mo 94 (d, p$\gamma\gamma$) reaction. *Physical Review C*, 93(5):054311, 5 2016. ISSN 24699993. doi: 10.1103/PHYSREVC.93.054311. URL https://journals.aps.org/prc/abstract/10.1103/PhysRevC.93.054311.

[30] M. D. Jones, A. O. MacChiavelli, M. Wiedeking, L. A. Bernstein, H. L. Crawford, C. M. Campbell, R. M. Clark, M. Cromaz, P. Fallon, I. Y. Lee, M. Salathe, A. Wiens, A. D.

Ayangeakaa, D. L. Bleuel, S. Bottoni, M. P. Carpenter, H. M. Davids, J. Elson, A. Görgen, M. Guttormsen, R. V.F. Janssens, J. E. Kinnison, L. Kirsch, A. C. Larsen, T. Lauritsen, W. Reviol, D. G. Sarantites, S. Siem, A. V. Voinov, and S. Zhu. Examination of the low-energy enhancement of the γ -ray strength function of Fe 56. *Physical Review C*, 97(2):024327, 2 2018. ISSN 24699993. doi: 10.1103/PHYSREVC.97.024327. URL https://journals.aps.org/prc/abstract/10.1103/PhysRevC.97.024327.

[31] A. C. Larsen, N. Blasi, A. Bracco, F. Camera, T. K. Eriksen, A. Görgen, M. Guttormsen, T. W. Hagen, S. Leoni, B. Million, H. T. Nyhus, T. Renstrøm, S. J. Rose, I. E. Ruud, S. Siem, T. Tornyi, G. M. Tveten, A. V. Voinov, and M. Wiedeking. Evidence for the dipole nature of the low-energy γ enhancement in Fe56. *Physical Review Letters*, 111 (24):242504, 12 2013. ISSN 00319007. doi: 10.1103/PHYSREVLETT.111.242504. URL https://journals.aps.org/prl/abstract/10.1103/PhysRevLett.111.242504.

[32] Fang Qi Chen, Y. F. Niu, Yang Sun, and Mathis Wiedeking. Origin of the Low-Energy Enhancement of the γ -Ray Strength Function. *Physical Review Letters*, 134(8): 082502, 2 2025. ISSN 10797114. doi: 10.1103/PHYSREVLETT.134.082502. URL https://journals.aps.org/prl/abstract/10.1103/PhysRevLett.134.082502.

[33] S. Goriely, N. Chamel, and J. M. Pearson. Skyrme-Hartree-Fock-Bogoliubov nuclear mass formulas: Crossing the 0.6 MeV accuracy threshold with microscopically deduced pairing. *Physical Review Letters*, 102(15):152503, 4 2009. ISSN 00319007. doi: 10.1103/PHYSREVLETT.102.152503. URL https://journals.aps.org/prl/abstract/10.1103/PhysRevLett.102.152503.

[34] S. Goriely, S. Hilaire, S. Péru, M. Martini, I. Deloncle, and F. Lechaftois. Gogny-Hartree-Fock-Bogolyubov plus quasiparticle random-phase approximation predictions of the M1 strength function and its impact on radiative neutron capture cross section. *Physical Review C*, 94(4):044306, 10 2016. ISSN 24699993. doi: 10.1103/PHYSREVC.94.044306. URL https://journals.aps.org/prc/abstract/10.1103/PhysRevC.94.044306.

[35] E. Margaret Burbidge, G. R. Burbidge, William A. Fowler, and F. Hoyle. Synthesis of the Elements in Stars. *Reviews of Modern Physics*, 29(4): 547, 10 1957. ISSN 00346861. doi: 10.1103/RevModPhys.29.547. URL https://journals.aps.org/rmp/abstract/10.1103/RevModPhys.29.547.

[36] B P Abbott. GW170817: Observation of Gravitational Waves from a Binary Neutron Star Inspiral. 2017. doi: 10.1103/PhysRevLett.119.161101.

[37] M Asplund, D L Lambert, T Kipper, D Pollacco, and M D Shetrone. The rapid evolution of the born-again giant Sakurai's object. *Astron. Astrophys*, 343:507–518, 1999.

[38] K. Cooper, C. S. Sumithrarachchi, D. J. Morrissey, A. Levand, J. A. Rodriguez, G. Savard, S. Schwarz, and B. Zabransky. Extraction of thermalized projectile fragments from a large volume gas cell. *Nuclear Instruments and Methods in Physics Research Section A: Accel-*

erators, Spectrometers, Detectors and Associated Equipment, 763:543–546, 11 2014. ISSN 0168-9002. doi: 10.1016/J.NIMA.2014.06.075.

[39] D. J. Morrissey, B. M. Sherrill, M. Steiner, A. Stolz, and I. Wiedenhoever. Commissioning the A1900 projectile fragment separator. *Nuclear Instruments and Methods in Physics Research Section B: Beam Interactions with Materials and Atoms*, 204:90–96, 5 2003. ISSN 0168-583X. doi: 10.1016/S0168-583X(02)01895-5.

[40] C. J. Prokop, S. N. Liddick, B. L. Abromeit, A. T. Chemey, N. R. Larson, S. Suchyta, and J. R. Tompkins. Digital data acquisition system implementation at the National Superconducting Cyclotron Laboratory. *Nuclear Instruments and Methods in Physics Research Section A: Accelerators, Spectrometers, Detectors and Associated Equipment*, 741:163–168, 3 2014. ISSN 0168-9002. doi: 10.1016/J.NIMA.2013.12.044.

[41] K. Starosta, C. Vaman, D. Miller, P. Voss, D. Bazin, T. Glasmacher, H. Crawford, P. Mantica, H. Tan, W. Hennig, M. Walby, A. Fallu-Labruyere, J. Harris, D. Breus, P. Grudberg, and W. K. Warburton. Digital Data Acquisition System for experiments with segmented detectors at National Superconducting Cyclotron Laboratory. *Nuclear Instruments and Methods in Physics Research Section A: Accelerators, Spectrometers, Detectors and Associated Equipment*, 610 (3):700–709, 11 2009. ISSN 0168-9002. doi: 10.1016/J.NIMA.2009.09.016.

[42] G. Savard, S. Baker, C. Davids, A. F. Levand, E. F. Moore, R. C. Pardo, R. Vondrasek, B. J. Zabransky, and G. Zinkann. Radioactive beams from gas catchers: The CARIBU facility. *Nuclear Instruments and Methods in Physics Research Section B: Beam Interactions with Materials and Atoms*, 266(19-20):4086–4091, 10 2008. ISSN 0168-583X. doi: 10.1016/J.NIMB.2008.05.091.

[43] T. D. Johnson, D. Symochko, M. Fadil, and J. K. Tuli. Nuclear Data Sheets for A = 142. *Nucl. Data Sheets*, 112:1949, 2011.

[44] Tsviki Y. Hirsh, Nancy Paul, Mary Burkey, Ani Aprahamian, Fritz Buchinger, Shane Caldwell, Jason A. Clark, Anthony F. Levand, Lin Ling Ying, Scott T. Marley, Graeme E. Morgan, Andrew Nystrom, Rodney Orford, Adrian Perez Galván, John Rohrer, Guy Savard, Kumar S. Sharma, and Kevin Siegl. First operation and mass separation with the CARIBU MR TOF. *Nuclear Instruments and Methods in Physics Research Section B: Beam Interactions with Materials and Atoms*, 376:229–232, 6 2016. ISSN 0168-583X. doi: 10.1016/J.NIMB.2015.12.037.

[45] A. C. Dombos, D. L. Fang, A. Spyrou, S. J. Quinn, A. Simon, B. A. Brown, K. Cooper, A. E. Gehring, S. N. Liddick, D. J. Morrissey, F. Naqvi, C. S. Sumithrarachchi, and R. G.T. Zegers. Total absorption spectroscopy of the β decay of Ga 76. *Physical Review C*, 93(6):064317, 6 2016. ISSN 24699993. doi: 10.1103/PHYSREVC.93.064317. URL `https://journals.aps.org/prc/abstract/10.1103/PhysRevC.93.064317`.

[46] Jun Chen and Balraj Singh. Nuclear Data Sheets for A = 42. *Nucl. Data Sheets*, 135:1, 2016.

[47] A. C. Larsen, M. Guttormsen, M. Krticka, E. Betak, A. Bürger, A. Görgen, H. T. Nyhus, J. Rekstad, A. Schiller, S. Siem, H. K. Toft, G. M. Tveten, A. V. Voinov, and K. Wikan. Analysis of possible systematic errors in the Oslo method. *Physical Review C*, 83(3), 11 2012. doi: 10.1103/PhysRevC.83.034315. URL http://arxiv.org/abs/1211.6264 http://dx.doi.org/10.1103/PhysRevC.83.034315.

[48] V. W. Ingeberg, S. Siem, M. Wiedeking, K. Sieja, D. L. Bleuel, C. P. Brits, T. D. Bucher, T. S. Dinoko, J. L. Easton, A. Görgen, M. Guttormsen, P. Jones, B. V. Kheswa, N. A. Khumalo, A. C. Larsen, E. A. Lawrie, J. J. Lawrie, S. N.T. Majola, K. L. Malatji, L. Makhathini, B. Maqabuka, D. Negi, S. P. Noncolela, P. Papka, E. Sahin, R. Schwengner, G. M. Tveten, F. Zeiser, and B. R. Zikhali. First application of the Oslo method in inverse kinematics. *The European Physical Journal A 2020 56:2*, 56 (2):1–9, 2 2020. ISSN 1434-601X. doi: 10.1140/EPJA/S10050-020-00070-7. URL https://link.springer.com/article/10.1140/epja/s10050-020-00070-7.

[49] M. Guttormsen, T. S. Tveter, L. Bergholt, F. Ingebretsen, and J. Rekstad. The unfolding of continuum γ-ray spectra. *Nuclear Instruments and Methods in Physics Research Section A: Accelerators, Spectrometers, Detectors and Associated Equipment*, 374(3):371–376, 6 1996. ISSN 0168-9002. doi: 10.1016/0168-9002(96)00197-0.

[50] J. E. Midtb{\o}, Fabio Zeiser, Erlend Lima, Ann Cecilie Larsen, Gry M. Tveten, Magne Guttormsen, Frank Leonel Bello Garrote, Anders Kvellestad, and Therese Renstr{\o}, m. A new software implementation of the Oslo method with rigorous statistical uncertainty propagation. *Computer Physics Communications*, 262:107795, 5 2021. ISSN 0010-4655. doi: 10.1016/J.CPC.2020.107795.

[51] A. Schiller, L. Bergholt, M. Guttormsen, E. Melby, J. Rekstad, and S. Siem. Extraction of level density and γ strength function from primary γ spectra. *Nuclear Instruments and Methods in Physics Research Section A: Accelerators, Spectrometers, Detectors and Associated Equipment*, 447(3):498–511, 6 2000. ISSN 0168-9002. doi: 10.1016/S0168-9002(99)01187-0.

[52] M. Wiedeking, M. Guttormsen, A. C. Larsen, F. Zeiser, A. Görgen, S. N. Liddick, D. Mücher, S. Siem, and A. Spyrou. Independent normalization for γ -ray strength functions: The shape method. *Physical Review C*, 104(1): 014311, 7 2021. ISSN 24699993. doi: 10.1103/PHYSREVC.104.014311. URL https://journals.aps.org/prc/abstract/10.1103/PhysRevC.104.014311.

[53] Jeromy Tompkins. ddasdumper : Converting data for ROOT analyses, 4 2016. URL https://docs.frib.msu.edu/daq/newsite/ddas-1.0/The.html.

[54] Rene Brun, Fons Rademakers, Philippe Canal, Axel Naumann, Olivier Couet, Lorenzo Moneta, Vassil Vassilev, Sergey Linev, Danilo Piparo, Gerardo GANIS, Bertrand Bellenot, Enrico Guiraud, Guilherme Amadio, wverkerke, Pere Mato, TimurP, Matevž Tadel, wlav, Enric Tejedor, Jakob Blomer, Andrei Gheata, Stephan Hageboeck, Stefan Roiser, marsupial, Stefan Wunsch, Oksana Shadura, Anirudha Bose, CristinaCristescu, Xavier Valls, and Raphael

Isemann. root-project/root, 2025. URL https://zenodo.org/records/3895860.

[55] Magne Guttormsen, Fabio Zeiser, Jørgen Eriksson Midtb{\o}, Vetle W. Ingeberg, and Ann-Cecilie Larsen. oslocyclotronlab/oslo-method-software: Oslo Method, 2025. URL https://zenodo.org/records/6024876.

[56] E. Browne and J.K. Tuli. Nuclear Data Sheets for A = 60. *Nucl. Data Sheets*, 114:1849, 2013.

[57] D. M{\"{u}}cher, A. Spyrou, M. Wiedeking, M. Guttormsen, A. C. Larsen, F. Zeiser, C. Harris, A. L. Richard, M. K. Smith, A. Görgen, S. N. Liddick, S. Siem, H. C. Berg, J. A. Clark, P. A. Deyoung, A. C. Dombos, B. Greaves, L. Hicks, R. Kelmar, S. Lyons, J. Owens-Fryar, A. Palmisano, D. Santiago-Gonzalez, G. Savard, and W. W. Von Seeger. Extracting model-independent nuclear level densities away from stability. *Physical Review C*, 107 (1):L011602, 1 2023. ISSN 24699993. doi: 10.1103/PHYSREVC.107.L011602. URL https://journals.aps.org/prc/abstract/10.1103/PhysRevC.107.L011602.

[58] R. Schwengner, S. Frauendorf, and A. C. Larsen. Low-energy enhancement of magnetic dipole radiation. *Physical Review Letters*, 111(23):232504, 12 2013. ISSN 00319007. doi: 10.1103/PHYSREVLETT.111.232504. URL https://journals.aps.org/prl/abstract/10.1103/PhysRevLett.111.232504.

APPENDIX A

EXPERIMENTAL SETTINGS

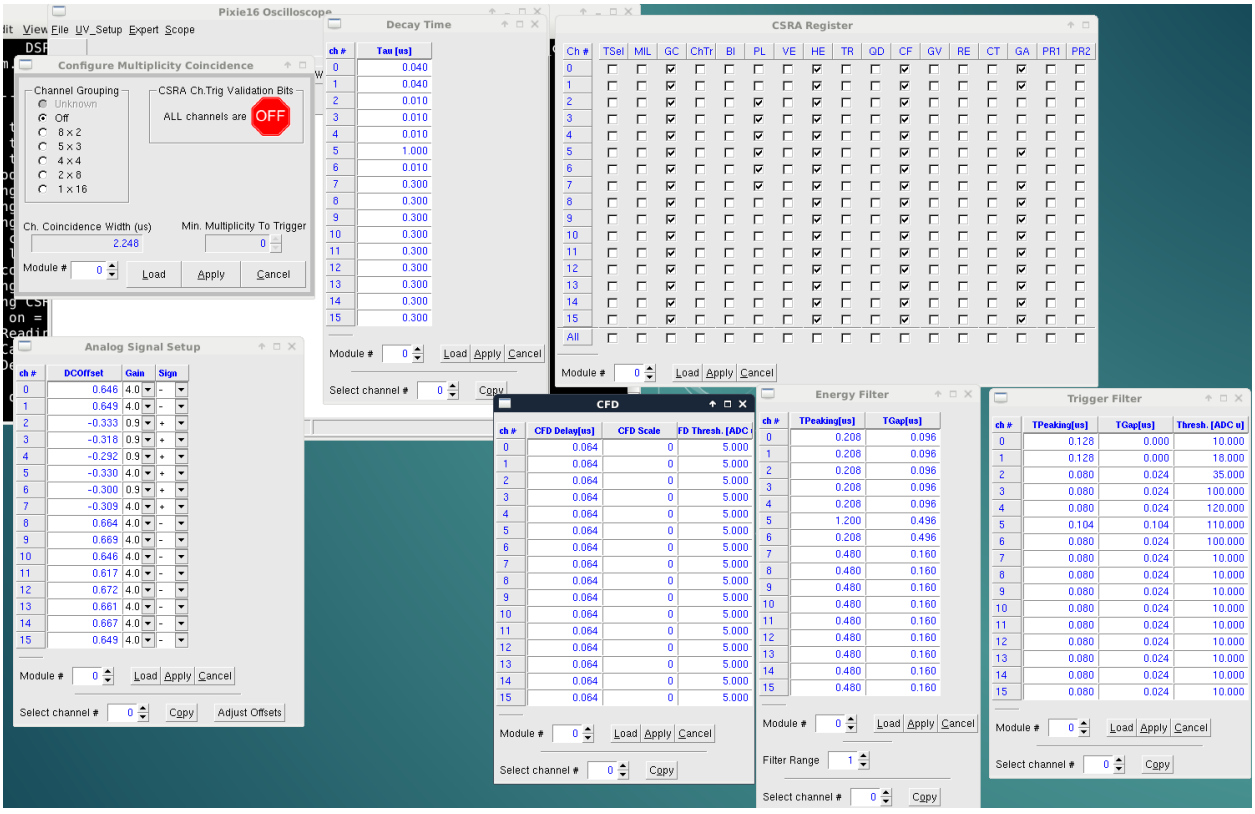

Figure A.1 Caption

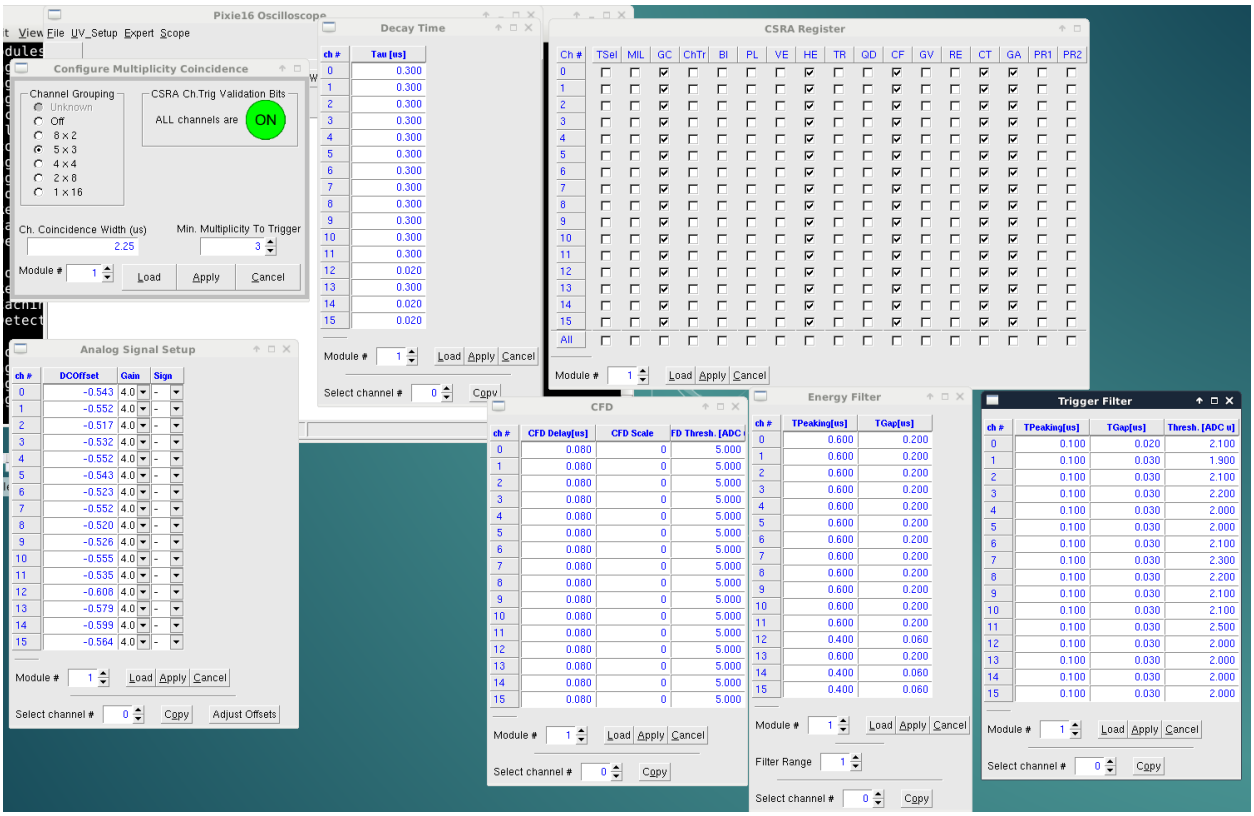

Figure A.2 Caption

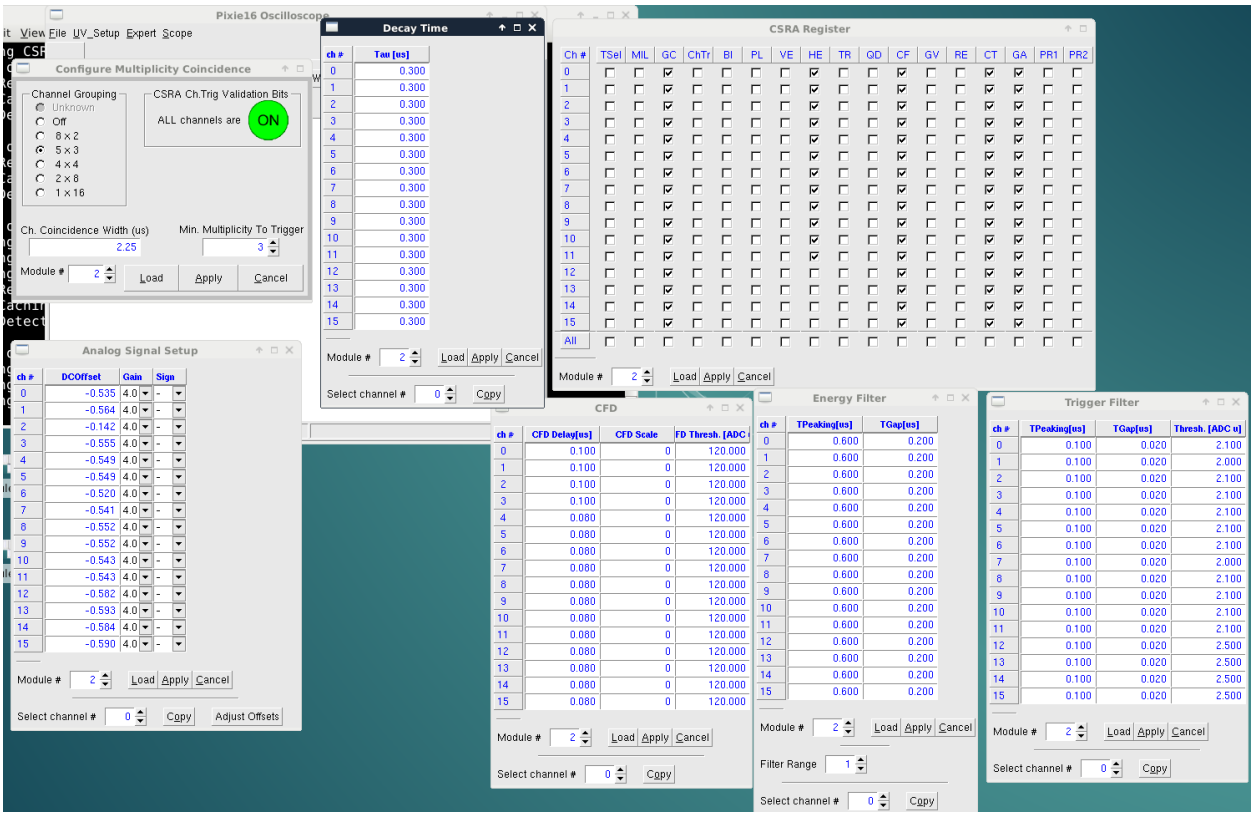

Figure A.3 Caption